FIELD MONITORING AND NUMERICAL ANALYSIS OF TEMPERATURE EFFECTS ON A SUPER-TALL STRUCTURE

ZHANG PENG

Ph.D

The Hong Kong Polytechnic University

2016

The Hong Kong Polytechnic University
Department of Civil and Environmental Engineering

FIELD MONITORING AND NUMERICAL ANALYSIS OF TEMPERATURE EFFECTS ON A SUPER-TALL STRUCTURE

ZHANG PENG

A Thesis Submitted in Partial Fulfillment of the Requirements for the

Degree of Doctor of Philosophy

January 2015

DECLARATION

I hereby declare that this thesis is my own work and that, to the best of my knowledge and belief, it reproduces no material previously published or written, nor material that has been accepted for the award of any other degree or diploma, except where due acknowledgement has been made in the text.

____________________ (Signed)

ZHANG Peng (Name of student)

ABSTRACT

For super-tall buildings, temperature is one of the most significant factors to affect the structural response. Therefore, understanding the temperature distribution of these structures is of practical importance. Extensive studies of the temperature effects on structures have been conducted on bridges, whereas very few on super-tall buildings due to their large size and complicated configuration. A long-term structural health monitoring (SHM) system consisting of over 800 sensors of 16 types has been implemented on Canton Tower, a tube-in-tube super-tall structure with the height of 600 m for real-time monitoring at both construction and service stages. As part of this sophisticated SHM system, 184 temperature sensors and 412 strain sensors have been deployed at 12 cross-sections of the inner and outer tubes. The real-time temperature and strain data at these measurement points provide an excellent opportunity to investigate the temperature distribution and temperature-induced responses of the super-tall structures.

In this PhD study, firstly the finite element (FE) models of the inner tube and members of the outer tube are established to investigate the temperature distribution through the heat transfer analysis. The simulated results are compared with the field monitoring data. The two sets of results show a good agreement with the measurements, indicating the effectiveness of the thermal analysis model.

The temperature distribution obtained from the numerical analysis is then used as an input into the global FE model of the Canton Tower to calculate the temperature-induced deformation. The calculated results are compared with the global position system (GPS)-measured results. The two results are very close, indicating that the proposed method is effective. It could be also noticed that a small temperature difference (approximated 3 to 4°C) between different facades of the outer tube induces the significant horizontal displacement (larger than 10 cm) for this slender super-tall structures.

The other contribution of this study is to propose a new method for calculating structural deformation using real-time distributed strain data, which can be easily measured at different sections. Assuming the building flexure is of bending beam type, the horizontal displacement of the structure is associated with the longitudinal strain. The virtual work theory is then used to calculate the horizontal displacement and tilt angle of the structure on the basis of the strain data at different heights of the structure. The calculated deformation shows a good agreement with the measurements by using GPS and inclinometers. The error analysis demonstrates that the calculated displacements have higher accuracy than the GPS-measured counterparts, and that the calculated tilts have a similar accuracy as those measured by the inclinometer. The results verify that the proposed method is efficient and can be applied to other civil structures.

The temperature effects on variations in modal properties of Canton Tower are finally investigated. The results show that an increase in temperature leads to a decrease in structural frequencies, whereas no clear correlation has been found between temperature and damping ration. Quantitative analysis shows that variations in frequencies are caused mainly by the change in the modulus of a material under different temperatures. That is, modal frequencies of the concrete structures decrease by approximately 0.15% when temperature increases by one degree Celsius. Frequencies of concrete structures are more sensitive to temperature change than steel structures.

PUBLICATION

Journal Papers:

Ni, Y.Q., Zhang, P., Ye, X.W., Lin, K.C. and Liao, W.Y., (2011), "Modeling of temperature distribution in a reinforced concrete supertall structure based on structural health monitoring data", *Computers and Concrete*, **8**(3), 293-309.

Xia, Y., Ni, Y.Q., Zhang, P, Liao, W.Y. and Ko, J.M., (2011), "Stress development of a super-tall structure during construction: field monitoring and numerical analysis", *Computer-Aided Civil and Infrastructure Engineering*, **26**(7), 542-559.

Bao, Y.Q., Xia, Y., Li, H., Xu, Y.L. and Zhang, P., (2012), "Data fusion-based structural damage detection under varying temperature conditions", *International Journal of Structural Stability and Dynamics*, **12**(6), No. 1250052.DOI: 10.1142/S02194555412500526.

Xia, Y., Zhang, P., Ni, Y.Q. and Zhu, H.P., (2014), "Deformation monitoring of a super-tall structure using real-time strain data", *Engineering Structure*, **67**, 29-38.

Conference Papers:

Xia, Y., Ni, Y.Q., Zhang, P., Liao, W.Y. and Ko, J.M., (2010), "Structural health monitoring of the Guangzhou New TV Tower", *Third International Symposium on Cold-formed Metal Structures*, 26 July 2010, Hong Kong, 137-157.

Zhang, P., Xia, Y., Ni, Y.Q., and Liao, W.Y., (2011), "Temperature distribution of Guangzhou New TV Tower based on structural health monitoring data", *Proceedings of the International Symposium on Innovation and Sustainability of*

Structures in Civil Engineering, 28-30 October 2011, Xiamen, China, 455-461.

Zhang, P., Xia, Y., and Ni, Y.Q., (2012), "Prediction of temperature induced deformation of a supertall structure using structural health monitoring data", *Proceedings of the 6th European Workshop on Structural Health Monitoring*, 3-6 July 2012, Dresden, Germany, 879-865.

Xia, Y., Zhang, P., and Ni, Y.Q., (2013), "Displacement of a skyscraper using various types of field monitoring data", *Proceedings of the 9th International Workshop on Structural Health Monitoring*, 10-12 September 2013, Stanford, California, USA, 1679-1685.

Xia, Y., Zhang, P., and Ni, Y.Q., (2014), "Temperature distribution of a super-tall tube-in-tube structure in South China", *Proceedings of the 13th International Symposium on Structural Engineering*, 24-27 October 2014, Hefei, China, 236-246.

ACKNOWLEDGMENTS

First and foremost I sincerely express my gratitude to my supervisor, Associate Professor Xia Yong, for providing me the opportunity to pursue my PhD study in HK PolyU, for his warm encouragement, patient guidance, extensive discussion throughout this research, for his invaluable comments and suggestions for this thesis, and for his high responsibility to students. It is a great benefit and honor to study under his supervision.

I also would like to sincerely thank my co-supervisor Professor Ni Yi-qing, for his continuous advice, and his kindly encouragement during my study in HK PolyU.

I am gratitude to the Department of Civil and Environmental Engineering of HKPolyU for the provided scholarship and prolific resource.

Special thanks are due to my wife and my family for all their love, encouragement and support during past years.

CONTENTS

LIST OF TABLES

Table **Page**

LIST OF FIGURES

Figure **Page**

LIST OF SYMBOLS

Symbol	Description
k	Thermal conductivity
ρ	Density
c	Specific heat capacity
t	Time
T	Temperature
q	Heat flux
h	Heat transfer coefficient
T_0	Initial condition
T_∞	Surrounding temperature
l_x, l_y, l_z	Direction cosines of the outward drawn normal to the boundary
S_1, S_2, S_3	Boundary condition
N	Ordinal number from January 1st
I_0	The rate of the solar energy at the atmosphere
I_D	Solar radiation intensity reaching the earth surface
P	Coefficient of atmospheric transparency
m	Atmospheric optical mass
β_s	Solar altitude
k_a	Ratio of atmospheric pressure
t_u	Turbidity factor
A_m, B_m	Empirical coefficient
ϕ	Relative position between the direction of sunrays
$I_{D\phi}$	Solar radiation intensity reaching the structure surface

φ	Latitude of the location
δ	Solar declination
α_n	Surface azimuth angle
β_n	Angle between the surface normal to the ground plane
τ	Solar hour angle
t_r	Hour of sunrise
t_s	Hour of sunset
t_s	Apparent solar time
t_{bj}	Beijing time
l	Longitude of the location
t_d	Jet lag θ_N
θ_N	Angle changed with the day of the year
$I_{d\beta}$	Diffuse solar radiation in the surface
$I_{r\beta}$	Reflected solar radiation in the surface
r_e	Surface reflectivity
I	Total solar radiation projected to the structure
q_s	Solar radiation absorbed by the structure surface
α	Absorptivity coefficient of the material
q_c	Rate of the heat transfer by convection
T_a	Surrounding air temperature
T_s	Temperature of the structure surface
h_c	Convection heat transfer coefficient
h_n	Heat transfer coefficient related to the structure material
h_f	Heat transfer coefficient related to the wind speed
q_r	Thermal irradiation between the surface and the air
h_r	Heat transfer coefficient of thermal irradiation
ε	Emissivity coefficient of the structure surface

T^*	Equivalent temperature
β	Integration factor
Δt	Incremental time step
δ	An increment in the corresponding parameter
n	Order
f_n	Undamped flexural vibration frequency of order n
θ_t	Thermal coefficient of linear expansion of the material
θ_E	Temperature coefficient of modulus
S_C	Area of the entire column
T_C	Calculated the equivalent temperature of the CFT column
T_{BR}	Equivalent temperature of the brace or ring members
dh	Element of length
$d\theta$	Angular rotation of the infinitesimal element
$\varepsilon_l, \varepsilon_r$	Vertical strain at the left and right surfaces of the element
$\Delta\varepsilon$	Difference between ε_l and ε_r
b	Height of the section
l_i	Bending moment
h_j	Length of i-th segment
M_u	Bending moment diagram
v_n	Beam top horizontal displacement
θ_n	Beam top tilt angle
X_d	Displacements along the short axes
Y_d	Displacements along the long axes
X'_d	Displacements to the east and north
Y'_d	Displacements to the north
σ	Standard deviation
λ_n	Dimensionless parameter
E	Modulus of elasticity

I	Moment of inertia of the cross-sectional area
l	Length of the beam
μ	Mass per unit length
f	Frequency
T_{air}	Ambient air temperature
β_0	Intercept
β_T	Slope
ε_f	Regression error

Abbreviations

SHM	Structural Health Monitoring
FE	Finite Element
RTK	Real Time Kinematic
GPS	Global Position System
CFT	Concrete-Filled-Tube
SS	Sensory System
DATS	Data Acquisition and Transmission System
DPCS	Data Processing and Control System
SHDMS	Structural Health Data Management System
SHES	Structural Health Evaluation System
IMS	Inspection and Maintenance System
DAUs	data acquisition units
GIS	Geographic Information System
EFDD	Enhanced Frequency Domain Decomposition

CHAPTER ONE

INTRODUCTION

1.1 Background

In recent years, numerous super-tall structures for commercial and residential functions have been built in many densely urbanized cities worldwide, and a great many are still being constructed. For these super-tall structures of hundreds meters, changes in environmental factors, especially temperature, have a significant influence on the overall deformation of the structures. Considerable temperature differences may occur among adjacent structural members under certain climatological conditions and result in notable structural internal forces and deformations due to the restraints. Field monitoring exercise of Canton Tower with the height of 600 m has shown that the temperature-induced maximum daily movement of the tower top is 15 cm, which is similar to the typhoon-induced motion (Xia *et al.* 2014). Previous studies about the temperature effects on structures are mainly conducted on bridges and very few are on supertall buildings. Therefore, it becomes essential and desirable to investigate the variation characteristics of the structural temperature distribution for properly analyzing the structural behavior in consequence of thermal effects.

1.2 Temperature Effects on Structures

Research efforts have been devoted to investigating temperature effects on the structural performance and dynamic characteristics of either high-rise structures or long-span bridges for a relatively long time. For example, in the 1960s, Zuk (1965) investigated thermal behavior of several highway bridges and found that the temperature distribution was affected by air temperature, wind, humidity, intensity of solar radiation and material type. It is noted that the numerical models have been developed since the 1970's to predict temperature distribution of structures and its variation with time. The scope has included solar radiation, convex, conduction, heat of hydration, member size and geometry, and maturity of adjoining concrete. For example, Elbadly and Ghali (1982) developed a 2-D finite element model to analyze the temperature distribution throughout a section of concrete bridge.

As temperature change may cause damage to concrete structures and composite structures, temperature monitoring has been widely employed, especially in mass concrete during construction stage. Recently, attention has also been given to long-span bridges and high-rise buildings due to the development of the structural health monitoring (SHM) systems. SHM provides a situ-based laboratory experimental innovation to measure the loadings, environment factors, and responses of the structures. For example, 250 temperature sensors have been installed at six sections in the Confederation Bridge to monitor its time-temperature history hourly, together with the movements at expansion joints and strains (Dilger, 2000). Pirner and Fischer (1999) conducted the measurement of stresses due to insolation ascertained on the Prague TV tower and concluded that stresses due to temperature changes were not of negligible magnitude. Xu et al. (2007) studied the variation of temperature and temperature effect on the global responses of the Tsing Ma Bridge. Variation of the temperature data and static responses at different components from 1997 to 2005 were analyzed. Xia et al. (2013) further constructed the finite element (FE) model and obtained the temperature distribution of the bridge through the thermal analysis and calculate the temperature-induced response. For high-rise buildings, researches are mainly focus on the wind-induced deformations and little attention has been given to the thermal effects. Breuer et al. (2008) utilized Global Positioning System technology to acquire the daily and seasonal drift at the top of the Stuttgart TV Tower due to solar radiation and the daily air temperature variation.

Developing long-term SHM systems for large-scale structures is able to provide thorough and reliable information for evaluating structural integrity, durability and reliability throughout the life-cycle and for ensuring optimal maintenance planning and safe operation. From the SHM system, environmental information such as temperature and responses of structures such as strains and displacements are obtained. However, little attention has been given to use these data to accurately describe the temperature distribution and establish the relationship between the temperature and structural responses for super-tall structures. How to solve these problems is still a big challenge.

1.3 Research Objectives

This study thus aims to investigate the environmental effects (especially the temperature effects) on super-tall structures by integrating field monitoring and numerical analysis. This research project has the following four objectives:

1)To develop thermodynamic models for estimation of the temperature distribution in super-tall structures. The accuracy of the model will be verified by the monitored temperature data.

2)To study the effect of temperature on the static responses (including deformation and strain) of super-tall structures, and establish the relation between them.

3)To study the effect of temperature on the dynamic properties of structures (such as frequencies, mode shapes, and damping), and establish their relation.

4)To verify the established approach through application to Canton Tower.

1.4 Thesis Organization

The problems and objectives of this study have been defined above with relevant background material. Chapter 2 presents a literature review of the current studies of the temperature effects on structures. The boundary condition and the finite element method for the thermal analysis are introduced. The SHM system of a 600 m high super-tall Canton Tower is introduced in Chapter 3. The heat transfer analysis method is then applied to obtain the temperature distribution of the Canton Tower in Chapter 4.The temperature distribution is then used as an input into the global finite element model of the Canton Tower to calculate the temperature-induced deformation and internal force in this Chapter. A new method for calculating structural deformation using real-time strain data is presented in Chapter 5. The results are compared with field monitoring results to verify effectiveness. Finally, the temperature effect on variations in modal properties of Canton Tower is investigated in Chapter 6. Quantitative analysis between the modal frequencies and air temperature are also conducted in this chapter. Chapter 7 concludes the works of the present study.

CHAPTER TWO

LITERATURE REVIEW

2.1 Introduction

It is widely recognized that changes in environmental factors, especially temperature, have a significant influence on the overall deflection and deformation of either high-rise structures or long-span bridges. In addition, thermal stresses are induced due to redundancy and/or non-uniform distribution of temperature. As the thermal stresses may cause damage to structures, especially for concrete structures and composite structures, the thermal effect has been studied for a relatively long time. Meanwhile, changing temperature affects the measured dynamic properties, such as frequencies, mode shapes, and damping, of structures which could not be neglected in the vibration-based health monitoring of civil engineering structures.

This chapter reviews the previous researches concerning the temperatures effects on the structure behaviors including the static responses such as displacement and stress, and dynamic responses such as natural frequencies, damping and mode shapes.

2.2 Temperature Distribution of Structures

To obtain the temperature effects on structures, the first step is to get the temperature distribution of the structure. In the early stage, researchers mainly obtained the temperature distribution of structures from measured temperature data. For example, Zuk (1965) started a study on thermal behavior of several highway bridges and found that the temperature distribution was affected by air temperature, wind, humidity, intensity of solar radiation and material type. Capps (1968) measured temperature and longitudinal movements of a steel box bridge in the UK. Imbsen (1984) briefly discussed the mean effective temperature and temperature differential of concrete bridges in his research project. Kennedy (1987) proposed a temperature distribution on the composite bridges based on a synthesis of several theoretical and experimental studies on prototype bridges. The distribution is linear through the depth of the slab and uniform through the depth of the steel beams. Design codes have also been developed to address the thermal effect, for example, American Association of State Highway and Transportation Officials (AASHTO) first published a guide specifications on the thermal effects of concrete bridge superstructures (1989) based on the earlier research by Potgieter and Gamble (1983).

2.2.1 Boundary Condition of the Heat Transfer Analysis

With the development of computer technology, FE models on heat transfer analysis have been introduced to predict temperature distribution of structures and its variation with time.

The spatial temperature distribution of a structure having uniform material properties at any time *t*, $T\left(x,y,z,t\right)$ follows the heat transfer equation (Rao 2005):

$$k\left(\frac{\partial^2 T}{\partial x^2}+\frac{\partial^2 T}{\partial y^2}+\frac{\partial^2 T}{\partial z^2}\right)=\rho c\frac{\partial T}{\partial t} \tag{2-1}$$

where k, ρ, and c are the thermal conductivity, density and specific heat capacity, respectively.

Eq. (2-1) can be simplified into a two-dimensional or even one-dimensional temperature field when variation of the temperature in one direction or two directions is assumed negligible.

To solve Eq. (2-1), two conditions need to be considered, one is the initial condition and the other is the boundary conditions. The initial condition is the initial temperature distribution of the structure, which is not difficult to determine. The initial condition can be expressed as

$$T(x, y, z, t = 0) = T_0(x, y, z) \tag{2-2}$$

where T_0 is the specified temperature distribution at time zero.

The boundary condition is the heat transfer between the structure surface and the environment, which is affected by many complex environmental factors and not easy to determine. To establish the simplified and reasonable heat transfer boundary condition is the key to obtain the temperature distribution of the structure.

The boundary conditions can be categorized into three kinds:

$$T(x, y, z, t = 0) = T_0 \text{ for } t > 0 \text{ on } S_1, \tag{2-3}$$

$$k(\frac{\partial T}{\partial x} l_x + \frac{\partial T}{\partial y} l_y + \frac{\partial T}{\partial z} l_z) + q = 0 \text{ for } t > 0 \text{ on } S_2, \tag{2-4}$$

$$k(\frac{\partial T}{\partial x} l_x + \frac{\partial T}{\partial y} l_y + \frac{\partial T}{\partial z} l_z) + h(T - T_\infty) = 0 \text{ for } t > 0 \text{ on } S_3, \tag{2-5}$$

where q is the boundary heat flux, h is the convection heat transfer coefficient, T_∞ is the surrounding temperature, l_x, l_y, l_z are the direction cosines of the outward drawn normal to the boundary, S_1 is the boundary on which the value of temperature is specified as $T_0\ (t)$, S_2 is he boundary on which the heat flux q is specified. S_3 is the boundary on which the convective heat loss $h(T - T_\infty)$ is specified.

The boundary condition stated in Eq. (2-3) is called Dirichlet condition and those stated in Eqs. (2-4) and (2-5) are called Neumann conditions. In the surface of the structure, the Neumann boundary conditions can be applied to consider the radiation and convection.

For a structure subjected to external environment, the thermal energy exchange between the structure surface and environment consists of convection, thermal irradiation, and solar radiation.

2.2.1.1 Solar Radiation

When the solar radiation goes through the atmosphere, it will be absorbed, reflected and diffused by the atmosphere. The solar radiation arrived at the earth surface is attenuated and some of the diffused counterpart is projected on the earth surface too. The solar radiation arrived at the structure surface normally consists of direct, reflect and diffuse radiation. Some of them are absorbed by the structure and some are reflected to the air.

a) Direct Solar Radiation

The rate of the solar energy at the atmosphere can be expressed in the following equation

$$I_0 = 1367[1 + 0.033\cos(2\pi N / 365)] \tag{2-6}$$

where N is the ordinal number from January 1st and the unit of I_0 is kW/m^2.

In the actual project, the solar radiation intensity reaching the earth surface takes the following approximation formula

$$I_D = I_0 P^m \tag{2-7}$$

where P is the coefficient of atmospheric transparency, m is the atmospheric optical mass which is the ratio between the sunray path at any moment and the counterpart at the moment that the solar altitude β_s is 90 degrees.

$$m = 1/\sin\beta_s \tag{2-8}$$

In regard to the coefficient of atmospheric transparency P, Kehlbeck (1975) propose a solar radiation intensity calculation model based on his study of the temperature effect on the concrete bridge. Elbadry (1983) simplified this model and formed the following calculation formula

$$P = 0.9^{t_u k_a} \tag{2-9}$$

where k_a is the ratio of atmospheric pressure to pressure at sea lever, as shown in Table 2-1, t_u is a turbidity factor accounting for the effect of clouds and air pollution, which can be calculated in the following formula

$$t_u = A_m - B_m \cos(2\pi N/365) \tag{2-10}$$

where A_m and B_m are the empirical coefficient, as shown in Table 2-2.

Table 2-1. The relative atmospheric pressure at different altitude

altitude (m)	0	500	1000	1500	2000	2500	3000
k_a	1.	0.94	0.89	0.84	0.79	0.74	0.69

Table 2-2. The relative atmospheric pressure at different altitude

coefficient	mountainous area	rural area	urban area	industrial area
A_m	2.2	2.8	3.7	3.8
B_m	0.5	0.6	0.5	0.6

When the sunrays make the angle ϕ with the normal of the to the surface in any direction, the solar radiation intensity becomes

$$I_{D\phi} = I_D \cos\phi \qquad (2\text{-}11)$$

The solar incident angle ϕ represents the relative position between the direction of sunrays (denoted as *s* in figure 2-1) to the structure surface normal (denoted as *n*) and can be calculated as

$$\cos\phi = (\sin\varphi \sin\beta_n - \cos\varphi \cos\alpha_n \cos\beta_n)\sin\delta + (\cos\varphi \sin\beta_n + \sin\varphi \cos\alpha_n \cos\beta_n)$$
$$\cos\delta \cos\tau + \sin\alpha_n \cos\beta_n \cos\delta \cos\tau \qquad (2\text{-}12)$$

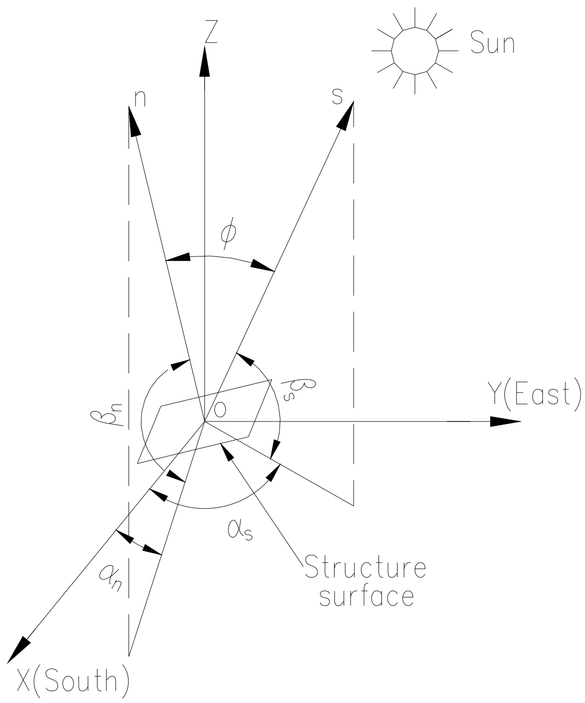

Figure 2-1. Solar incident angle for the structure surface

in which φ is the latitude of the location; δ is the solar declination; α_n is the surface azimuth angle; β_n is the angle between the surface normal to the ground plane; τ is the solar hour angle. The solar declination can be calculated by the approximation

$$\delta = 23.45° \sin[2\pi(284 + N)/365] \tag{2-13}$$

The solar radiation intensity obtained in Eq. (2-11) are only between the hour of sunrise t_r and sunset t_s, which can be calculated by

$$t_r = 12 - \frac{12 \arccos(-\tan\varphi \tan\delta)}{\pi} \tag{2-14}$$

$$t_s = 12 + \frac{12 \arccos(-\tan\varphi \tan\delta)}{\pi} \tag{2-15}$$

and solar hour angle between the hour of sunrise and sunset is expressed in

$$\tau = (12 - t_s) \times 12 / \pi \tag{2-16}$$

where t_s is the apparent solar time, which can be calculated by

$$t = t_{bj} - \frac{(120° - l)}{15°} + t_d \tag{2-17}$$

where t_{bj} is the Beijing time, l is the longitude of the location, t_d is the jet lag and can be calculated by

$$t_d = 165 \sin 2\theta_N - 0.025 \sin\theta_N - 0.126 \cos\theta_N \tag{2-18}$$

where θ_N is the angle changed with the day of the year and can be calculated by

$$\theta_N = 2\pi(N - 81)/364 \tag{2-19}$$

According Eq. (2-6) to Eq. (2-19) the direct solar radiation intensity at the observation surface in any direction from sunrise to sunset in any typical sunny day of one year can be obtained.

b) Diffuse and reflected Solar Radiation

A portion of the solar radiation which is diffused by the atmosphere will go back to ground. The diffuse solar radiation in any surface can be calculated by the following empirical formula

$$I_{d\beta} = (\frac{1+\sin\beta_n}{2})(0.271I_0 - 0.294I_D)\sin\beta_s \tag{2-20}$$

Meanwhile, after reaching the ground, part of the solar radiation is reflected by the surface and re-projects to the structure surface. It can be calculated by

$$I_{r\beta} = (\frac{1-\sin\beta_n}{2})r_e(I_D\sin\beta_s + (0.271I_0 - 0.294I_D)\sin\beta_s) \tag{2-21}$$

where r_e is the surface reflectivity, r_e =0.2 (normal ground), and r_e =0.7 (snow ground)

c) Total Solar Radiation

According to the mentioned above, the solar radiation reaching the structure surface consists of three portions, direct, diffuse and reflected solar radiation. Thus the total solar radiation projected to the structure can be expressed by

$$I = I_{D\phi} + I_{d\beta} + I_{r\beta} = I_D\cos\phi + (\frac{1+\sin\beta_n}{2})(0.271I_0 - 0.294I_D)\sin\beta_s$$

$$+(\frac{1-\sin\beta_n}{2})r_e(I_D\sin\beta_s + (0.271I_0 - 0.294I_D)\sin\beta_s) \tag{2-22}$$

The solar radiation cannot be absorbed by the structure surface totally and parts of them are reflected to the air. The shortwave radiation absorptivity is defined as the ratio of the radiation absorbed by the structure surface to the projected radiation, which is related to the color and roughness of the surface. Table 2-3 shows the solar radiation absorptivity for different surface. Then the solar radiation absorbed by the structure surface can be expressed by

$$q_s = \alpha I = \alpha[I_D \cos\phi + (\frac{1+\sin\beta_n}{2})(0.271 I_0 - 0.294 I_D)\sin\beta_s$$

$$+(\frac{1-\sin\beta_n}{2})r_e(I_D \sin\beta_s + I_{dH})] \tag{2-23}$$

Table 2-3. The solar radiation absorptivity of different surface

Surface condition	Absorptivity
common concrete	0.55-0.70
asphalt concrete	0.90-0.97
white coating	0.21-0.30
silver coating	0.55
read coating	0.60
grey coating	0.75
black coating	0.90-0.97

2.2.1.2 Convection

When the temperature of the structure surface is different from the counterpart of the surrounding air, the heat transfers between them. The rate of the heat transfer by convection is associated with the speed of the air and depends on the temperature difference between the air and structure surface. It can be expressed by the Newton's Law

$$q_c = h_c(T_a - T_s) \tag{2-24}$$

where T_a is the temperature of the surrounding air temperature; T_s is the temperature of the structure surface; h_c is the convection heat transfer coefficient (Wm^{-2}℃), which depends on many factors such as the surface roughness, wind speed and the surrounding temperature. Usually it can be calculated by the following empirical formula (Branco 1986)

$$h_c = h_n + h_f \tag{2-25}$$

where parameter h_n has the average value of 6 Wm^{-2}℃ for concrete and 7.5 Wm^{2}℃ for steel; h_f is the function of the wind speed *v*, approximately expressed by $h_f = 3.7v$.

2.2.1.3 Thermal irradiation

The structure, like all other substance in the nature, can emit and absorb the thermal irradiation simultaneously with the surrounding substance. The heat transferred by this type of long wave thermal irradiation between the surface and the air is expressed by the following simplified formula according to the Stefan-Boltzmaan law

$$q_r = h_r(T_a - T_s) \tag{2-26}$$

where h_r is the heat transfer coefficient and can be approximately expressed by

$$h_r = \varepsilon[4.8 + 0.075(T_a - 5)] \tag{2-27}$$

where ε ($0 < \varepsilon < 1$) is the emissivity coefficient of the structure surface.

2.2.1.4 Establish the Boundary Conditions

For a structure subjected to solar radiation, the thermal energy transferred between the structure surface and environment consists of convection q_c, thermal irradiation q_r and solar radiation q_s, expressed as

$$q = q_c + q_r + q_s \tag{2-28}$$

From Eqs. (2-23), (2-24) and (2-26), the heat exchange between a surface and the environment can be expressed as an equivalent convective exchange between the structural surface at temperature T_s and the external air flow at an equivalent temperature T^*, expressed as

$$q = h(T^* - T_s) \tag{2-29}$$

where h is the heat transfer coefficient including both the convection and thermal irradiation and can be expressed as

$$h = h_c + h_r \tag{2-30}$$

The equivalent temperature T^* has the expression as

$$T^* = T_a + \frac{\alpha I}{h} \tag{2-31}$$

The Neumann boundary conditions can be obtained through the above equations and then are used to conduct the heat transfer analysis.

2.2.2 Finite Element Method for Temperature Distribution Problem

FE method is the most common method to solve the transient thermal problem. The first step of the FE procedure is to divide the spatial domain to combine the ordinary differential equations with regard to the time coordinate. The FE equation can be derived either by using a variational (Rayleigh-Ritz) approach or from the governing differential equation using a weighted residual (Galerkin) approach (Rao 2005). And then by using the finite difference method, the equation could be solved.

For civil structures, the spatial temperature distribution of a structure having uniform material properties at any time t, $T(x, y, z, t)$ follows the heat conduction Eq. (2-1)

The initial condition is expressed by Eq. (2-2) and the Neumann boundary conditions expressed by Eqs. (2-4) and (2-5) are commonly applied to civil structures surface to consider the radiation and convection.

The spatial domain V is divided into E of p nodes each, and then a suitable form of variation of T in each finite element express $T^{(e)}(x,y,z,t)$ in element e as

$$T^{(e)}(x,y,z,t) = [N(x,y,z)]\vec{T}^{(e)} \tag{2-32}$$

where

$$[N(x,y,z)] = [N_1(x,y,z) \;\; N_2(x,y,z) \;\; \cdots \;\; N_p(x,y,z)]$$

$$\vec{T}^{(e)} = \begin{Bmatrix} T_1(t) \\ T_2(t) \\ \vdots \\ T_p(t) \end{Bmatrix}$$

In both of the variational and Galerkin approach, the FE equations for the heat conduction problem can be derived to the following matrix form as

$$[K_3]\dot{\vec{T}} + [K]\vec{T} = \vec{P} \tag{2-33}$$

where

$$[K_3] = \sum_{e=1}^{E}[K_3^{(e)}] \tag{2-34}$$

$$[K] = \sum_{e=1}^{E}\Big[[K_1^{(e)}] + [K_2^{(e)}]\Big] \tag{2-35}$$

and

$$\vec{P} = \sum_{e=1}^{E}\vec{P}^{(e)} \tag{2-36}$$

The expression for $[K_1^{(e)}]$, $[K_2^{(e)}]$, $[K_3^{(e)}]$,and $\vec{P}^{(e)}$ can be stated using matrix notation as

$$[K_1^{(e)}] = \iiint\limits_{V^{(e)}} [B]^T[D][B]dV \tag{2-37}$$

$$[K_2^{(e)}] = \iint_{S_3^{(e)}} h[N]^T [N] dS_3 \tag{2-38}$$

$$[K_3^{(e)}] = \iiint_{V^{(e)}} \rho c[N]^T [N] dV \tag{2-39}$$

$$\vec{P}^{(e)} = -\vec{P}_2^{(e)} + \vec{P}_3^{(e)} \tag{2-40}$$

where

$$P_2^{(e)} = \iint_{S_2^{(e)}} q[N]^T dS_2 \tag{2-41}$$

$$P_3^{(e)} = \iint_{S_3^{(e)}} hT_\infty [N]^T dS_3 \tag{2-42}$$

$$D = k\begin{bmatrix} 1 & 0 & 0 \\ 0 & 1 & 0 \\ 0 & 0 & 1 \end{bmatrix} \tag{2-43}$$

$$B = \begin{bmatrix} \dfrac{\partial N_1}{\partial x} & \dfrac{\partial N_2}{\partial x} & \cdots & \dfrac{\partial N_p}{\partial x} \\ \dfrac{\partial N_1}{\partial y} & \dfrac{\partial N_2}{\partial y} & \cdots & \dfrac{\partial N_p}{\partial y} \\ \dfrac{\partial N_1}{\partial z} & \dfrac{\partial N_2}{\partial z} & \cdots & \dfrac{\partial N_p}{\partial z} \end{bmatrix} \tag{2-44}$$

The transient thermal analysis can be solved by means of the following algorithm

$$T_{t+\Delta t} = T_t + \Delta t[(1-\beta)\dot{T}_t + \beta \dot{T}_{t+\Delta t}] \tag{2-45}$$

where β is an integration factor, and Δt is the incremental time step. When $\beta = 0$, it is the forward difference scheme

$$\dot{T}_t = \frac{T_{t+\Delta t} - T_t}{\Delta t} \tag{2-46}$$

In contrast, if $\beta = 1$, it is the backward difference scheme

$$\dot{T}_{t+\Delta t} = \frac{T_{t+\Delta t} - T_t}{\Delta t} \tag{2-47}$$

When $\beta = 1/2$, it is the Crank-Nicolson difference scheme

$$T_{t+\Delta t} = T_t + \frac{\Delta t}{2}[\dot{T} + \beta \dot{T}_{t+\Delta t}] \tag{2-48}$$

When $\beta = 2/3$, it is the Galerkin difference scheme

$$T_{t+\Delta t} = T_t + (\frac{2}{3}\dot{T} + \frac{1}{3}\dot{T}_{t+\Delta t})\Delta t \tag{2-49}$$

It is noted that the algorithm is unconditionally stable, when $\beta \geqslant 1/2$.

On time $t + \Delta t$, the differential equations can be stated as

$$[K_3]\dot{\vec{T}}_{t+\Delta t} + [K]\vec{T}_{t+\Delta t} = \vec{P} \tag{2-50}$$

Substituting Eq. (4-44) to Eq. (4-49), the following equation is obtained

$$([K_3] + \beta \Delta t[K])\dot{\vec{T}}_{t+\Delta t} = -[K](\vec{T}_t + (1-\beta)\Delta t \dot{\vec{T}}_t) + \vec{P} \tag{2-51}$$

which can be solved to obtain $\dot{\vec{T}}_{t+\Delta t}$ and then $\vec{T}_{t+\Delta t}$ can be obtained from Eq. (2-51).

Based on the above equations, the thermal field model can be developed to estimate the time-dependent temperature throughout the entire structure. One-dimensional (1-D) to three-dimensional (3-D) models have been developed.

Dilger (1982) started a study on the temperature distribution of composite box girder bridges by using a 1-D finite difference program and the largest temperature difference condition was found. Ho (1989) also developed a 1-D heat-flow model and compared the results with field measurements and then the extreme thermal loadings in highway bridges were obtained through the statistical analysis. Malcolm (1984) constructed a 1-D heat transfer model to obtain the temperature profile of a concrete roof slab heated by solar radiation.

To analyze the temperature distribution of a bridge, it is normally assumed that the temperature is constant over its length. This leads to a two-dimensional (2-D) heat transfer model that can be used to get the temperature distribution of one cross-section of a bridge. For example, Elbadry and Ghali (1983) developed a 2-D FE model to analyze the temperature distribution throughout a cross-section of a concrete bridge. Mirambell (1991) used two numerical methods based on a FE and a finite difference formulation to evaluate the temperature distribution in bridges. Branco (1993) also employed a FE method for the resolution of the Fourier heat-transfer equation and its associated boundary conditions to estimate the temperature distribution.

Adjali (2000) compared 2-D and 3-D models to simulate the temperatures in a ground floor slab and the soil beneath it and found that the 2-D model was satisfactory to predict the temperature variations in the soil when the slab was large and the 3-D model was necessary to accurately simulate the heat flows near the corner of the slab.

The numerical models presented by the previous study could take into account the geometry of the structures, the thermal properties of the materials, the location of the structures, and the climatic conditions (Elbadry and Ghali 1983, Branco 1993). Parametric studies could be conducted through the numerical techniques to obtain the highest temperature differences in different structures. The conditions under which the temperature difference is the highest could be also found through the parametric study (Dilger, 1982). Design temperature values for codes could also be got from the parametric studies (Mirambell, 1991). Uncertainties in input parameters like thermal properties of the materials could also be accounted through a differential sensitivity analysis (Adjali, 2000). Au (2002) also developed a systemic parametric approach to develop the site-specific temperature profiles for the composite bridges and applied it to the Hong Kong area.

2.3 Temperature Effects on Static Responses of Structures

As temperature change may cause damage to concrete structures and composite structures, attention has been given to thermal responses of structures. In the early stage, there were very few data of temperatures and thermal responses for structures, researchers mainly predicted the responses through numerical techniques. Dilger (1982) developed a FE computer program to find the extreme temperature difference of a composite bridge and the chosen temperature distribution was used as an input for analyzing the stress caused by the temperature. Saleh (1990) investigated the temperature effects on three different types of structures using different techniques and suggested three different methods to eliminate the temperature effect. Moorty (1992) conducted thermo-elastic analysis to obtain the movements and associated stresses induced by temperature in different types of bridges and did a field test to verify the analytical models. Saetta (1995) presented a numerical procedure based on the FE method for the stress-strain analysis to calculate the thermal responses of concrete structures and applied the proposed numerical method to a concrete dam and a typical bridge section to prove the effectiveness and reliability of this method in practical structural design.

With the development of SHM system, temperature monitoring and thermal response monitoring of structures have been widely employed. More and more real-time temperature data and structural responses data like deformation, strain and stress were obtained, the understanding of structural thermal behavior gone deeper.

For example, based on a three-year monitoring program with over 200 temperature sensors installed on 8 different cross-sections, Forli (1996) analyzed the thermal behavior of a box girder bridge by using a FE model and found the simulated results agreed well with the observed values. Then an algorithm for calculating the effective mean temperature and linear vertical and horizontal gradients from field temperatures was obtained.

Shahawy and Arockiasamy (1996) compared the measured time-dependent strains of the Sunshine Skyway Bridge with the analytical predictions, provided that thermal effects could be accounted for independently in the analytical model. The total strains inclusive of the thermal strains together with the predicted time-dependent strains show reasonable agreement with the measured data.

The time-temperature history of a three-span 500 m long Confederation Bridge was monitored by over 250 temperature sensors installed at six sections. The movements at the expansion joint and strains were also monitored as well (Dilger, 2000).

Based on the measured temperature data over two and half years of a box girder bridge, Roberts-Wollman et al. (2002) proposed the modified Potgieter and Gamble (1983) temperature difference equations to predict the positive temperature difference and compared the results to the measurements and the comparison demonstrated that the proposed method worked reasonably well. Then the deflections of this bridge in two days were calculated and the results compare well with measured.

Fu and DeWolf (2004) conducted a field investigation and numerical analysis on a curved concrete bridge concerning the temperature effect on the tilt and natural frequencies. The temperature changes in the bridge superstructure subject the columns to torsion deformations and field inspections have shown that there were spiral cracks in the columns corresponding to these torsion deformations.

Wang (2008) investigated the crack opening displacement of the Kishwaukee Bridge in Illinois and found that the crack opening displacement due to temperature was about 2 times the effect due to traffic loadings in its daily magnitude.

In the last decade, more and more high-rise buildings and long-span bridges have been built around the world. Research efforts have also been devoted to investigating temperature effects on the performance of these structures.

Tong et al. (2001) and Au et al. (2001) parallel carried out a laboratory study of segmental steel sections under the influence of the solar radiation and a field temperature measurement on the Tsing Ma Bridge to verify the heat transfer FE models. Good agreement between the numerical results and field measurements was observed.

Wong et al. (2002) introduced a 3-year thermal monitoring and response monitoring of the Ting Kau Bridge. The daily temperature variations of different segments of this bridge were obtained. The daily variation of the thermal effect induced no more than 10% of the overall variation of the stress in the steel girder due to the live loads.

De Sortis and Paoliani (2007) studied the long-term variation of crest displacement of a dam due to air temperature and water level, via both statistical approach and structural identification. The structural identification results provide a higher degree of accuracy in predicting the future response of the structure.

Xu et al. (2010) studied the variation of temperature and temperature effect on the global responses of the Tsing Ma Bridge. The results show that the longitudinal displacement responses of the bridge towers, deck sections, and cables have strong linear relationships with the effective deck temperature. The vertical displacement of partial structure members is well correlated with the effective deck temperature and the lateral displacement responses of the Tsing Ma Bridge are not dominantly affected by the temperature. Xia et al. (2013) further constructed the FE model and obtained the temperature distribution of the bridge through the thermal analysis.

After inputting the temperature data into the structural model of the whole bridge, the temperature induced displacement and strain responses of various bridge components were obtained and a good level of agreement was achieved between the bridge responses and the monitoring data.

Nevertheless, field study of temperature distribution and static temperature responses of high-rise structures is still very rare. Pirner and Fischer (1999) measured the stress of the 198m high Prague TV tower and concluded that the stresses due to temperature changes were not negligible. Tamura (2002) used the real time kinematic-global position system (RTK-GPS) (Leica MC1000) measured the static displacement of a 108 m high steel tower caused by heat stress on a calm and fine weather day. It is found that the tower moved in a circular shape in the daytime and returned to the original place after sunset. The daily displacement of the tower top in northwest direction was approximately 4 cm. The temperature distribution on the external surface of the Stuttgart TV Tower has been recognized and the daily and seasonal drift of the tower top due to solar radiation and daily air temperature variation have been acquired (Breuer et al. 2008). It is found that the path of the tower top described an ellipse related to the sun and change of the movement was based on the change of meteorological conditions.

However, in some large-scale structures especially the long-span bridges and high-rise buildings, the thermal FE models were hard to establish or simplify and the measured structural response data normally caused by different kinds of loadings. The monitored temperature data and static responses haven’t been well compared with the model predictions. This means the thermal behavior of these structures were not fully understood.

2.3 Temperature Effects on Structural Dynamic Properties

Varying temperature dose not only affect structural static response, but also the dynamic properties such as frequency, mode shapes, and damping.

2.3.1 Relation between Temperature and Dynamic Properties of Structures

Pioneer study of the relationship between the temperature and natural frequency of structures may attribute to Adams et al. (1978), who investigated the relation between temperature and axial resonant frequency of a bar. During the last 20 years, more and more studies in this field have been carried out on real structures.

Askegaard and Mossing (1988) studied a three-span RC footbridge and observed a 10% seasonal change in frequency over a three-year period.

Researchers from Los Alamos National Laboratory found that the first three natural frequencies of the Alamosa Canyon Bridge varied about 5% during a 24 hour period as the temperature of the bridge deck changed by approximately 22°C (Comwell, 1999).

Sohn (1999) developed a linear adaptive model to discriminate the changes of modal parameters due to temperature changes from those caused by structural damage or other environmental effects and apply this model to the same bridge to demonstrate the effectiveness of this model.

Peeters and De Roeck (2001) continuously monitored the Z24-Bridge for nearly a year and they reported that the frequencies decreased with the temperature increase.

Fu and DeWolf (2001) found that there is only an increase in frequency of a two-span composite steel-girder bridge with decreasing temperatures below the temperature at which the bearings become partially restrained.

Breccolotti et al. (2004) numerically simulated the temperature effect on the dynamic characteristics of a simple supported bridge and found that the temperature changes may shadow in many cases the frequency variations due to the mechanical damage.

Ni et al. (2005) used the support vector machine technique to investigate the effect of temperature on modal parameters in the Ting Kau Bridge in Hong Kong using one-year monitoring data and found that the that the environmental temperature changes account for variation in modal frequencies with variance from 0.20% to 1.52% for the first ten modes.

Desjardines et al. (2006) studied modal data and average girder temperature collected over a six-month period in the Confederation Bridge and found that there was a clear trend of reduction in the modal frequencies with increase in the average temperature of the concrete of the bridge.

The first two modal frequencies identified from the Bill Emerson Memorial Bridge (Song, 2006) monotonically decreased as the temperature went up in a linear way, while the mode shapes did not experience a significant change.

Liu and DeWolf (2007) found that the frequencies of a curved concrete box bridge varied by a maximum of 6% in a peak to peak temperature range of 70°F (39°C) during one year.

Xia et al (2006a) conducted experiments on a continuous concrete slab for nearly two years. Not only temperature changes, but also humidity effect on variation of frequencies, mode shapes and damping were investigated. It is found that the frequencies have a strong negative correlation with temperature and humidity, damping ratios have a positive correlation, but no clear correlation of mode shapes with temperature and humidity change can be observed. From the daily variation of modal properties and temperature data, they (Xia, 2006b) have found that the variation of frequencies lagged behind the variation of temperature at the top of the slab by a few hours.

Nayeri et al. (2008) monitored a 17-story steel frame building and it showed a strong correlation between the frequency and air temperature while the frequency variations lagged behind the temperature variations by a few hours. A chamber experiment which was conducted by Balmes et al. (2008) demonstrated that axial stresses due to different thermal expansion in members cause the frequencies to change significantly.

For most of the construction materials, it is generally accepted that an increase in temperature will cause a decrease in Young's modulus and shear modulus of the materials.

In Xia's study (2006a), by assuming the variation of Young's modulus with temperature is linear for small changes in temperature, the increment of the undamped flexural vibration frequency of order *n* for a simply supported uniform beam can be expressed as

$$\frac{\delta f_n}{f_n} = \frac{1}{2}(\theta_t + \theta_E)\delta t \tag{2-52}$$

where δ represents an increment in the corresponding parameter; f_n is the undamped flexural vibration frequency of order n; θ_t is the thermal coefficient of linear expansion of the material; θ_E is the temperature coefficient of modulus, the coefficient θ_E of concrete is approximately 4.5×10^{-3}/℃, for $t < 100$℃, and 1.4×10^{-3}/℃, for $t > 100$℃, and for steel the coefficient θ_E is about 3.6×10^{-3}/℃.

Therefore, it has been widely observed that natural frequencies of structures decrease with the increasing temperature.

2.3.2 Damage Detection Considering Environmental Conditions

In vibration-based health monitoring of civil engineering structures, it is not only the health of a structure affects the measured dynamic properties, but also the changing temperature and other applied excitations such as wind and traffic.

Peeters (2001) compared results of different types of excitations like band-limit noise generated by shakers, an impact from a drop of weight, wind and traffic for the Z24 Bridge and proposed a methodology to distinguish the temperature effects from real damage events.

Since the changing environmental and operational conditions can often mask the changed in the measured signal caused by real damage, a unique combination of time series analysis, neural networks, and statistical inference techniques is developed by Sohn (2002) for damage classification taking into account the environmental and operational variations.

Yan (2003) proposed a method based on principal component analysis to eliminate the environmental effects for SHM, whose advantage is that is does not require to measure environmental parameters.

Giraldo (2006) also presented a statistically based analysis to analyze the distribution of identified structural parameters over an unknown number of external conditions and to effectively reduce their influence on the localization of damage. The proposed method was then applied to a four story, two-bay by two-bay building which was used as SHM benchmark problems to demonstrate the effectiveness of this technique.

As the operational, environmental and even computational variability could influence damage indicator functions, a sensitivity model-based technique, which focuses on the physical rather than the statistical nature of variability was developed by Kess (2007) and applied to a woven composite plate.

Xu and Wu (2007) analyzed the dynamic characteristics like frequencies and mode shapes considering seasonal temperature difference and sunshine temperature difference and then compared the changes in dynamic characteristics due to the temperature variations and damage of girders and cables. They found that changes in dynamic characteristics due to damage in girders or cables might be smaller than those changes due to variations in temperature.

Kullaa (2011) proposed a method which utilizes the hardware redundancy by modelling the sensor network as a Gaussian process and estimating the signal of each sensor in the network using the others to distinguish between sensor fault, structural damage, and environmental or operational effects in a SHM system. Since false alarms may result if a measurement is made under novel or extreme environmental or operational conditions not included in the training data, actually measuring the environmental or operational variables can check if the change in the system might be due to extreme conditions.

2.4 Challenge in Temperature Effects on Structure

Although many researchers have studied in the area of temperature effects on structures, there are a number of challenging issues especially for large-scale structures.

One issue is that the complex geometry of the modern structure especially the super-tall structures makes it is difficult to establish a suitable global model or a simplified low dimension model to conduct the heat transfer analysis. The solar radiation is usually not measured in the field monitoring, which makes the numerical models cannot be effectively calibrated and improved. The boundary condition is normally calculated inaccurately.

The number and location of sensors are another important issue. Bortoluzzi (2013) suggested using a subset of collected time histories for associating a few temperature readings with a full definition of the temperature field and applied the procedure to a railway bridge in Austria. However, for large-scale structures, it is not feasible to install large number of sensors due to the limited budget of the SHM system. The temperature distribution obtained from limited measurement points cannot represent the real situation. The measured results need to be integrated with the satisfactory numerical simulated results.

CHAPTER THREE

CANTON TOWER AND ITS SHM SYSTEM

3.1 Canton Tower

Canton Tower is a super-tall structure with a height of 600 m. After being used for broadcasting the 16th Asian Games, which was held in Guangzhou from November 12 to November 27, 2010, the Canton Tower is now serving for office, entertainment, catering, tour, and transmission of television and radio programmes.

As shown in Figure 3-1, the Canton Tower is a concrete-steel composite structure, consisting of a main tower (454 m) and an antennary mast (146 m). The underground has 2 floors with a height of 10 m in total and an expanded plan of about 167 m × 176 m. Pile foundation is employed for the structure.

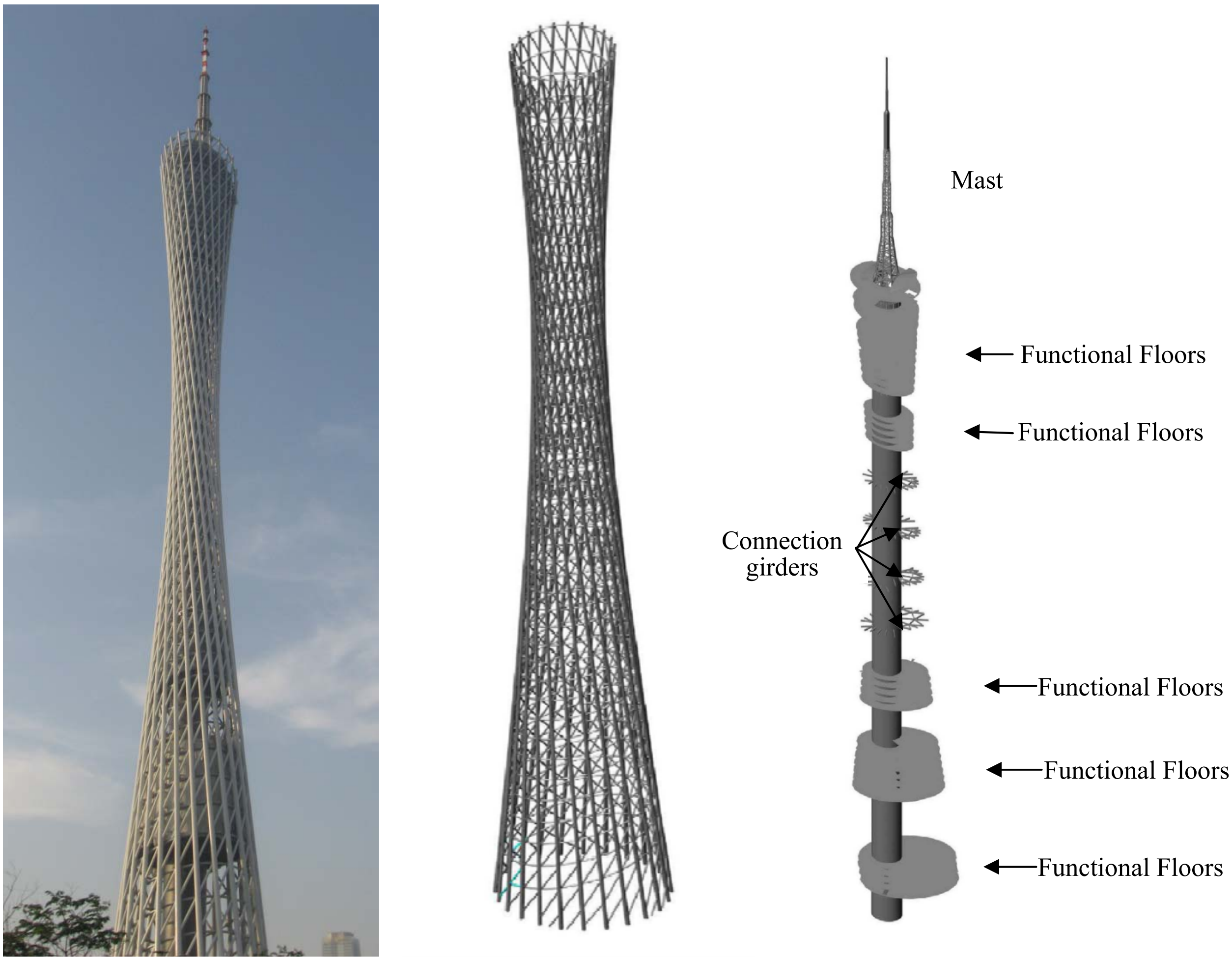

(a) The perspective view (b) Outer steel structure (c) Inner concrete structure

Figure 3-1. Canton Tower

Figure 3-2 shows a typical floor plan in those sections with functional floors of Canton Tower. The inner tube has an oval shape with a constant dimension of 14 m × 17 m, while the centroid differs from the centroid of the outer oval. The long axis of the inner tube is directed toward of 18° west to north. The thickness of the tube varies from 1.0 m at the bottom to 0.4 m at the top. High strength low shrinkage concrete with grade C80 (according to Chinese code GB 50010, 2002, its characteristic cube strength = 50.2 MPa) was poured below the height of 36 m and the concrete grade decreases to C45 (characteristic cube strength = 29.6 MPa) at the top of the tower gradually.

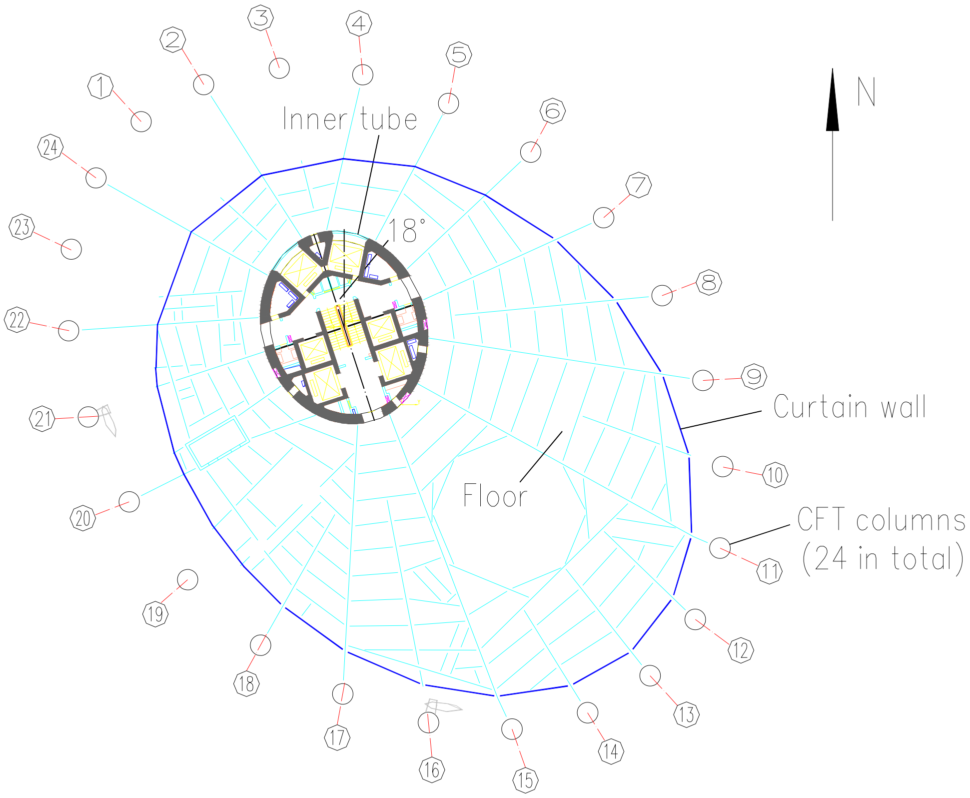

Figure 3-2. A typical floor plan of Canton Tower

Figure 3-3 shows a typical cross-section of the inner tube. The inner tube mainly functions as vertical transportation, which includes 6 lifts, stairs, and a few facility rooms to place pipes and cables. An antenna mast of 146 m high stands on the top of the inner tube and is made of steel spatial frame with an octagonal cross-section (as shown in Figure 3-4) of approximately 13 m in the maximum diagonal.

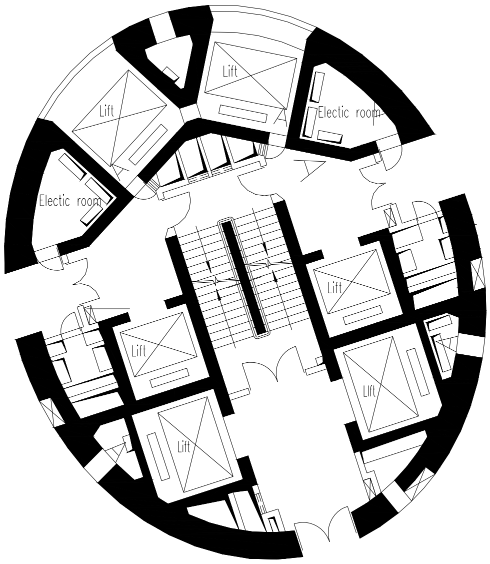

Figure 3-3. A typical cross-section of inner tube

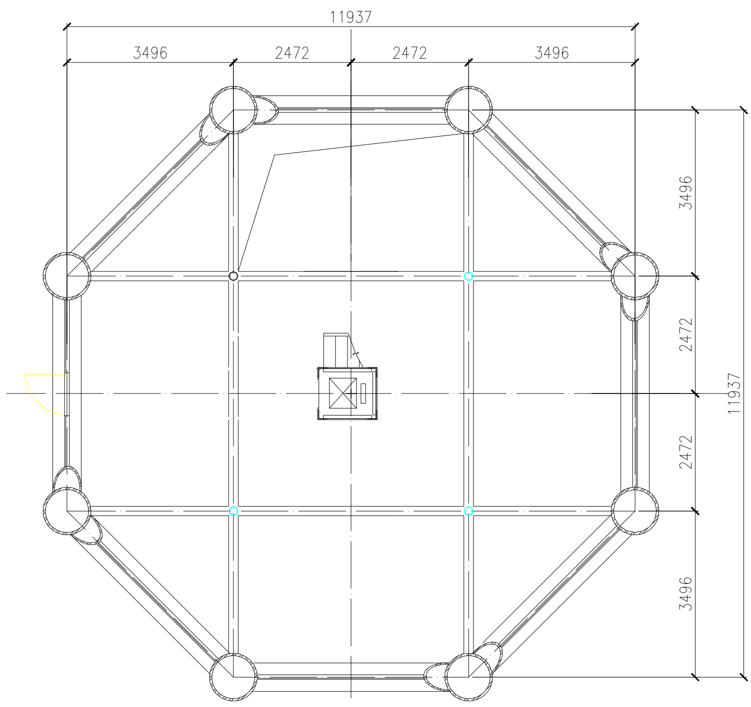

Figure 3-4. The cross-section of the bottom of the antenna

As shown in Figure 3-5, the outer tube consists of 24 concrete-filled-tube (CFT) columns, uniformly spaced in an oval while inclined in the vertical direction and connected by hollow steel rings and braces. Dimension of the oval decreases from 60 m × 80 m at the underground level (height of -10 m) to the minimum of 20.65 m × 27.5 m at the height of 280 m, and then increases to 40.5 m × 54 m at the top of the tube (454 m), shown in Figure 3-6. The top oval is rotated clockwise by 45 degrees with respect to the bottom oval in the horizontal plane. There are 46 steel 'ring' beams link the CFT columns with an inclination angle of 15.5 degrees to the horizontal plane and non-uniform intervals in vertical direction. The hollow steel braces connect all the joints of the CFT columns and the ring beams.

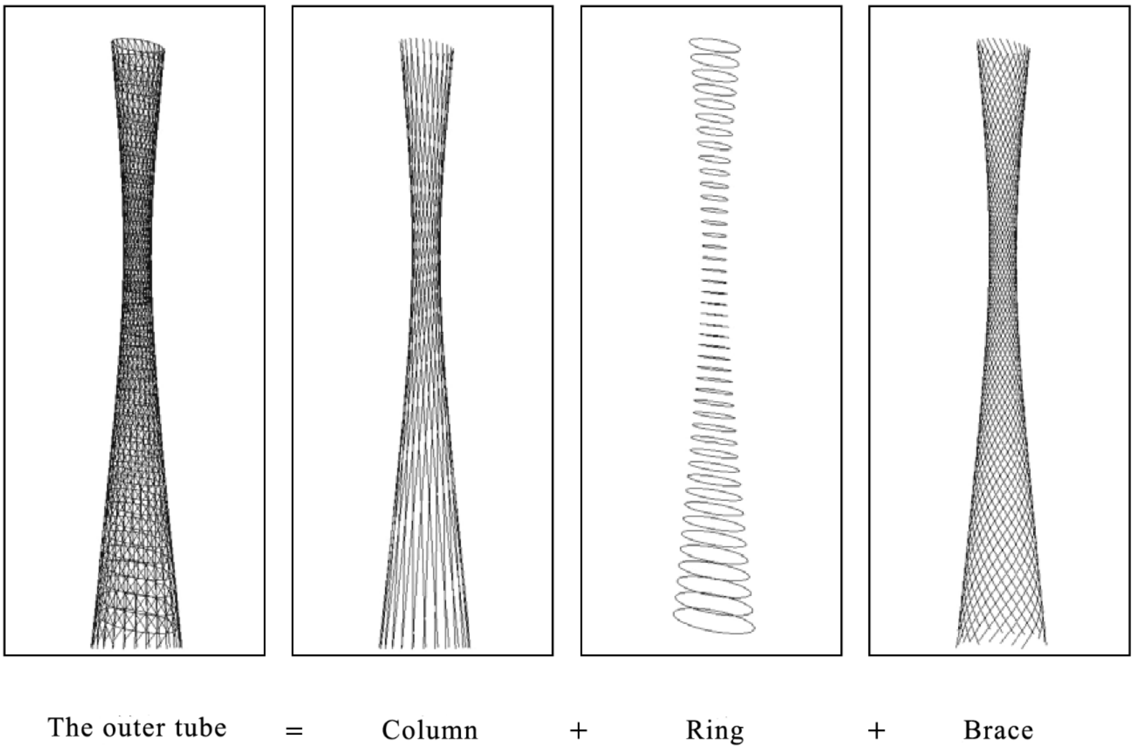

Figure 3-5. Components of the outer tube

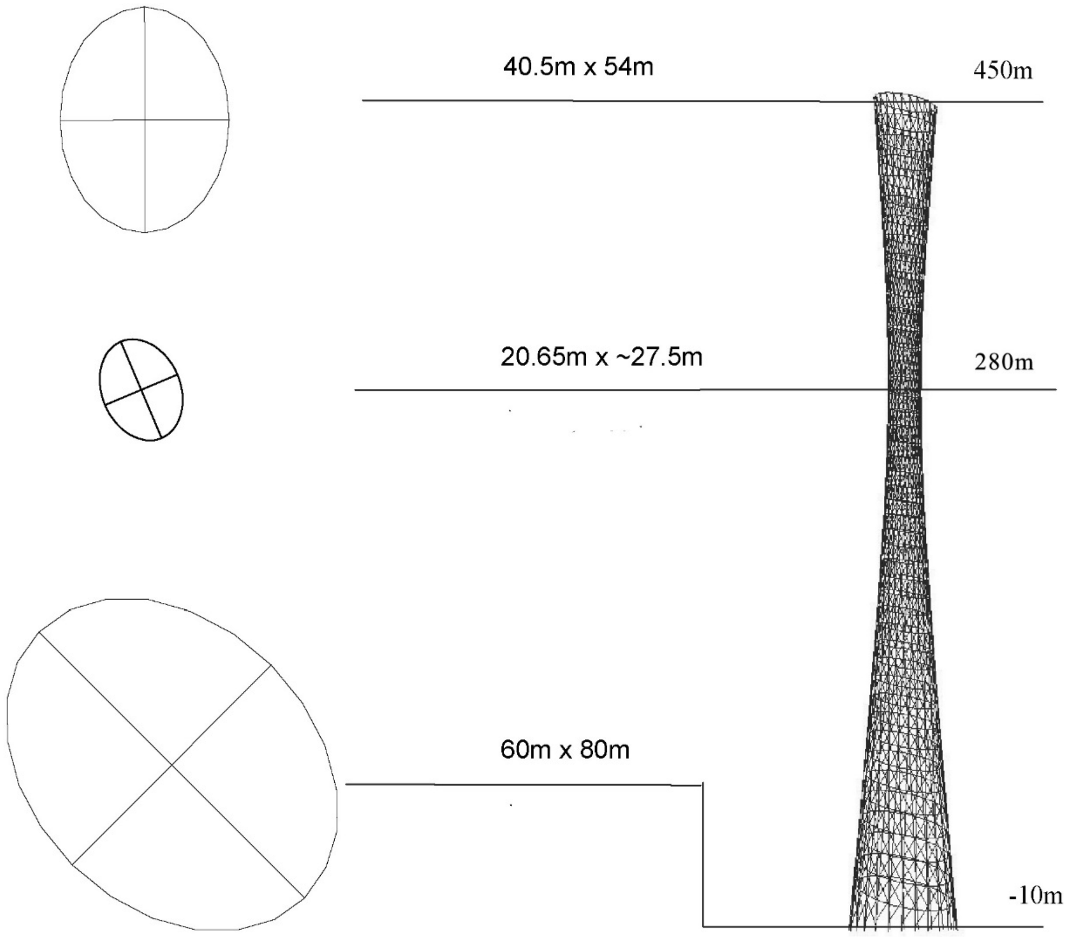

Figure 3-6. Dimension of the oval of the outer tube

There are 37 floors connecting the inner and outer structures that serve for various functions, e.g., television and radio transmission facilities, observatory decks, Ferris wheels, exhibition spaces, shops, revolving restaurants, conference rooms, computer gaming, and 4D cinemas. The floor, which is a composite decking with profiled steel sheet as the permanent bottom formwork and concrete pouring above to a depth of 150mm, does not attach to the outer tube directly. Radiating steel girders of the floor stretch out from the bottom of the floor and connect to the corresponding CFTs of the outer tube through a bolt at each CFT with pin connection. The other end of the girders is welded to the inner tube through an embedded steel corbel with connection of moment resistance. The floor perimeter is enclosed by a curtain wall system (inside the outer tube) attached to the slab. Apart from the floors enclosed with the curtain wall, majority of the inner tube is exposed to outside atmosphere. There are four levels of connection girders without floor at the height of about 204 m, 230 m, 272 m, and 303 m joining the inner tube and the outer tube.

For large-scale civil engineering structures like Canton Tower, long-term SHM systems is able to provide thorough and most reliable information for evaluating structural integrity, durability and reliability throughout the life-cycle and for ensuring optimal maintenance planning and safe operation. In order to assess the structural safety, a sophisticated long-term SHM system has been implemented in parallel with the construction progress for on-line monitoring of the Canton Tower at both construction and service stages.

3.2 SHM system for Canton Tower

A long-term SHM system has been implemented on the Canton Tower by a team from The Hong Kong Polytechnic University (located in Hong Kong) and Sun Yat-Sen University (located in Guangzhou). The SHM system, which consists of 15 different types of over 700 sensors, employs a pioneering SHM practice (as shown in Figure 3-7) that integrates in-construction monitoring and in-service monitoring (Ni et al. 2009a). This on-line SHM system has been devised based on the modular design concept and consists of six functional modules: (i) Sensory System (SS), (ii) Data Acquisition and Transmission System (DATS), (iii) Data Processing and Control System (DPCS), (iv) Structural Health Data Management System (SHDMS), (v) Structural Health Evaluation System (SHES), and (vi) Inspection and Maintenance System (IMS). The SS and DATS are located in the structure, the DPCS, SHDMS and SHES are inside the monitoring center room, and the IMS is a portable system. The integration of these six modules is shown in Figure 3-8.

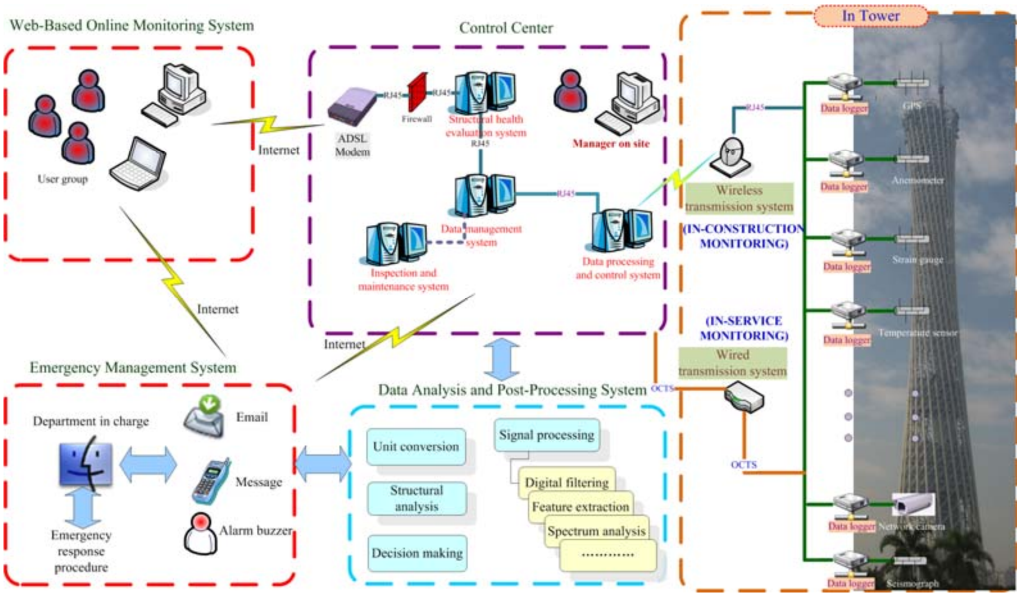

Figure 3-7. Topology of integrated in-construction and in-service monitoring system

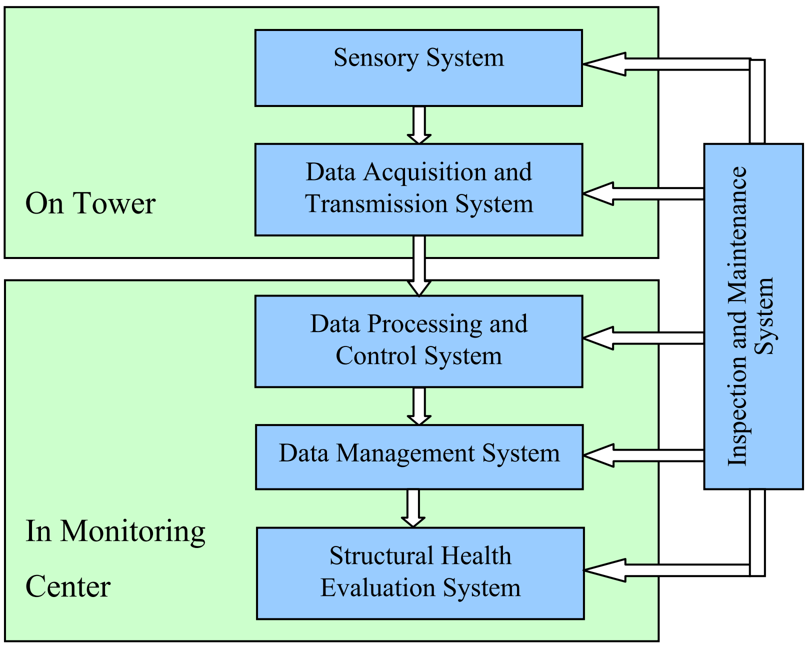

Figure 3-8. SHM system for Canton Tower consisting of six modules

The SS is composed of 15 types of sensors, as list in Table 3-1 and shown in Figure 3-9, which include a weather station, a total station, zenithal telescopes, theodolites, vibrating wire strain gauges, thermometers, accelerometers, level sensors, tiltmeters, corrosion sensors, digital video cameras, fiber optic dynamic strain and temperature sensors, a seismograph, and a GPS. Crucial information including environmental effects (temperature, humidity, rain, air pressure, and corrosion), loading sources (wind seismic, and thermal loading), and structural responses (strain, displacement, inclination, acceleration, and geometric configuration) can be acquired in real time.

The DATS consists of 13 stand-alone data acquisition units (DAUs) (sub-stations) for in-construction monitoring and 6 stand-alone DAUs (sub-stations) for in-service monitoring. The DAUs are assigned at several cross-sections of the Canton Tower to collect the signals from surrounding sensors, digitize the analog signals, and transmit the data into a central room in either wired or wireless manner.

The DPCS comprises high-performance servers located in the central room and data-processing software. It is devised to control the on-structure DAUs regarding data acquisition and pre-processing, data transmission and filing, and display of the data. The DMS comprises an Oracle-driven database system for non-spatial temporal data management and a Geographic Information System (GIS) software system for spatial data management. The SHES is composed of an on-line structural condition evaluation system and an off-line structural health and safety assessment system. The IMS is a laptop-computer-aided portable system for inspecting and maintaining sensors, DAUs, and cabling networks.

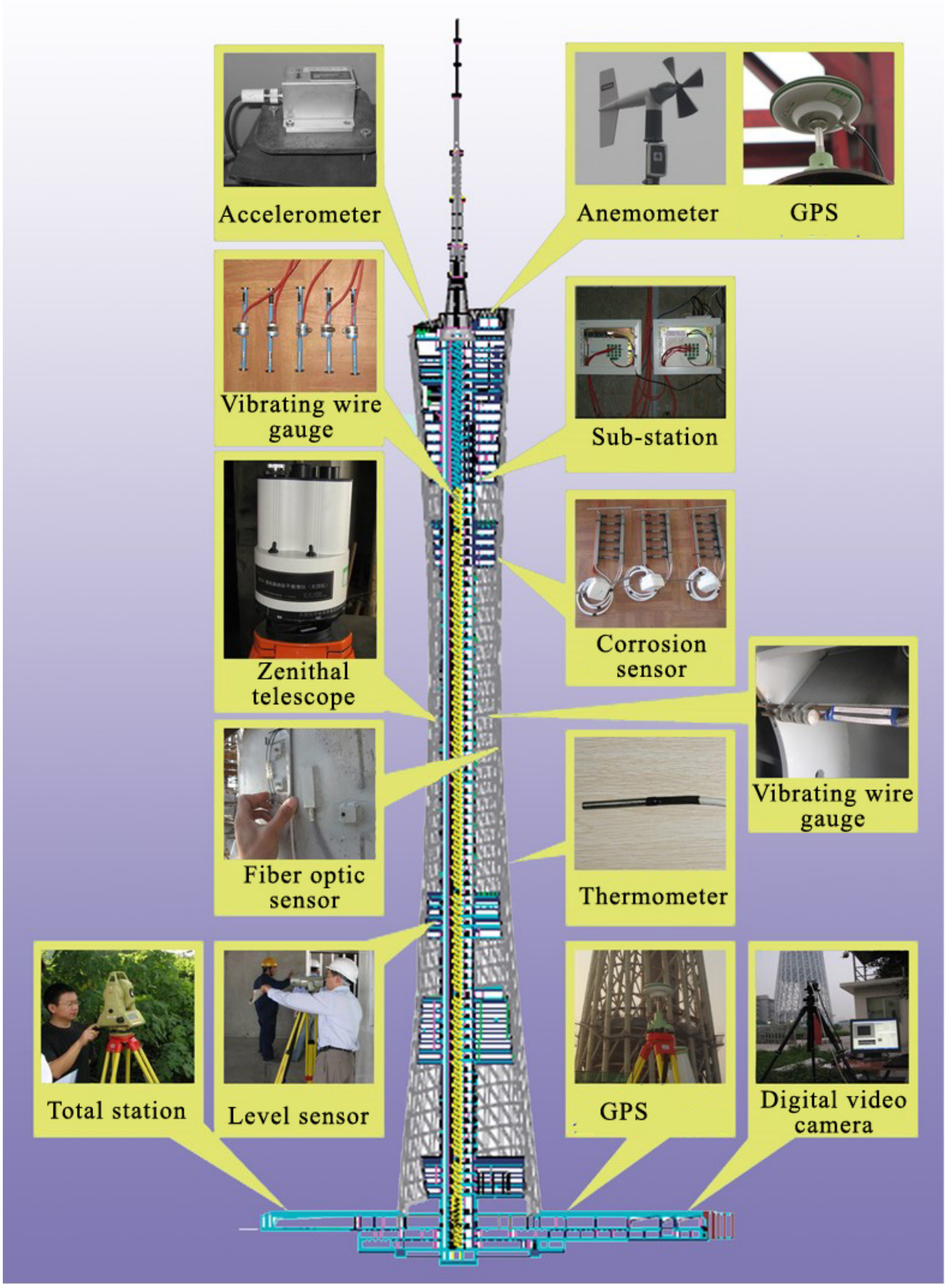

Figure 3-9. Sensor deployment for Canton Tower

Table 3-1. Sensor deployment for Canton Tower

No.	Sensor Type	Monitoring Items	Number of Sensors	Manufacturer/ Model
1	Weather station	Temperature, humidity, rain, air pressure	1	VAISALA/ WXT510
2	Anemometer	Wind speed and direction	2	R M YOUNG/ 05103L
3	Total station	Inclination, leveling, elevation	1	LEICA Geosystems / TCA1800
4	Zenithal telescope	Inclination of tower	2	LAT LASER/ JZC-G
5	Tiltmeter	Inclination of tower	2	LEICA Geosystems / Nivel210
6	Level sensor	Leveling of floors	2	LEICA Geosystems / Sprinter 200
7	Theodolite	Elevation	2	KOLIDA/ET-02
8	GPS	Displacement	2	LEICA Geosystems / GPS1230
9	Vibrating wire gauge	Strain, shrinkage and creep	416	GEOKON/ GK4000, GK4200
10	Thermometer	Temperature of structure	216	FUMIN Measurements/PT100
11	Digital video camera	Displacement	3	PROSILICA/GE2040C
12	Seismograph	Earthquake motion	1	TOKYO SOKUSHIN/ SPC-51C
13	Corrosion sensor	Corrosion of reinforcement	3	S+R/ Anode Ladder
14	Accelerometer	Acceleration	22	TOKYO SOKUSHIN/ AS-2000C
15	Fiber optic sensor	Strain and temperature	120	MICRON OPTICS/ OS310s, sm130-200
Total			795	

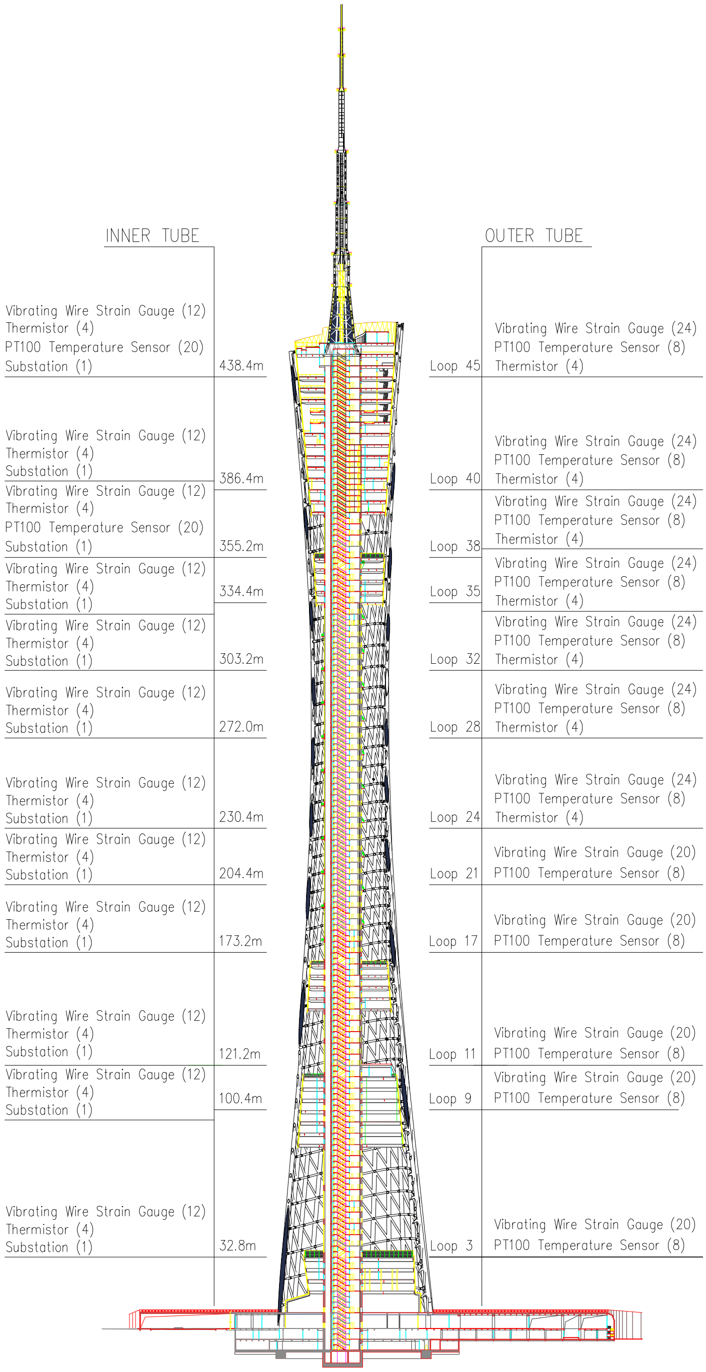

Figure 3-10. Layout of the strain and temperature monitoring system

The strain and temperature monitoring subsystem employed during the construction stage consisted of vibrating wire strain gauges, thermal sensors, and substations distributed along 12 sections at different heights. As shown in Figure 3-10, a total of

12 critical cross-sections have been selected for strain and temperature monitoring. They are at the levels of 32.8 m, 100.4 m, 121.2 m, 173.2 m, 204.4 m, 230.4 m, 272.0 m, 303.2 m, 334.4 m, 355.2 m, 376.0 m, and 433.2 m high, and designated as section 1 to section 12, respectively. These elevations corresponded to Ring Nos. 3, 9, 11, 17, 21, 24, 28, 32, 35, 38, 40, and 45 of the outer tubular structure. The selected cross-sections are expected to suffer large stresses under certain construction and in-service loadings or experience an abrupt change in lateral stiffness. They were determined by FE analysis of the structure at critical construction stages and the completed stage. The data on each section are collected by the corresponding substations and then transmitted to a control room.

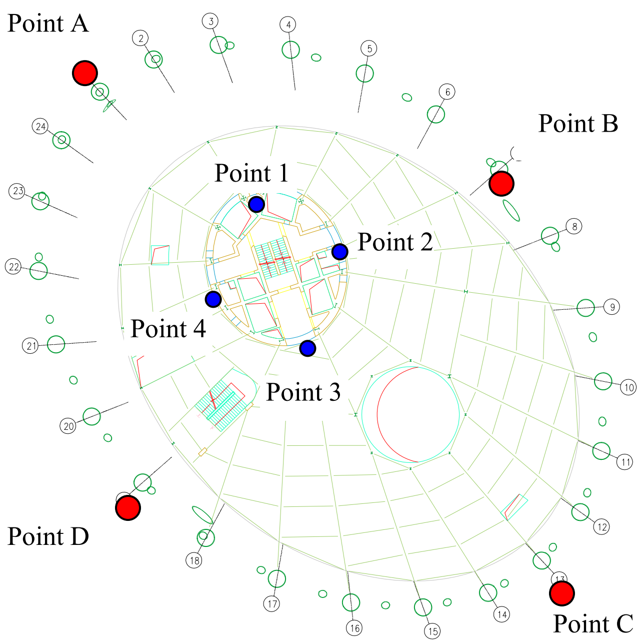

Figure 3-11. Location of strain and temperature monitoring points at one critical section

At the inner tube, as shown in Figure 3-11, four points (denoted as Point 1 to 4) at each critical section are installed with a 45-degree strain rosette, each consisting of three Geokon vibrating wire strain gauges (Geokon 4200) to measure the strain and temperature of the concrete wall. Figure 3-12 shows the installation of a typical strain rosette in the RC wall of the inner tube with firm protection. Figure 3-12 (a) is a photograph of an original Geokon 4200 gauge. To measure the strain of the concrete rather than that of the rebar, the vibrating wire strain gauges were coated with cement as shown in Figure 3-12 (b) the day before the concrete was poured. All the gauges were inspected and tested using a portable readout box. A strain rosette was then attached to the rebars (Figure 3-12 (c)) to avoid movement while concrete was poured and to measure the strain in three directions at each point. The cables were then protected by stainless galvanized steel pipes embedded in the concrete floor (Figure 3-12 (d)). This protects the cables from causal damage.

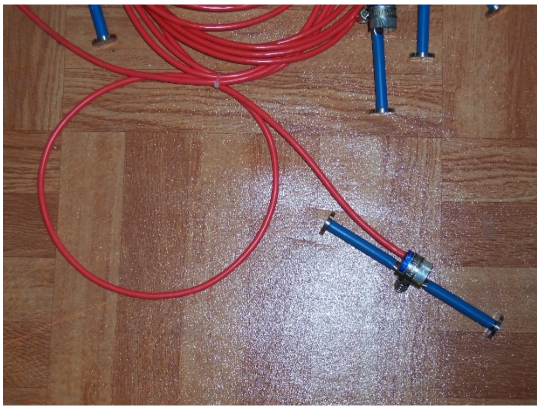

(a) Original vibrating wire strain gauge

(b) Cement coating

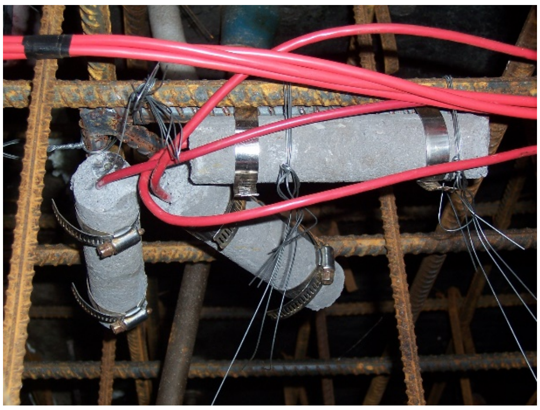

(c) A strain rosette in the inner tube

(d) Protection of cables

Figure 3-12. Installation of vibrating wire strain gauges in the inner tube

The SHM project began from June of 2007, when the inner tube has been constructed to the height of about 120 m. Therefore the section of 121.2 m was firstly equipped with gauges embedded inside the inner core wall. The upper sections were installed with embedded gauges along with the progress of the construction activity, while the sections of 32.8 m and 100.4 m were installed with sensors (Geokon 4000) on the exterior surface of the core wall as concrete construction had been completed at that time. The gauges were attached to two grouted concrete mounting blocks on the wall.

For the outer structure, as shown in Figures 3-13, four points (denoted as Point A ~ Point D in Figure 3-11) are monitored at each section by vibrating wire strain gauges as well. There are six strain gauges (Geokon 4000) at every monitoring location: three of them (denoted as S1 to S3) are used to monitor the strain at the external surface of the CFT, one for (denoted as S4) strain and temperature inside the CFT, one for ring member (denoted as S5) and one for brace (denoted as S6). In addition, two thermal sensors (denoted as S7 and S8) are installed at the opposite surface of the four CFTs to measure the surface temperature of the CFTs while inside temperature is obtained through the vibrating wire temperature sensor. Figure 3-14 shows the installation of a typical strain rosette in surface of the outer tube with firm wire protection. The strain gauges were attached on the surface of the steel tube in the fabrication factory, as shown in Figure 3-14(a). The cables were then protected by stainless steel cases after finishing assembling the steel tubes (Figure 3-14(b)).

A wireless system has been developed for synchronous acquisition of temperature data of the reinforced concrete inner structure and real-time data transmission from the data acquisition units (sub-stations) to the site office during the construction period. The sampling rate for each sensor is set as one data per minute in normal circumstances and can be switched to one data per second (1 Hz) during typhoons and other extreme events.

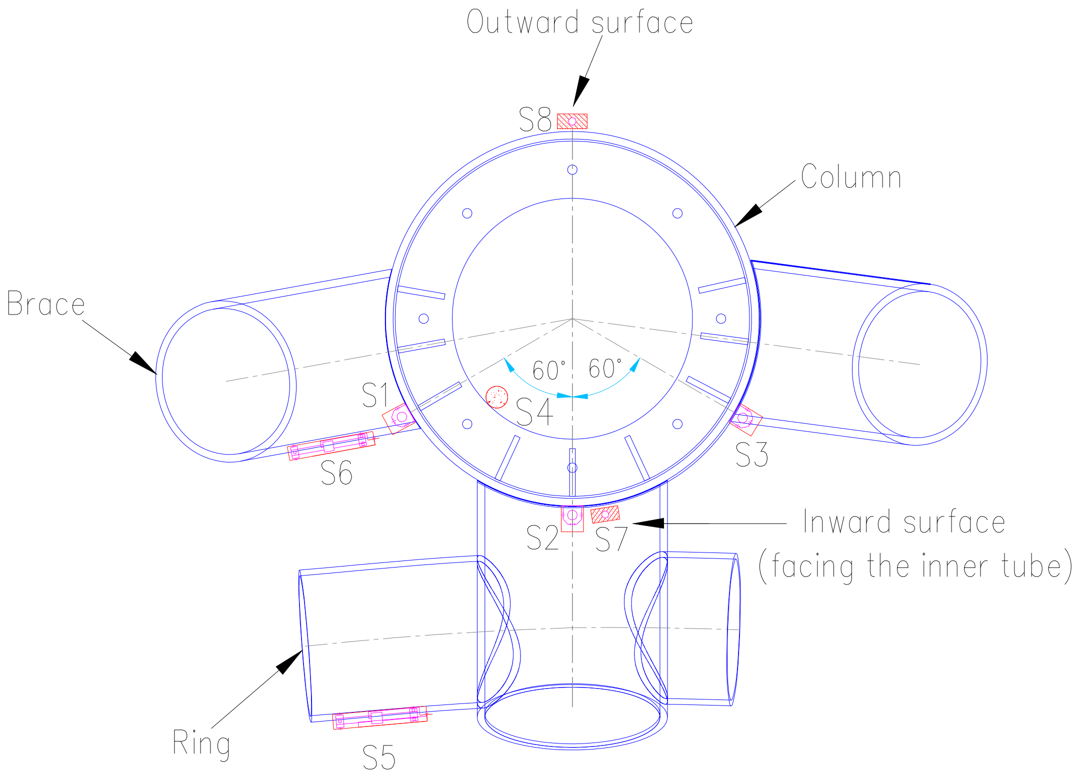

Figure 3-13. Layout of strain and temperature sensors at the out tube

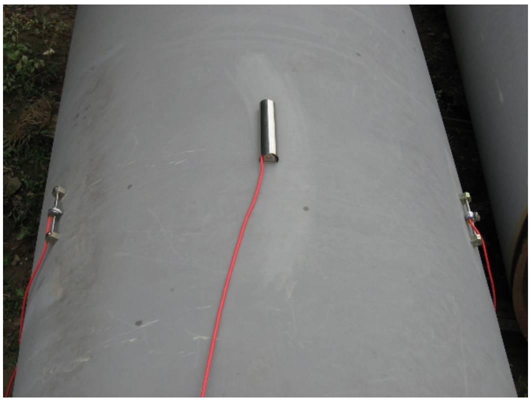

(a) Attached strain gauges

(b) Protection of the cables

Figure 3-14. Installation of vibrating wire strain gauges on the outer tube

A GPS system was installed to monitor the displacement of the Canton Tower. The reference station (Figure 3-15 (a)) was installed 3 m above the sightseeing platform at 10.2 m. The rover station (Figure 3-15 (b)) was installed on a chimney at approximately 6 m above the platform at 459.2 m. In addition, a Leica Nivel 210 inclinometer (Figure 3-16) was installed at the height of 443.8 m to measure the tilt angles (or inclination from the horizontal) along the short and long axes of the inner tube. The sampling rate of the GPS and inclinometer was set to 1 Hz.

(a) Reference station

(b) Rover station

Figure 3-15. GPS installed on the structure

Figure 3-16. Inclinometer installed on the structure

CHAPTER FOUR

TEMPERATURE DISTRIBUTION AND TEMPERATURE-INDUCED RESPONSE OF CANTON TOWER

4.1 Thermal analysis of Canton Tower

4.1.1 Verification of the Solar Radiation Calculation Model

For supertall structures like Canton Tower, the temperature distribution on these type of structures is normally very complicated. By conducting the heat transfer analysis with proper boundary conditions, the temperature distribution can be obtained. The boundary conditions especially the solar radiation intensity in previous studies are normally obtained through the solar radiation calculation model like Eq. (2-22) which is seldom verified with the measurement. In this study, to verify the effectiveness of the simulated solar radiation obtained from Eq. (2-22), a field test the place of which shown in Figure 4-1 was carried out to measure the daily solar radiation of Canton Tower on 17th January 2013.

As illustrated in Figures 4-2, a meteorological station was temporarily installed near the Canton Tower. The meteorological station was composed of a total solar radiometer, diffuse solar radiometer, reflected solar radiometer to measure the solar radiation, a thermohygrometer to measure the humidity and air temperature, and an anemograph to measure the wind speed and wind direction.

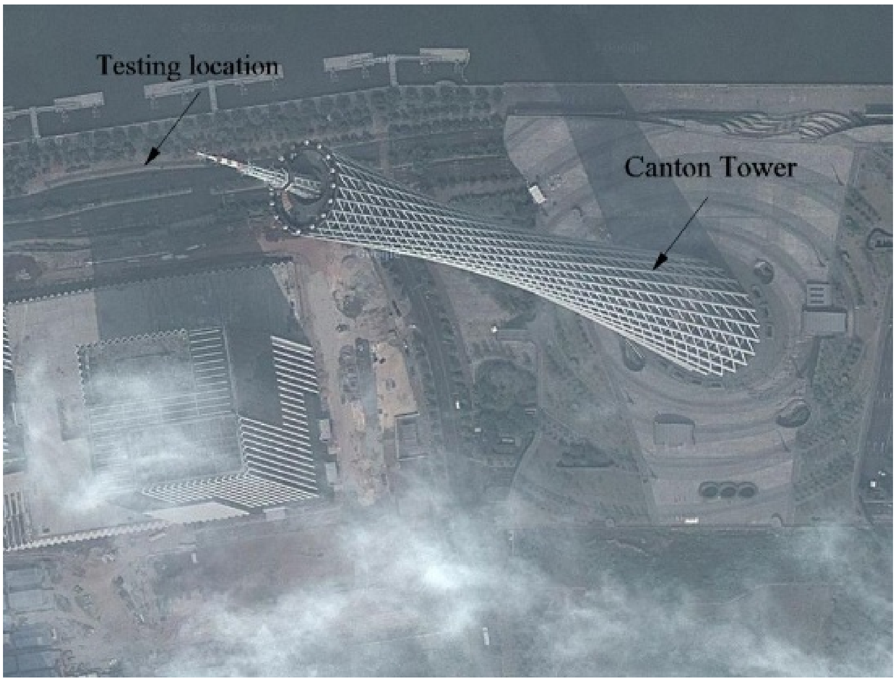

Figure 4-1. Satellite figure of testing place

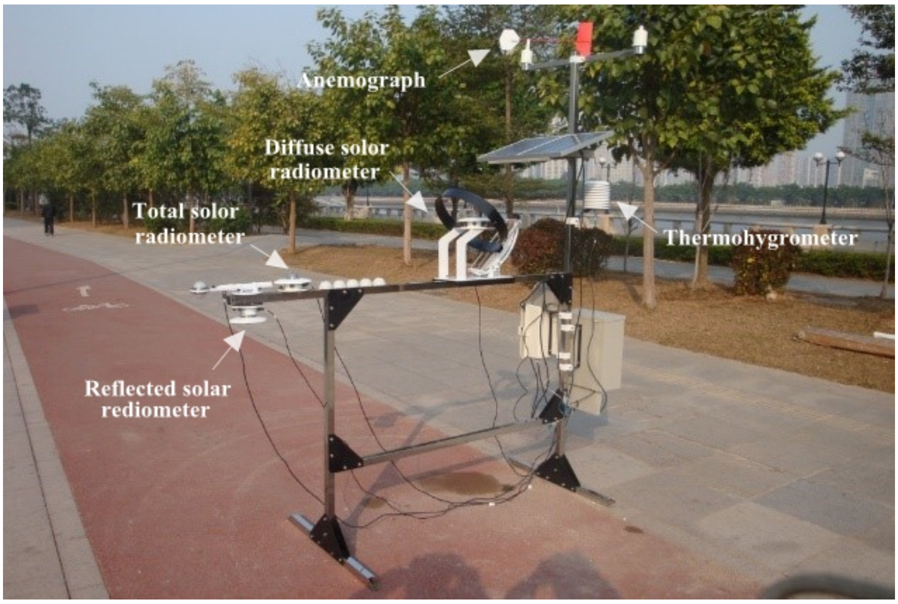

Figure 4-2. Meteorological station at the testing location

The test started at 9:15 and ends at 16:30. Figure 4-3 compares the measured and simulated solar irritation in the horizontal plane. It can be noticed that the two curves have the same variation trend and the maximum solar radiation occurred at almost the same time. In particular, the measured maximum solar radiation was 570.1 W/m^2; 55 W/m^2 less than the simulated one. The solar radiation calculation model normally considers the ideal weather condition (sunny day without cloud). The comparison shows that the measured and simulated solar radiations have 10% difference, which is acceptable in engineering applications. Therefore the solar radiation model can be satisfactorily applied to calculate the solar radiation intensity at the surface of the structure in any direction.

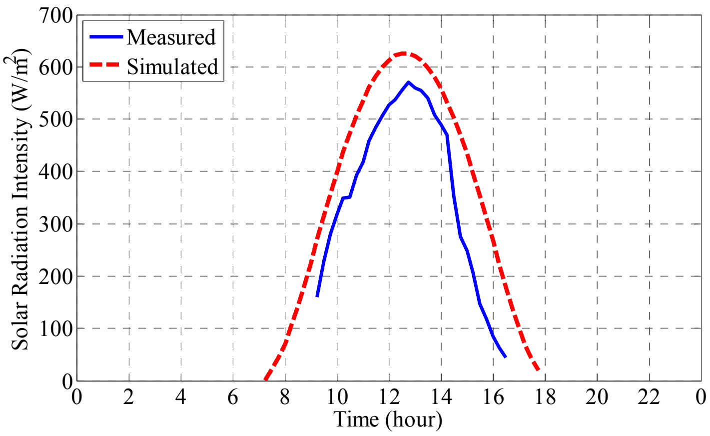

Figure 4-3. The measured and simulated solar radiation intensity on the horizontal plane on 17th January 2013

4.1.2 Finite Element Model

The thermal variation of the tube in vertical direction is assumed to be insignificant and thus one typical section for inner tube, one for the column of the outer tube, and one for the ring and brace members are investigated here. The FE models for the above are established in the commercial general-purpose FE analysis packages ANSYS (ANSYS 14.0 2011). The inner tube covered with functional floors and do not directly receive the solar radiation. The heat transfer analysis is only conducted on those sections without functional floors. The shear wall of the inner tube, the CFT column of the outer tube, and the ring and brace members are modeled using the two-dimensional thermal-type plane elements (PLANE 55 in ANSYS), as shown in Figure 4-4, 4-5, 4-6, respectively. In particular, the inner tube model consists of 8453 nodes and 7192 elements; the CFT column model consists of 4179 nodes and 3759 elements; and the ring and brace model has 4179 nodes and 3759 elements.

As the cross-section of the inner-tube is oval and that of the outer tube is circle, the surfaces of the section are divided into different regions and are subject to different solar radiation. Table 4-1 lists the material parameters for the thermal analysis. The temperature measured by the thermistor embedded in the vibration wire installed in the middle of the outside shear-wall (as shown in Figure 3-12) and the thermal sensors installed at the surface of the four CFTs (as shown in Figure 3-13) are utilized to verify the numerical results. For the ring and brace members, no thermal sensors are installed and only numerical results are shown here.

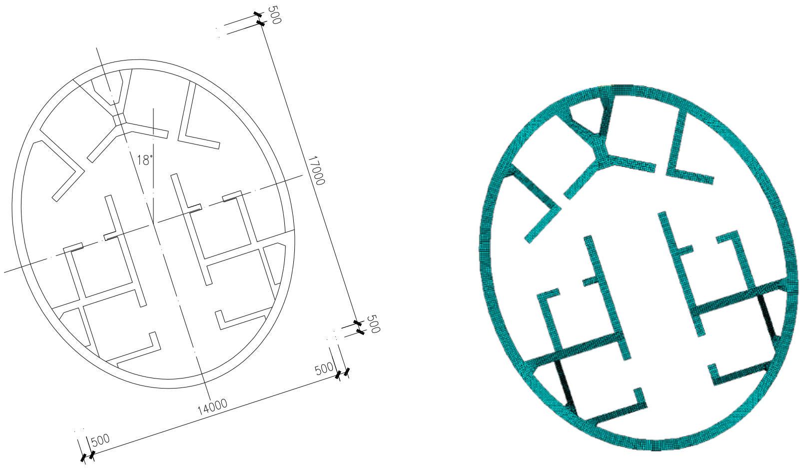

(a) Cross-section (b) Finite element model

Figure 4-4. Finite element model for the inner concrete tube (unit: mm)

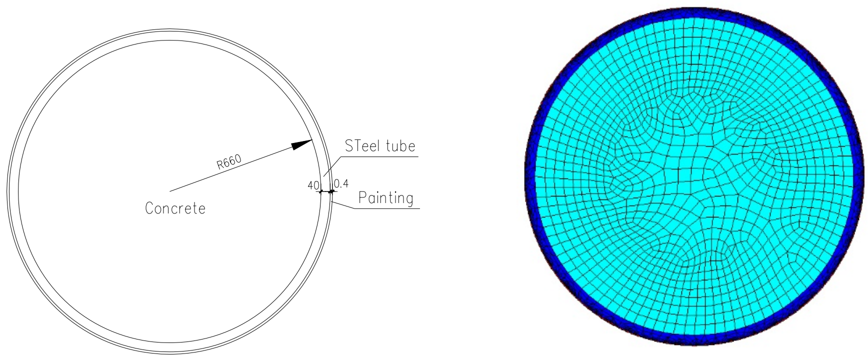

(a) Cross-section (b) Finite element model

Figure 4-5. Finite element model for the CFT column (unit: mm)

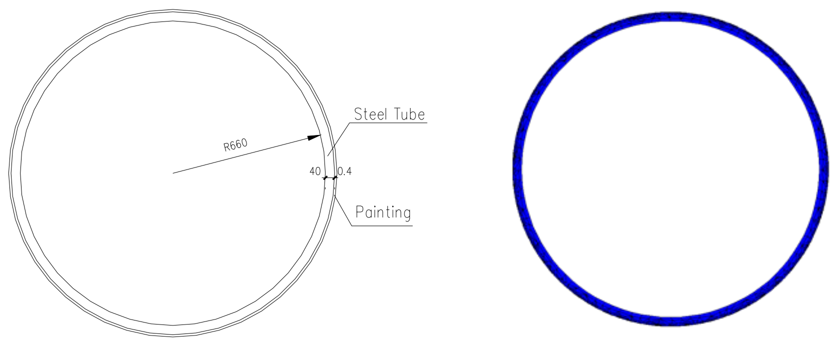

(a) Cross-section (b) Finite element model

Figure 4-6. Finite element model for brace and ring members (unit: mm)

Table 4-1. Material parameters

Parameter	Concrete	Steel
Thermal conductivity (k, W/(m℃))	1.5	54
Density (ρ, kg/m^3)	2400	7850
Heat capacity (c, J/(kg℃))	950	450
Absorptivity coefficient (α)	0.65	0.7
Emissivity coefficient (ε)	0.85	0.8

4.1.3 Comparison between the Simulated and Measured Temperature

The initial condition T_0 described in Eq. (2-2) normally can't be accurately obtained from limited temperature measurement points. Therefore, one-day transient heat transfer pre-analysis is conducted to get the initial condition of the next day. The initial temperature in the pre-analysis on each component is deemed as uniform distribution and the value of which is the air temperature at 0:00 in the mid-night. 13th to 14th April 2013 and 30th to 31st December 2013 in different seasons are chosen to conduct the heat transfer analysis.

As the cross-section of the inner-tube is oval and that of the outer tube is circle (see Figure 4-7), different facades of the section receive different levers of solar radiation. Figure 4-8 shows the calculated solar radiation intensity at the temperature monitoring point of the inner tube at cross-section 303.2m on 14th April 2013 by Eq. (2-23). It can be noticed that the peak values of the solar radiation intensity at each point occurred at different time in one day. After sunrise, the solar radiation intensity at Point 2 reached the maximum value of 624 W/m^2 at 8:30 firstly, and then the solar radiation intensity at Point 3 reached the maximum value of 393 W/m^2 at 11:00. When the sun moved to the west in the afternoon, the solar radiation intensity at Point 4 and 1 reached the maximum value of 658 W/m^2 and 206 W/m^{2}at 15:45 and 16:30, respectively.

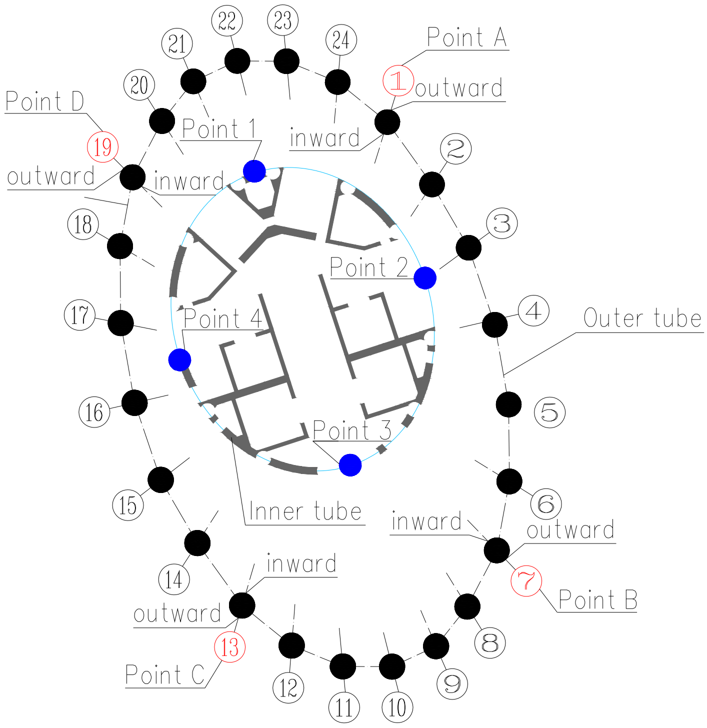

Figure 4-7. Location of temperature monitoring points at one critical section of 303.2m high

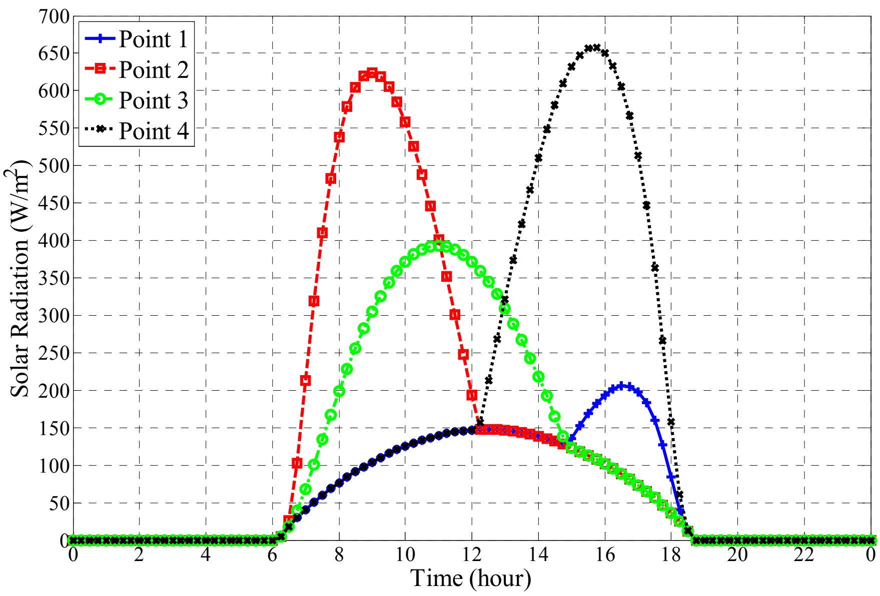

Figure 4-8. Solar radiation intensity at the temperature monitoring point of the inner tube at cross-section 303.2m on 14th April 2013

Figure 4-9 shows the calculated solar radiation intensity at the temperature monitoring point of the inner tube at cross-section 303.2m on 31st December 2013. The daily variation of the solar radiation intensity at each point on 31st December 2013 appears some difference to that on 14th April 2013. The solar radiation intensity at Point 1 reached the maximum value at 9:30 firstly, one hour later than that on 14th April 2013. The maximum value is 390 W/m^2, 234 W/m^2 less than that on 14th April 2013. The solar radiation intensity at Point 2 reached the maximum value of 745 W/m^2 at 11:30, 352 W/m^2 larger than that on 14th April 2013. When the sun moved to the west in the afternoon, the solar radiation intensity at Point 3 reached the maximum value of 613 W/m^2 at 15:15, closer to that on 14th April 2013. There are only diffuse and reflected solar radiations at Point 4, so the solar radiation intensity at Point 1 reached the maximum value of 112 W/m^2 at 12:15.

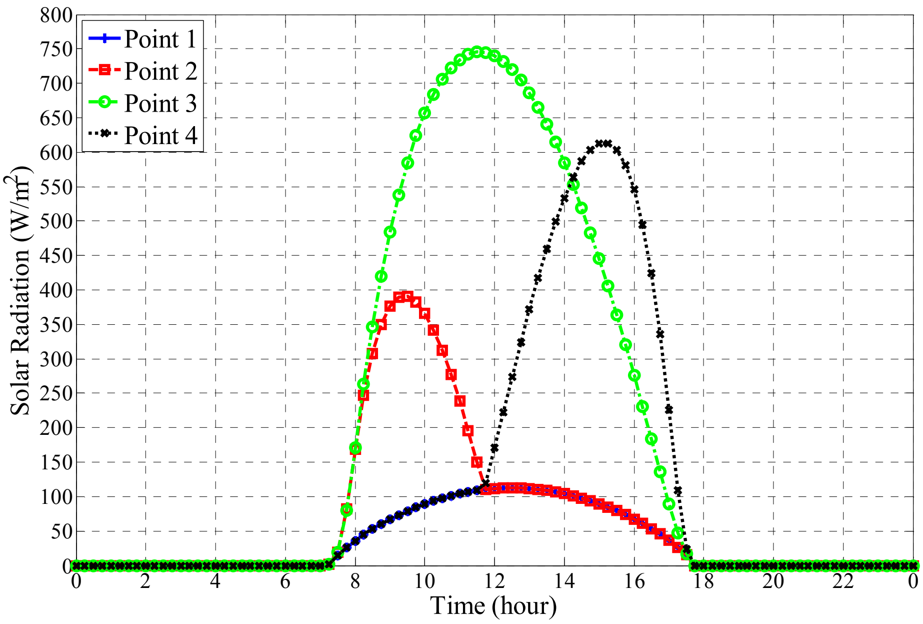

Figure 4-9. Solar radiation intensity at the temperature monitoring point of the inner tube at cross-section 303.2m on 31st December 2013

These differences between the above two days are mainly due to the relative position between the sun and Canton Tower. The sun moved to the south in winter, making that the façade at Point 3 receive more direct solar radiation, the façade at

Point 2 receive less direct solar radiation, and the façade at Point 4 receive no direct solar radiation.

The solar radiation intensity at different facades of the inner tube can be also calculated by Eq. (2-23) and the boundary conditions expressed in Eq. (2-31) are obtained. With the FE model and the boundary condition, the temperature distributions of the reinforced concrete inner tube are obtained through the transient heat transfer analysis.

Figures 4-10 and 4-11 compare the measured and simulated temperature at the measurement points (Point 1 to Point 4 shown in Figure 4-7) 303.2m cross-section for the inner tube on 14th April and 31st December 2013, respectively. Both of these two days are typical sunny days. It is observed that the simulated variation trend of temperature is similar to that of the field measurement. The daily variation of the temperature in the inner tube is rather small, less than 2.5°C. The peak temperature occurred in the night and lagged behind the air temperature, which is mainly due to the small thermal conductivity of the concrete.

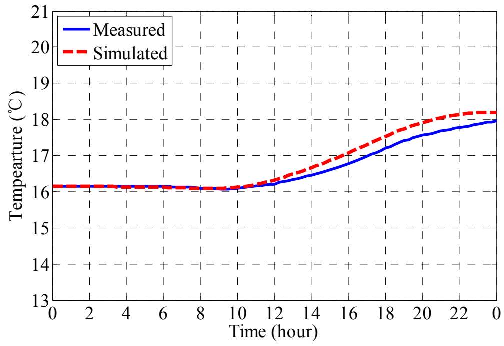

(a) Point 1

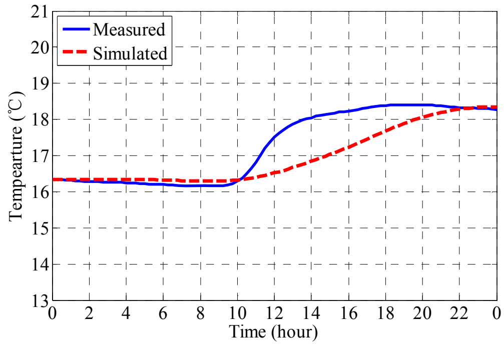

b) Point 2

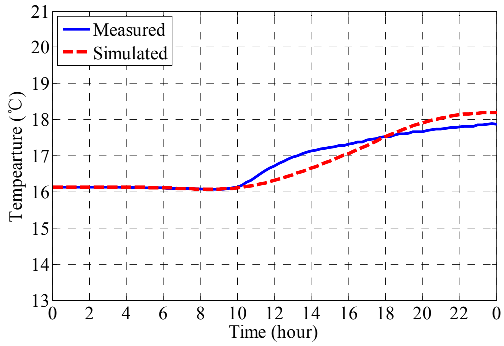

(c) Point 3

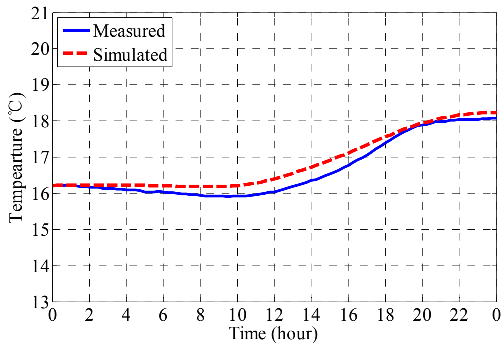

(d) Point 4

Figure 4-10. Measured and simulated temperature of the inner tube at cross-section 303.2m on 14th April 2013

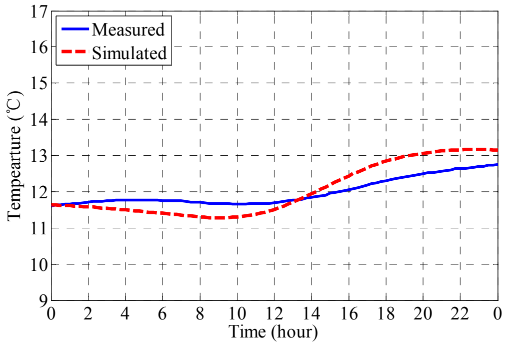

(a) Point 1

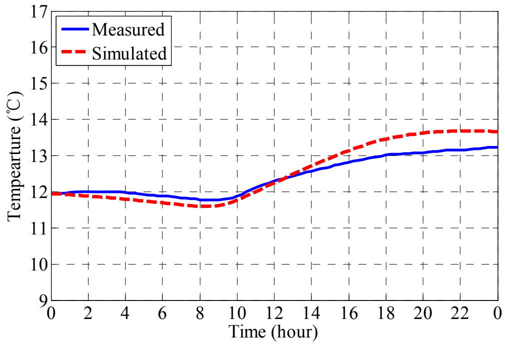

b) Point 2

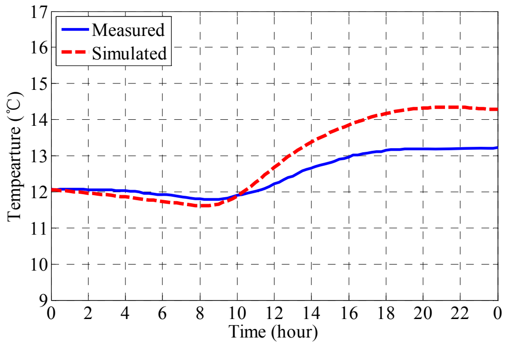

(c) Point 3

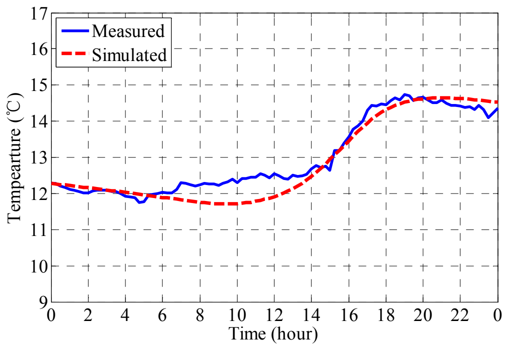

(d) Point 4

Figure 4-11. Measured and simulated temperature of the inner tube at cross-section 303.2m on 31st December 2013

Similarly, as the cross-section of the outer tube is circle (see Figure 4-7), different facades of the section receive different levers of solar radiation. Figure 4-12 shows the calculated solar radiation intensity at the outward façade of the temperature monitoring point on the column of the outer tube at cross-section 303.2m on 14th April 2013 by Eq. (2-23).

It can be noticed that the peak values of the solar radiation intensity at each point occurred at different time in one day. After sunrise, the solar radiation intensity at the outward side of Point A located in the east reached the maximum value of 457 W/m^2 at 8:45 firstly, and then the solar radiation intensity at Point B reached the maximum value of 559 W/m^2 at 9:45. When the sun moved to the west in the afternoon, the solar radiation intensity at Point C and D located in the west reached the maximum value of 559 W/m^2 and 456 W/m^2 at 15:15 and 16:15, respectively.

The inward sides of the four monitoring points are almost sheltered from the sun and can't receive the direct solar radiation. Only diffuse and reflected solar radiation are absorbed in the inward side, as shown in Figure 4-13. The solar radiation intensities at the inward façade of the four points have the same values and the maximum value is 148 W/m^2.

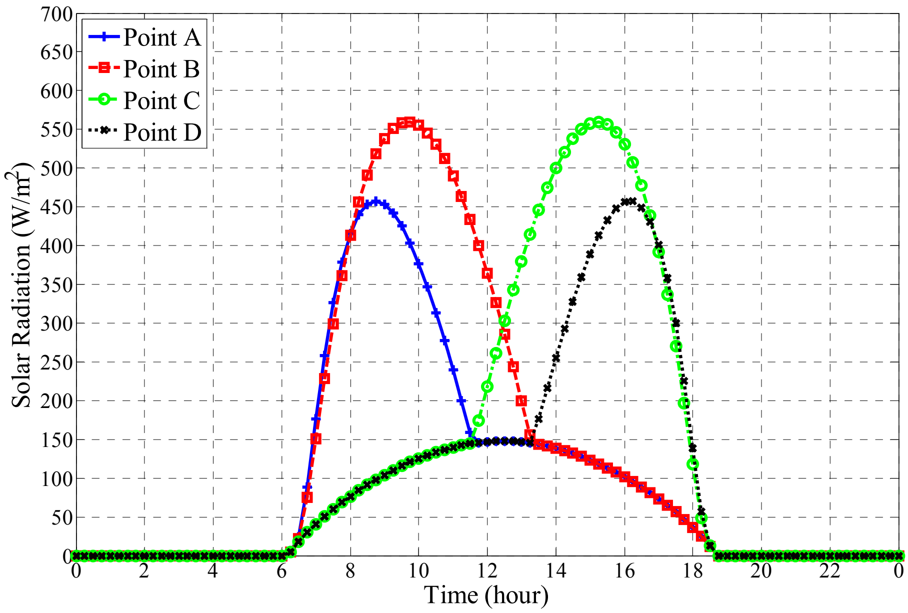

Figure 4-12. Solar radiation intensity at the outward façade of the temperature monitoring point of the outer tube at cross-section 303.2m on 14th April 2013

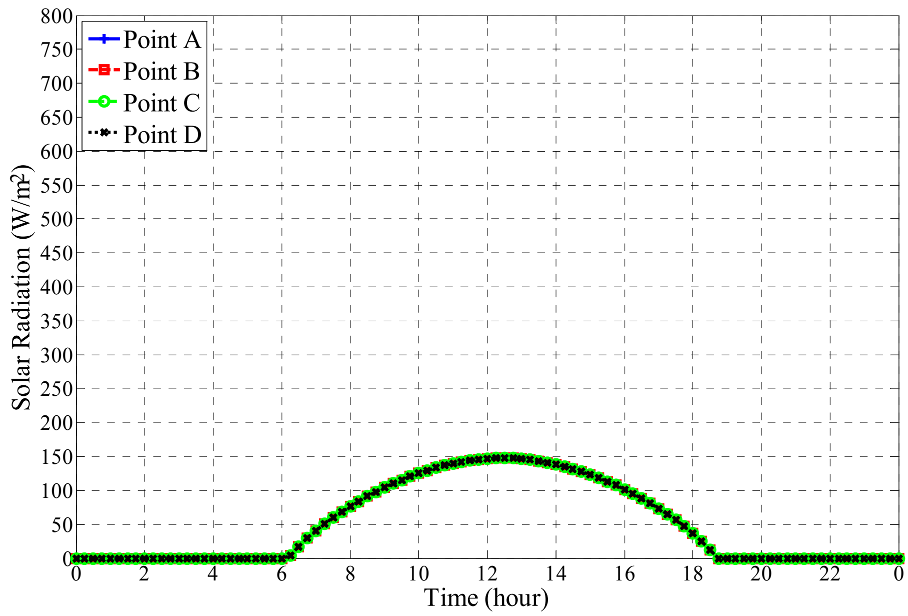

Figure 4-13. Solar radiation intensity at the inward façade of the temperature monitoring point of the outer tube at cross-section 303.2m on 14th April 2013

Figure 4-14 shows the calculated solar radiation intensity at the outward façade of the temperature monitoring point on the column of the outer tube at cross-section 303.2m on 131st December 2013 by Eq. (2-23).

It can be noticed observed that the solar radiation intensity at each point on 31st December 2013 appears some difference to that on 14th April 2013. The solar radiation intensity at Point B reached the maximum value at 10:30 firstly, 45 minutes later than that on 14th April 2013. The maximum value is 732 W/m^2, 172 W/m^2 larger than that on 14th April 2013. When the sun moved to the west in the afternoon, the solar radiation intensity at Point C reached the maximum value of 732 W/m^2 at 14:15, 245 W/m^2 larger than that on 14th April 2013. The maximum solar radiation intensity at the outward faced of the Point A and Point B are very small. This is mainly because the sun moved to the south in winter, most of the façades at Point 1 and 4 received very little or no direct solar radiations.

Similarly, only diffuse and reflected solar radiation are absorbed in the inward side, as shown in Figure 4-15. The maximum solar radiation intensity at the four monitoring is 113 W/m^2, 35 W/m^2 than that on 14th April 2013.

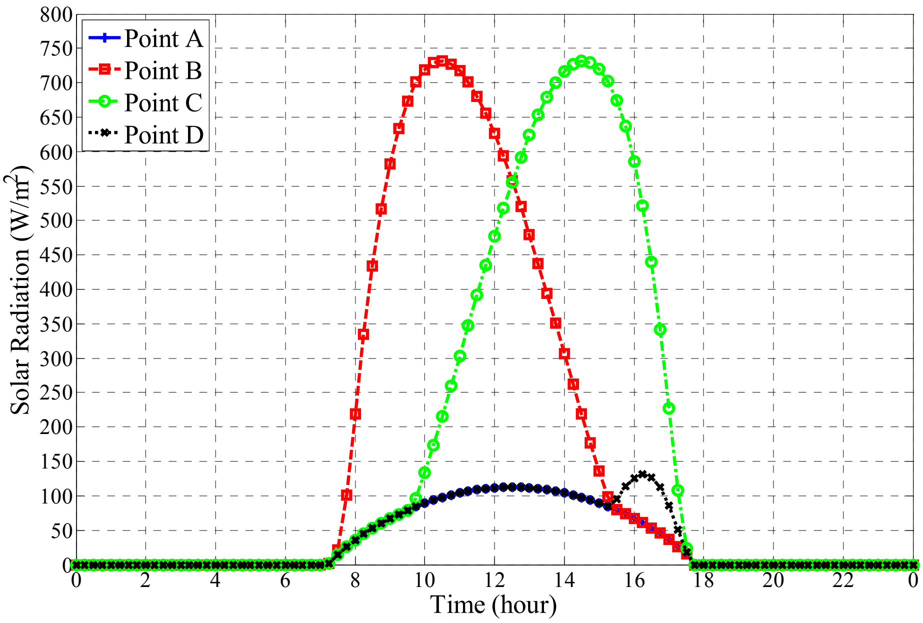

Figure 4-14. Solar radiation intensity at the outward façade of the temperature monitoring point of the outer tube at cross-section 303.2m on 31st December 2013

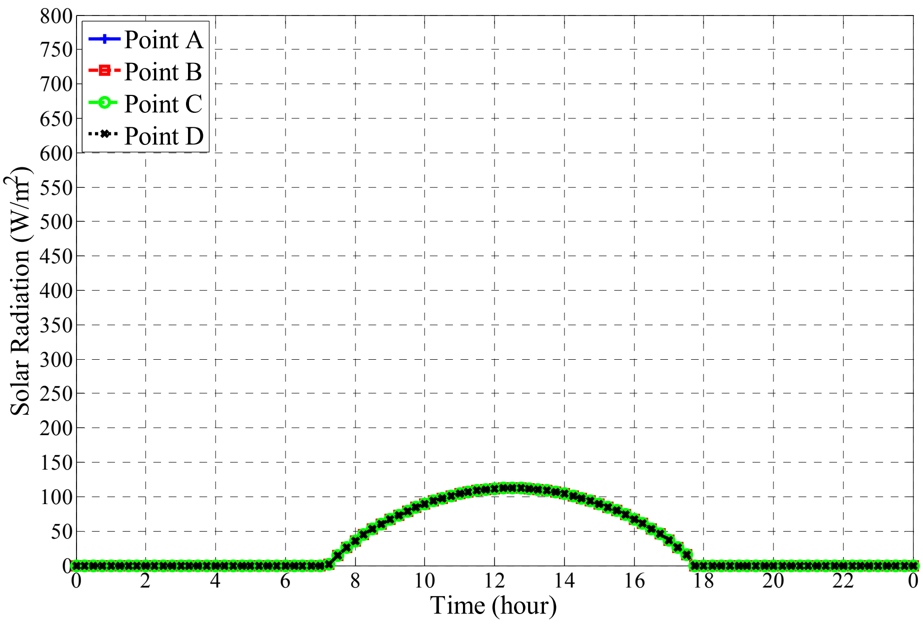

Figure 4-15. Solar radiation intensity at the inward façade of the temperature monitoring point of the outer tube at cross-section 303.2m on 31st December 2013

Figures 4-16 and 4-17 compare the measured and simulated temperature at the measurement points (Point A to Point D as shown in Figure 4-7) around the height of 303.2m on 14th April and 31st December 2013, respectively. The daily variation of the surface temperature, especially the measurement point exposed to the sun, is relatively large, approximately 10 °C on 14th April and 12 °C on 31st December 2013 for column 13 (southeast). Both simulated and measured temperature curves have a similar variation trend, although there are some discrepancies. The curves for the inner side of four columns exhibit the similar variation trend and the difference is 10 °C approximately. The measured daily temperature variations are approximately 4 °C on 14th April and 2 to 3 °C on 31st December 2013. The peak temperature of the outer side for column 7 located in southeast occurred at 12:00. After the sun moved to the southwest in the afternoon, temperature of the outer side for column 13 located in southwest and column 19 located in the northwest arrived at their peak values at around 17:00. The measured temperature difference at the surface of the outer side between columns 7 and 19 was approximately 5 °C in the noon. The difference between columns 1 and 13 was approximately 6 °C on 14th April and 9 °C on 31st December 2013 in the afternoon.

The above observations show that the developed FE model is able to satisfactorily simulate the temperature distributions of the reinforced concrete inner tube and the CFT columns of the outer tube. The temperature difference between different facades is more significant in winter than that in other seasons.

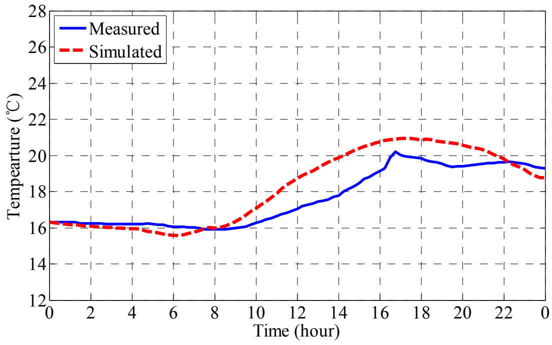

(a) Inward of column 1 (Point A)

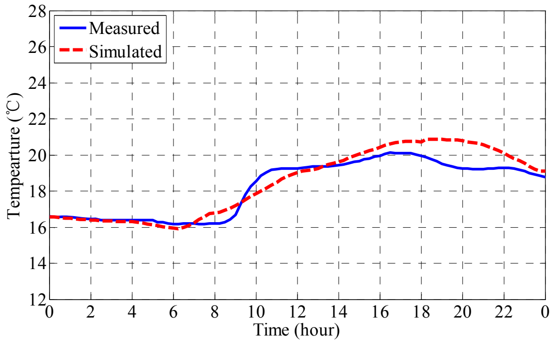

b) Outward of column 1 (Point A)

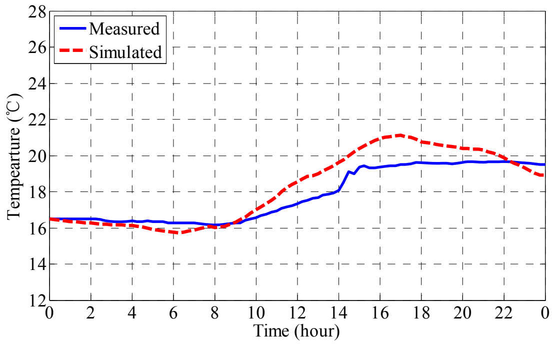

(c) Inward of column 7 (Point B)

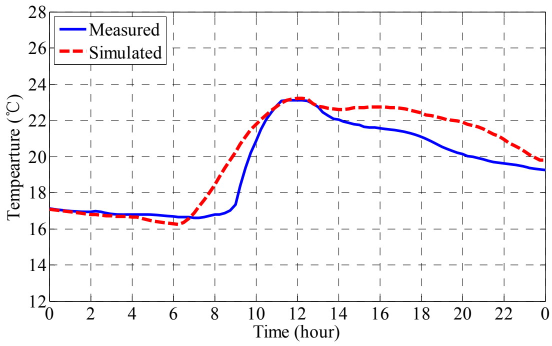

(d) Outward of column 7 (Point B)

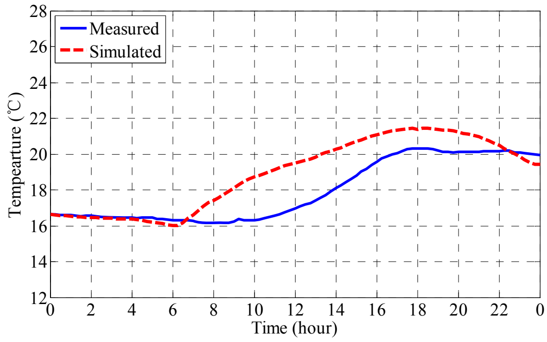

(e) Inward of column 13 (Point C)

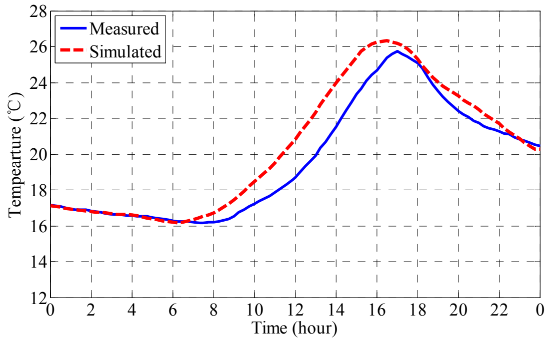

(f) Outward of column 13 (Point C)

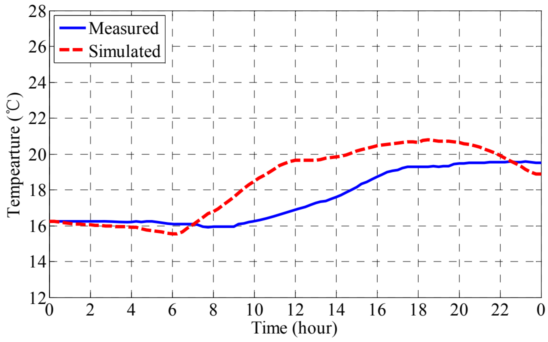

(g) Inward side of column 19 (Point D)

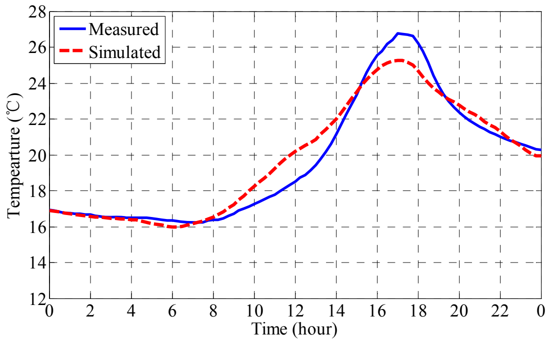

(h) Outward of column 19 (Point D)

Figure 4-16. Measured and simulated temperature of the CFT column surfaces at cross-section 303.2m on 14th April 2013

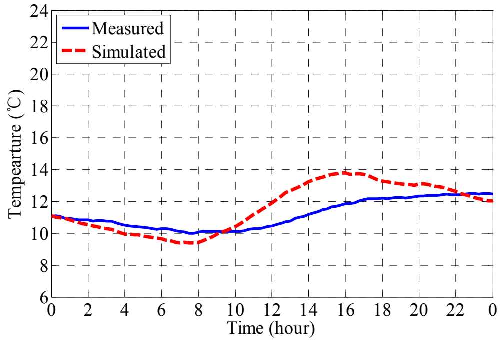

(a) Inward side of column 1 (Point A)

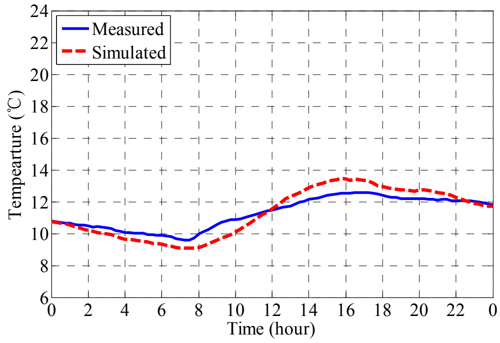

b) Outward of column 1 (Point A)

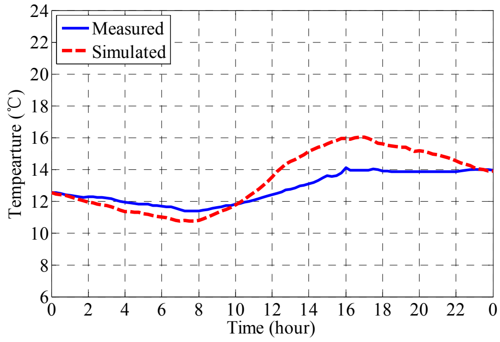

(c) Inward side of column 7 (Point B)

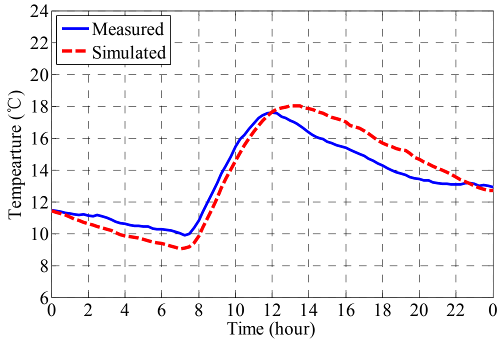

(d) Outward of column 7 (Point B)

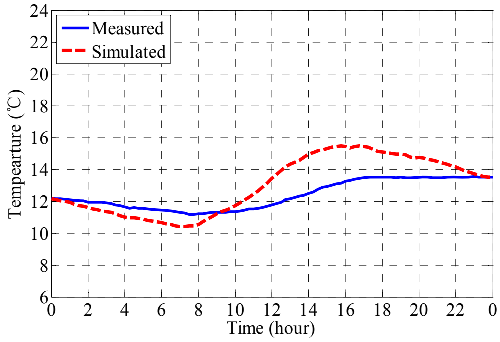

(e) Inward side of column 13 (Point C)

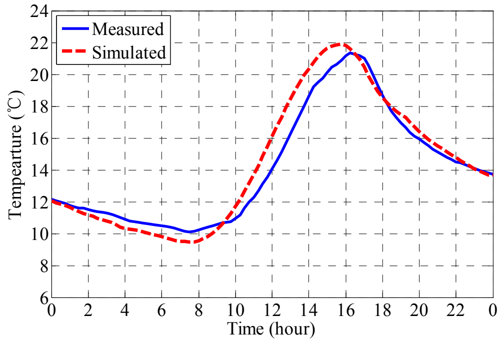

(f) Outward of column 13 (Point C)

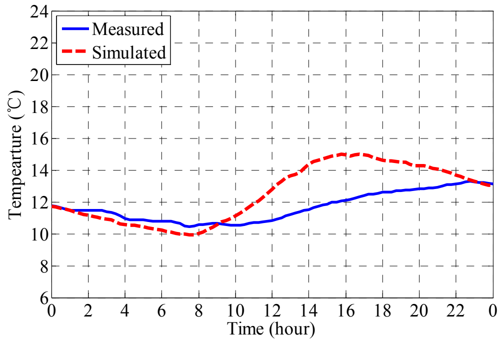

(g) Inward side of column 19 (Point D)

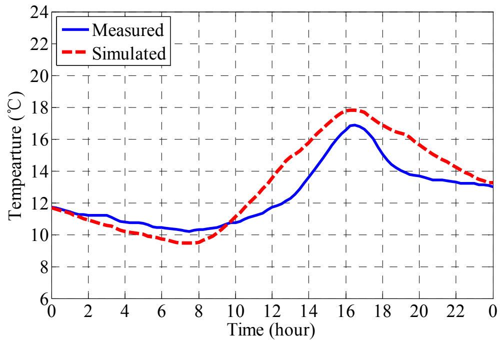

(h) Outward side of column 19 (Point D)

Figure 4-17. Measured and simulated temperature of the CFT column surfaces at cross-section 303.2m on 31st December 2013

4.2 Temperature Variation

Since the measurement point is limited, some structure members like ring and brace members are of no thermal sensors. The FE numerical simulated results can compensate for this shortage. The above comparison results show that the developed FE model is effective and satisfactorily to simulate the daily temperature distributions of the reinforced concrete inner tube and the CFT columns of the outer tube. The next step is to establish the proper temperature model that can be used as an input to the global structural analysis FE model to calculate the temperature-induced deformation and stresses. The deformation and stressed will also be compared with the field monitoring counterparts.

To obtain the daily adverse temperature distribution, one typical sunny day with high air temperature difference and low wind speed is chosen. Figure 4-18 (a) and (b) show the air temperature and wind speed on 31st December 2013. The air temperature on this day ranged from 7 °C to 20 °C and the maximum wind speed is 5 m/s.

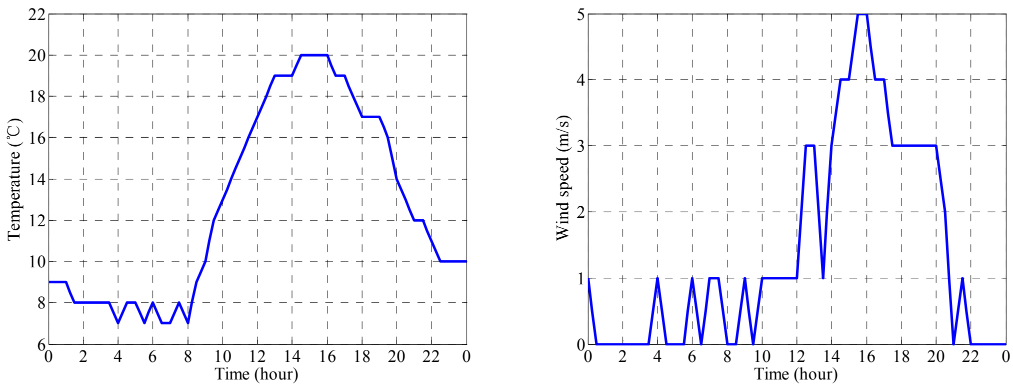

(a) Air temperature (b) Wind Speed

Figure 4-18. Air temperature and weed speed in Guangzhou on 31st December 2013

The daily relative temperature distribution of the inner tube and outer tube will be investigated in the following section. For brevity, the temperature at midnight (00:00) is set as the initial reference value. The temperature calculated at later instances is the change relative to the reference values.

4.2.1 Inner tube

For the inner tube covered by functional floors, it could not directly receive the solar radiation. The measured temperature variations in one day are less than 1°C, as shown in Figure 4-19. Therefore, the temperature of the inner tube covered with functional floors can be deemed as stable in one day.

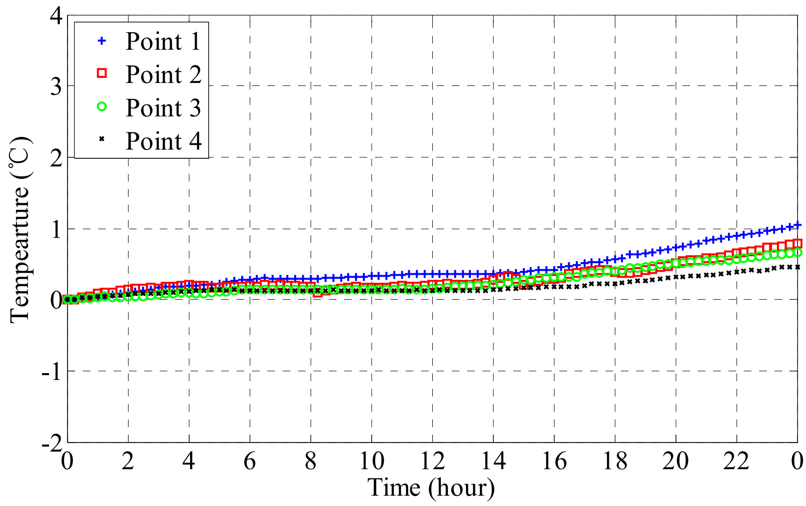

Figure 4-19. Measured temperature of the inner tube on the section 334.2 m on 31st December 2013

For the inner tube without function floors, most segments are exposed to the environment and receive partial solar radiation during the daytime. Figure 4-20 shows the simulated relative temperature variation of the four measurement points on section 303.2 m on 31st December 2013. The daily temperature variation is approximately from 2°C to 3°C, larger than that with function floor. The peak temperature occurred in the evening, lagging behind the air temperature. This is mainly because of the small thermal conductivity of the concrete.

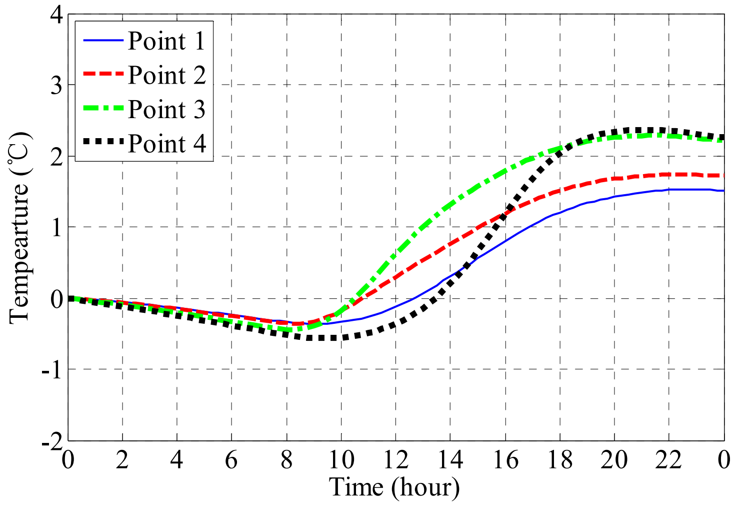

Figure 4-20. Simulated temperatures of the inner tube on section 303.2 m on 31st December 2013

4.2.2 Outer tube

The cross-section of the outer tube is circle. Their surfaces in different orientation receive different solar radiation, causing the temperature variation distribution of the section is very complicated. The equivalent temperature is thus proposed to represent the temperature of the entire structure member.

4.2.2.1 Column

As shown in Figure 4-21, the CFT column is divided into 3 regions. And the simulated temperature at the points shown in Figure 4-21 is used to calculate the equivalent temperature of the CFT column.

$$T_{R1} = (4*T_{CO} + T_{LC1} + T_{OC1} + T_{RC1} + T_{IC1})/8 \quad (4\text{-}1)$$

$$T_{R2} = (T_{LC1} + T_{OC1} + T_{RC1} + T_{IC1} + T_{LC2} + T_{OC2} + T_{RC2} + T_{IC2})/8 \quad (4\text{-}2)$$

$$T_{R3} = (T_{LS} + T_{OS} + T_{RS} + T_{IS} + T_{LC2} + T_{OC2} + T_{RC2} + T_{IC2}) / 8 \tag{4-3}$$

$$T_C = (T_{R1}S_{R1} + T_{R2}S_{R2} + T_{R3}S_{R3}) / S_C \tag{4-4}$$

where T_{CO}, T_{LC1}, T_{OC1}, T_{RC1}, T_{IC1}, T_{LC2}, T_{OC2}, T_{RC2}, T_{IC2}, T_{LS}, T_{OS}, T_{RS}, and T_{IS} are the simulated temperature at the points shown in Figure 5-14, S_{R1}, S_{R2} and S_{R3} are the area of the three divided region, S_C is the area of the entire column, T_C is the calculated the equivalent temperature of the CFT column.

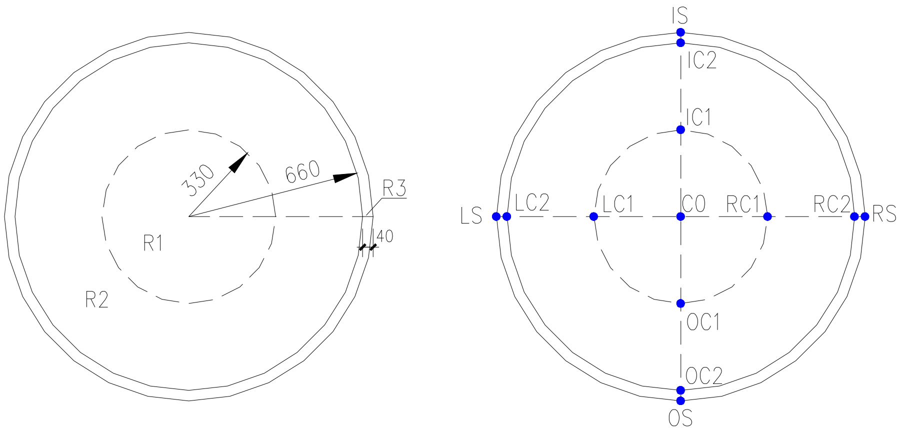

Figure 4-21. The region division of the CFT column for the outer tube

In Figure 4-21, “I” represents the facade towards the tower, “O” is outwards the tower, “L” is left and “R” is right. The simulated temperature of four CFT columns (Points A~D) on section 303.2 m is shown in Figure 4-22 to 4-25. It could be noticed that: (i) The interior and exterior surfaces of the steel tube have almost same temperature. This is because the steel has a very high heat conductivity. (ii) Different facades of the steel tube have much different temperature because they have different orientation to the sun and thus receive different solar radiation. However, the entire interior concrete has almost same temperature and the temperature variation is very small, because of low heat conductivity of the concrete. (iii) The maximum temperature variation of the CFT column surface is approximately 12 °C.

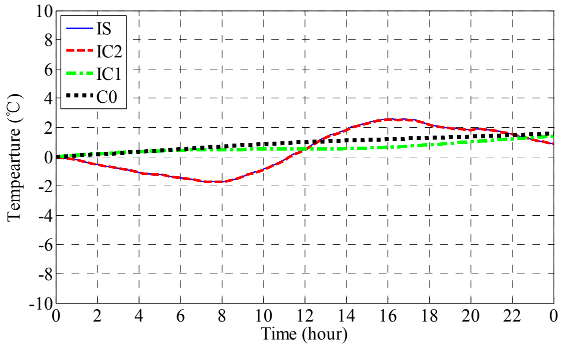

(a) Inner side

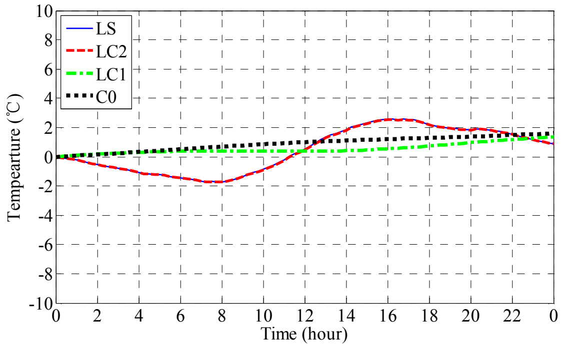

(b) Left side

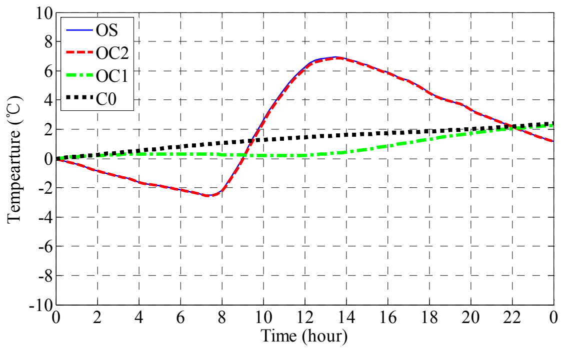

(c) Outer side

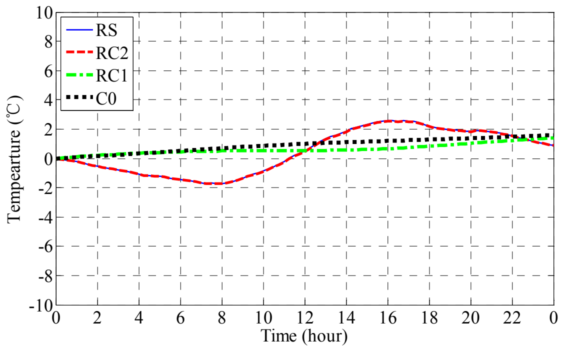

(d) Right side

Figure 4-22. Simulated temperatures of Point A on the CFT column of the outer tube on section 303.2m on 31st December 2013

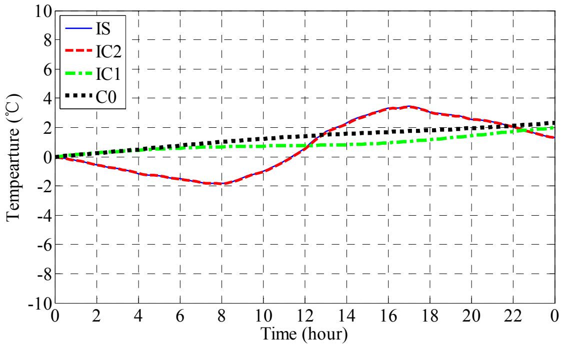

(a) Inner side

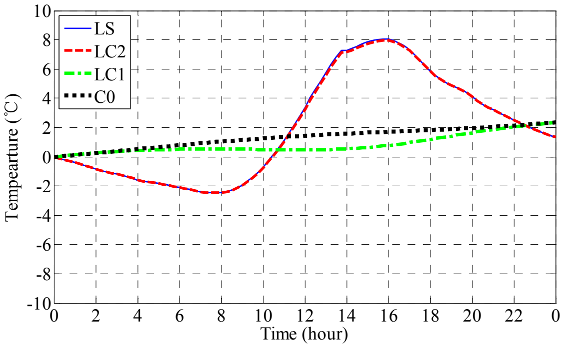

(b) Left side

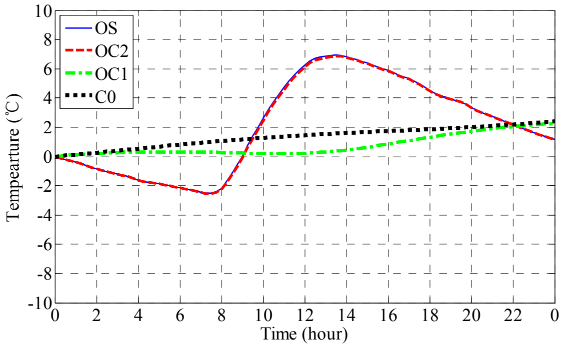

(c) Outer side

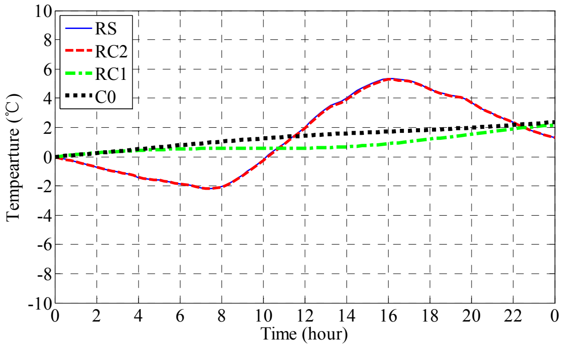

(d) Right side

Figure 4-23. Simulated temperatures of Point B on the CFT column of the outer tube on section 303.2m on 31st December 2013

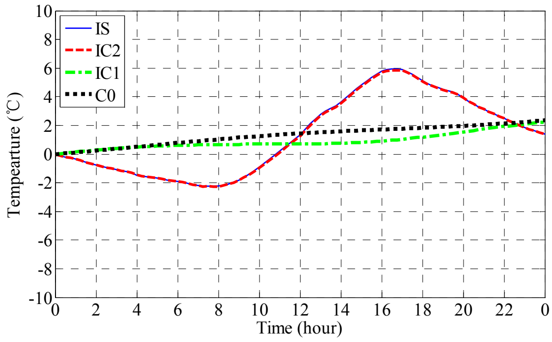

(a) Inner side

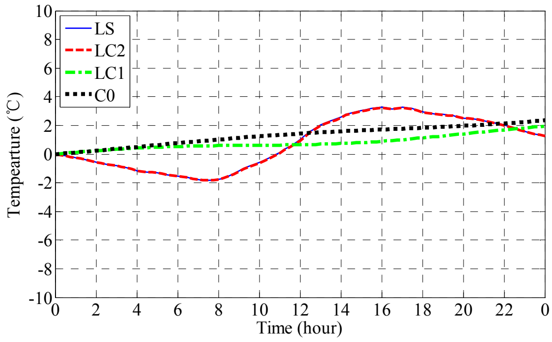

(b) Left side

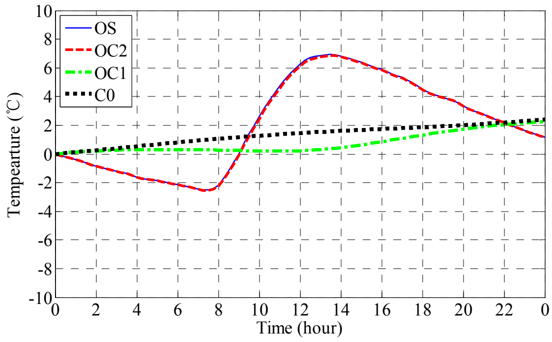

(c) Outer side

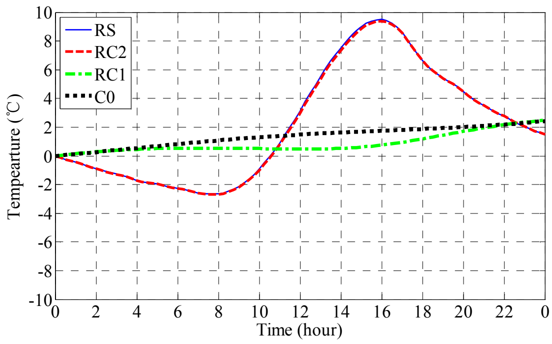

(d) Right side

Figure 4-24. Simulated temperatures of Point C on the CFT column of the outer tube on section 303.2m on 31st December 2013

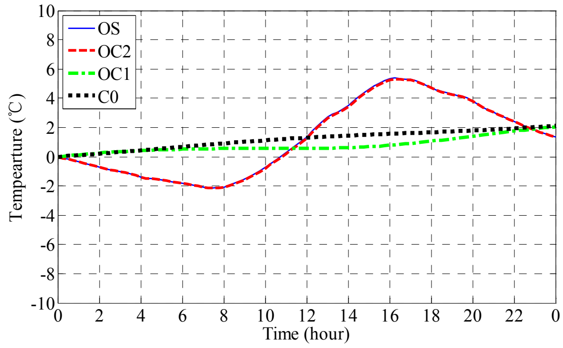

(a) Inner side

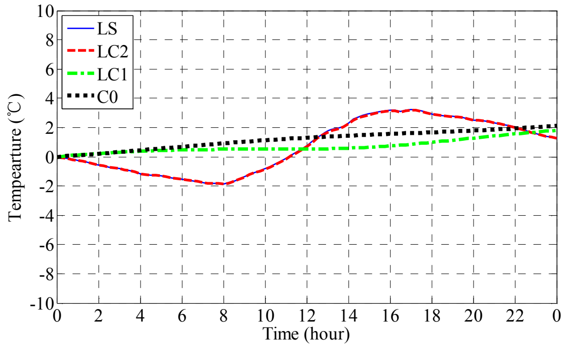

(b) Left side

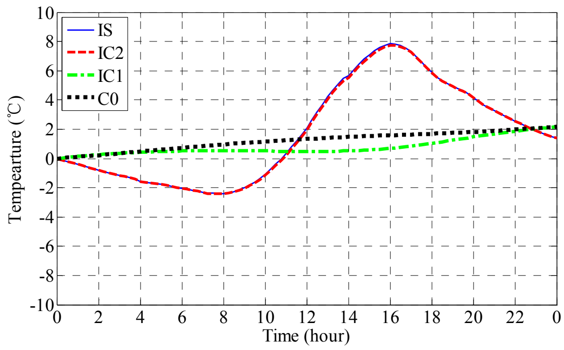

(c) Outer side

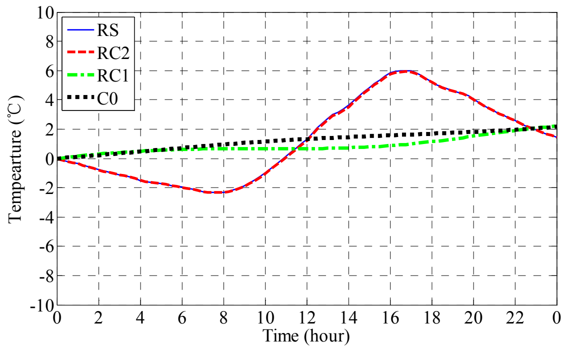

(d) Right side

Figure 4-25. Simulated temperatures of Point D on the CFT column of the outer tube on section 303.2m on 31st December 2013

The equivalent temperature of the four columns calculated from Eqs. (4-1) to (4-4) is shown in Figure 4-26. The temperature at Point B and C (the south) increased rapidly in the morning. After the sun moved to the west in the afternoon, the temperature at Point D started increasing. The temperature at above three points almost reached the maximum value at the same time in the afternoon (16:00). The maximum equivalent temperature difference between the points is approximately 3°C, occurred at 16:00 on 31st December 2013.

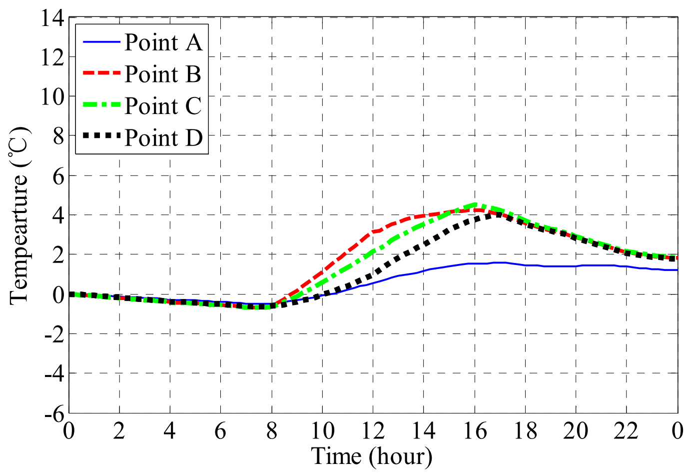

Figure 4-26. Simulated equivalent temperature of the CFT columns of the outer tube on 31st December 2013

4.2.2.2 Brace members

The brace and ring members of the outer tube are hollow steel pipe. Figure 4-27 shows such a section and four different orientations are considered, similar to the CFT columns. By averaging the simulated temperature of the 8 points, the equivalent temperature of the brace and ring members can be obtained and expressed as

$$T_{BR} = (T_{LS1} + T_{OS1} + T_{RS1} + T_{IS1} + T_{LS2} + T_{OS2} + T_{RS2} + T_{IS2})/8 \qquad (4\text{-}5)$$

where $T_{LC1}, T_{OC1}, T_{RC1}, T_{IC1}, T_{LC2}, T_{OC2}$, T_{RC2}, and T_{IC2} are the simulated temperature at the points.

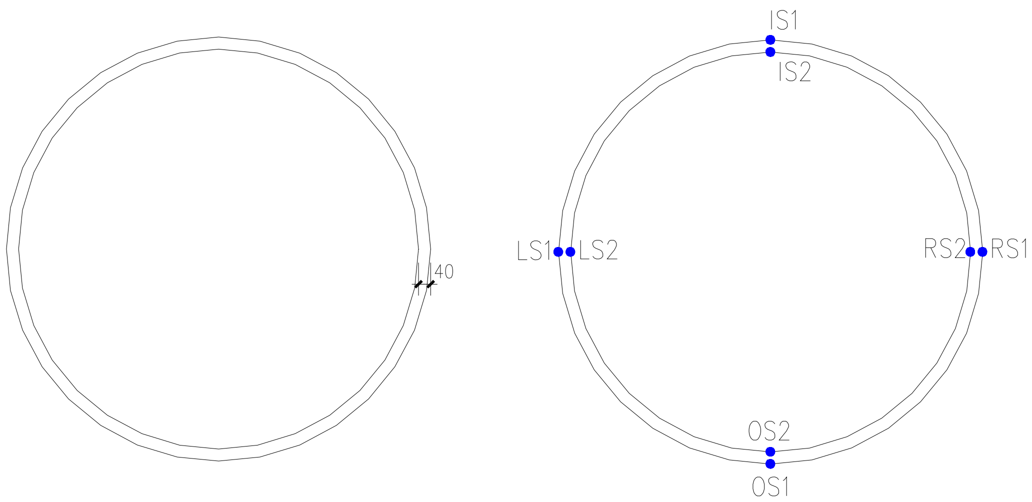

Figure 4-27. Section of the brace and ring members for the outer tube

The simulated temperature of the brace at Points A to D is shown in Figures 4-28 to 4-31. It could be noticed that: (i) Due to the high thermal conductivity of the steel, the temperature variations of the interior and exterior surfaces in the same side are almost the same. (ii) The maximum temperature of the steel surface occur at different time due to their relative position to the sun. (iii) The maximum temperature variation of the brace surface is approximately 16 °C, occurring at outward side of Points B and C. The daily variation is larger than the counterpart of the CFT column.

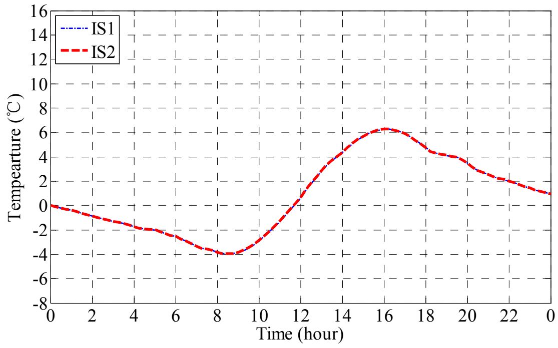

(a) Inward side

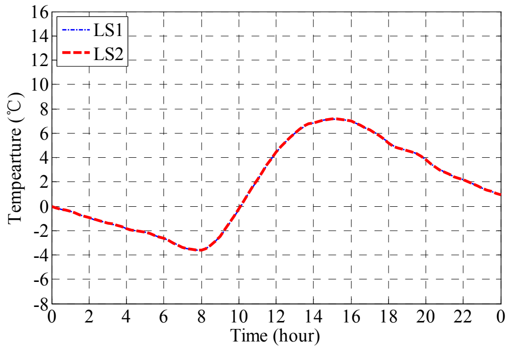

(b) Left side

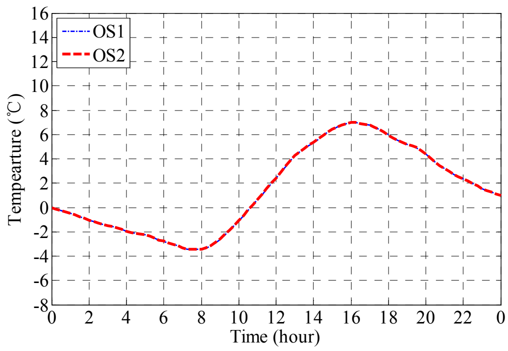

(c) Outward side

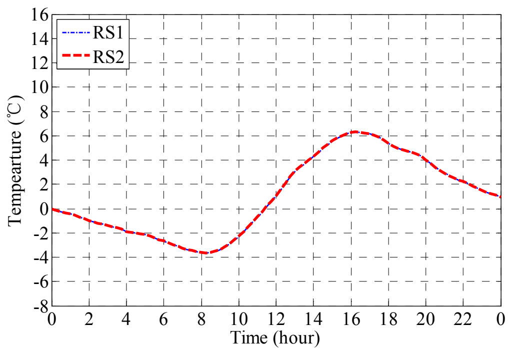

(d) Right side

Figure 4-28. Simulated temperature of the brace of the outer tube (Point A) on section 303.2 m on 31st December 2013

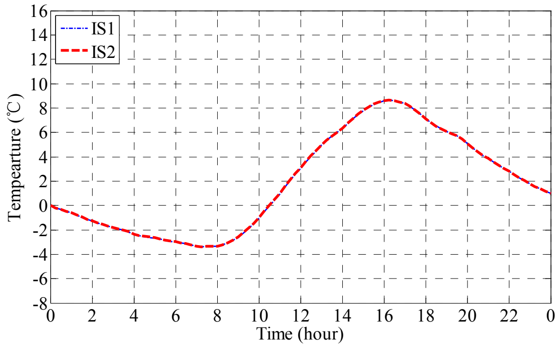

(a) Inner side

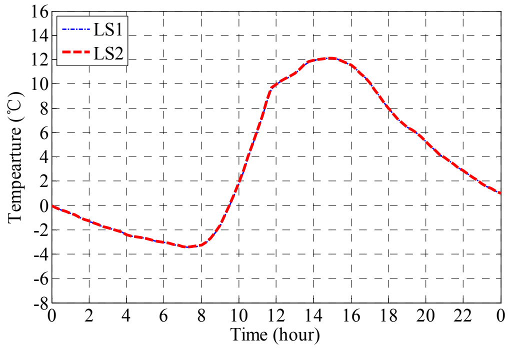

(b) Left side

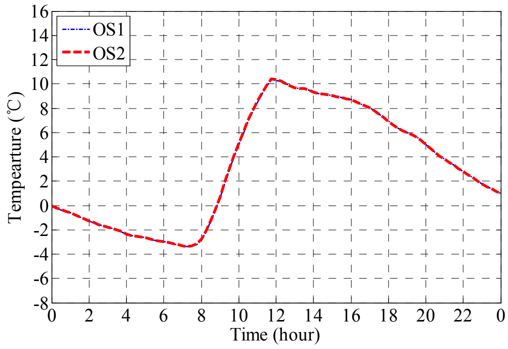

(c) Outer side

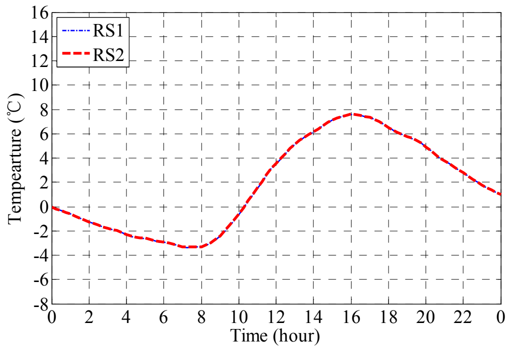

(d) Right side

Figure 4-29. Simulated temperature of the brace of the outer tube (Point B) on section 303.2 m on 31st December 2013

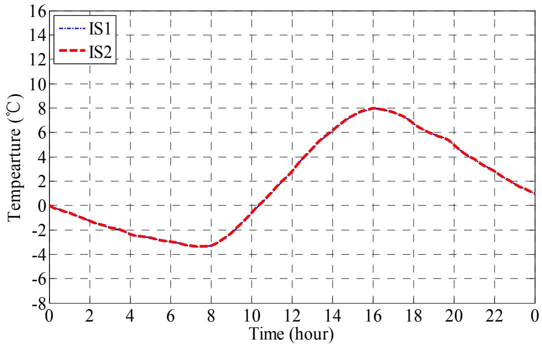

(a) Inner side

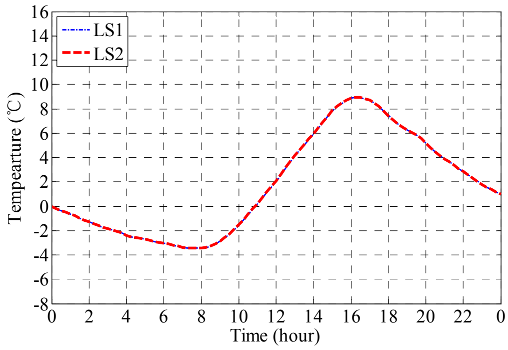

(b) Left side

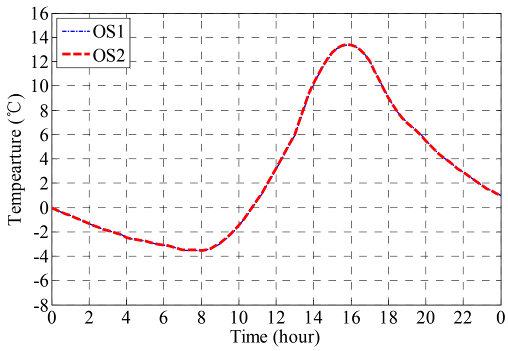

(c) Outer side

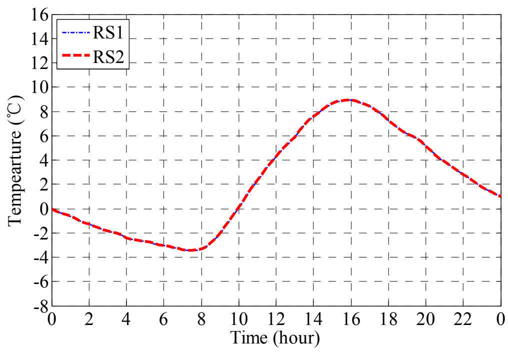

(d) Right side

Figure 4-30. Simulated temperature of the brace of the outer tube (Point C) on section 303.2 m on 31st December 2013

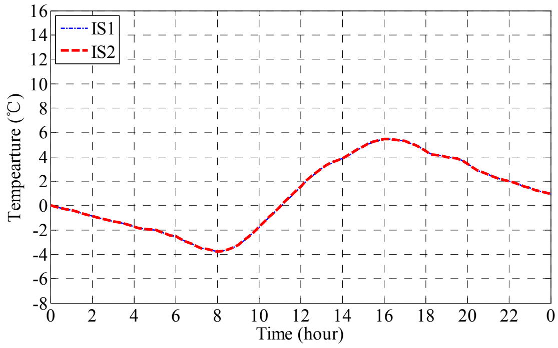

(a) Inner side

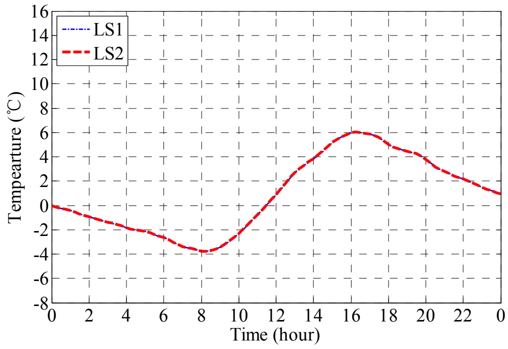

(b) Left side

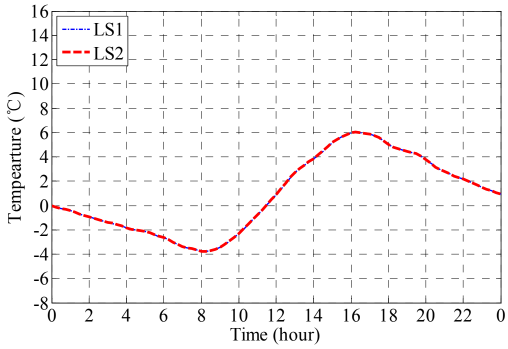

(c) Outer side

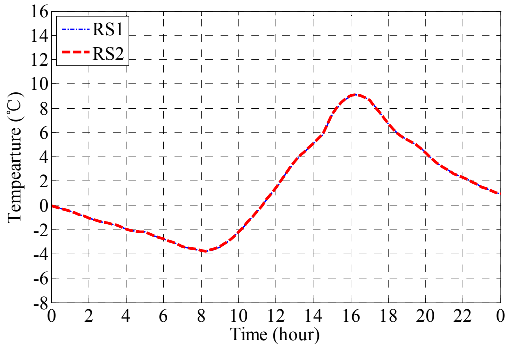

(d) Right side

Figure 4-31. Simulated temperature of the brace of the outer tube (Point D) on section 303.2 m on 31st December 2013

The equivalent temperature of the brace member is calculated from Eq. 4-5 and shown in Figure 4-32. The temperature at Point B in the southeast façade increased rapidly in the morning. The temperatures of the four points almost reached the maximum value at the same time in the afternoon. The variation of the daily equivalent temperature of the points is approximately 13°C and the maximum temperature difference between different facades of the brace members is approximately 5°C, occurring Points B and D at 12:00 on 31st December 2013.

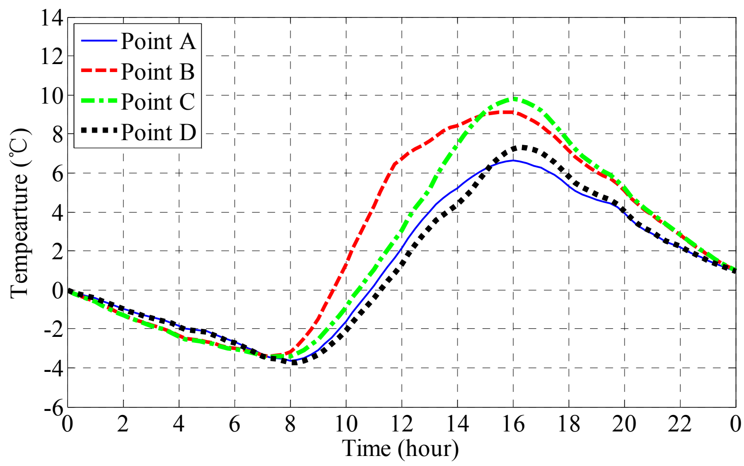

Figure 4-32. Simulated equivalent temperature of the brace member of the outer tube on section 303.2 m on 31st December 2013

<u>*4.2.2.3 Ring members*</u>

The simulated temperatures of the ring at Points A to D are shown in Figure 4-33 to Figure 4-36. It could be noticed that: (i) Due to the high thermal conductivity of the steel, the temperature variations of the interior and exterior surfaces in the same side are almost the same. (ii) The maximum temperatures of the steel surface occur at different time due to their relative position to the sun. (iii) The maximum temperature variation of the ring surface is approximately 17 °C, occurring at the outward side of Point C. The daily variation is larger than the counterpart of the CFT column and similar to the brace.

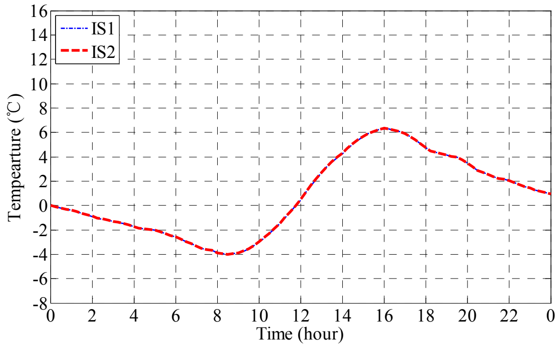

(a) Inner side

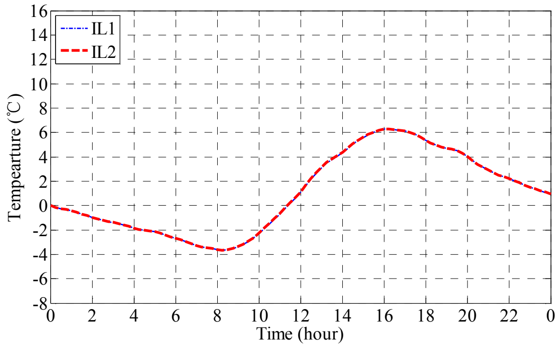

(b) Left side

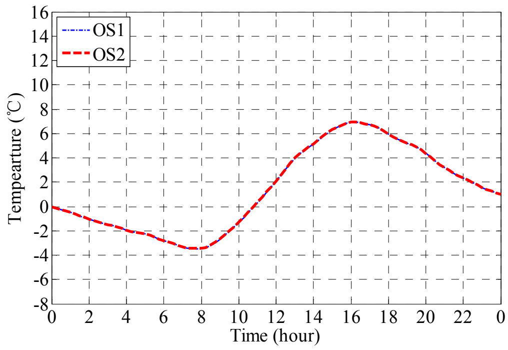

(c) Outer side

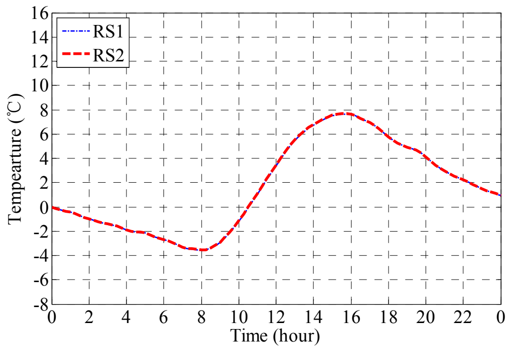

(d) Right side

Figure 4-33. Simulated temperature of the ring of the outer tube (Point A) on section 303.2m on 31st December 2013

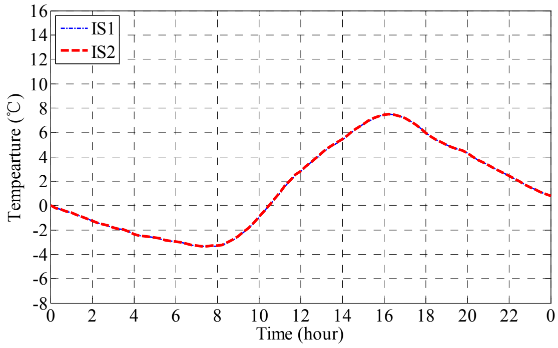

(a) Inner side

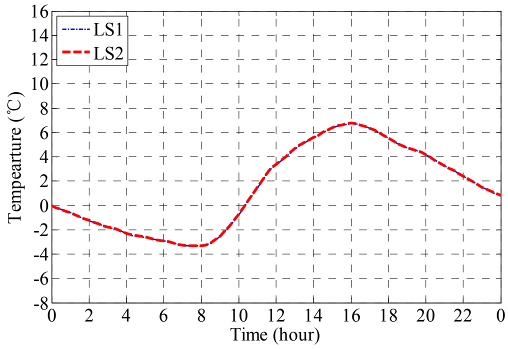

(b) Left side

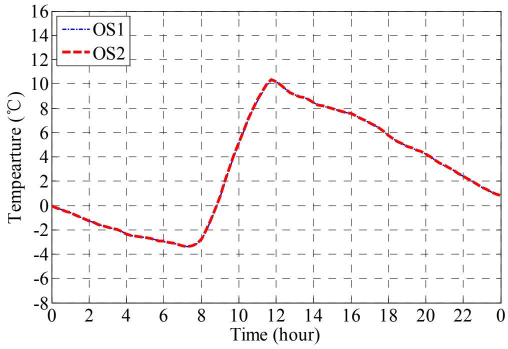

(c) Outer side

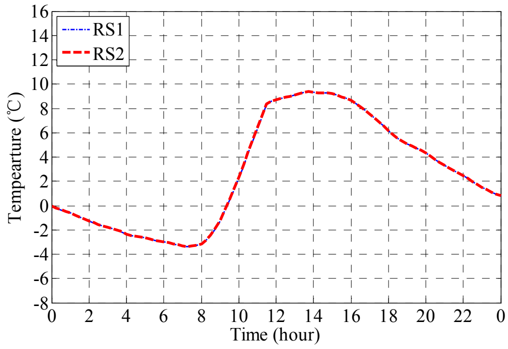

(d) Right side

Figure 4-34. Simulated temperature of the ring of the outer tube (Point B) on section 303.2m on 31st December 2013

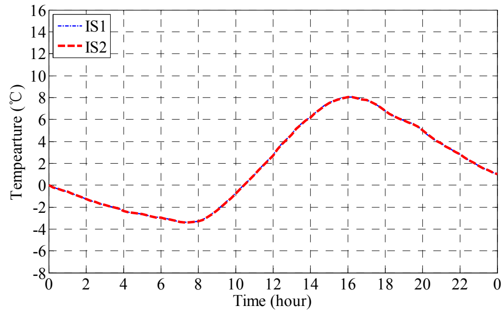

(a) Inner side

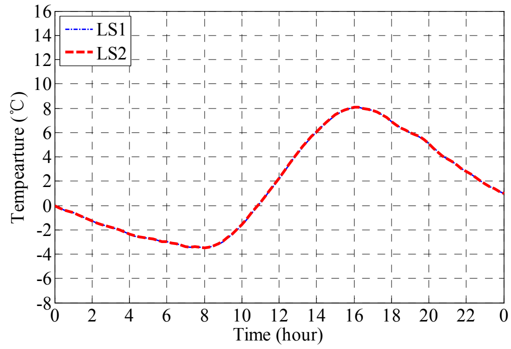

(b) Left side

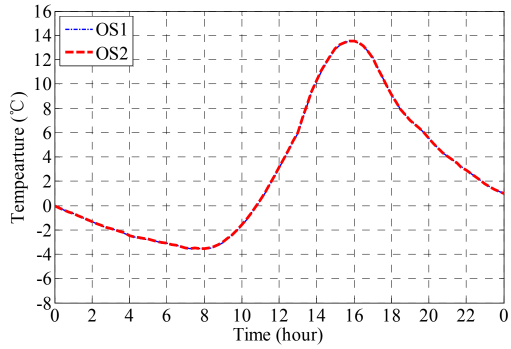

(c) Outer side

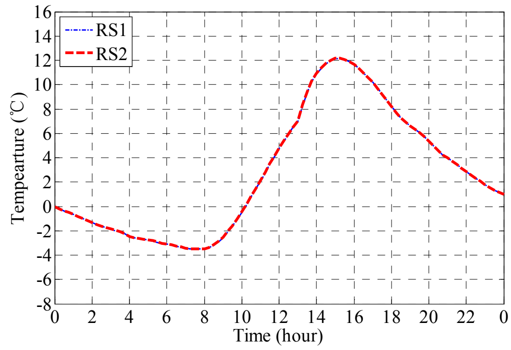

(d) Right side

Figure 4-35. Simulated temperature of the ring of the outer tube (Point C) on section 303.2m on 31st December 2013

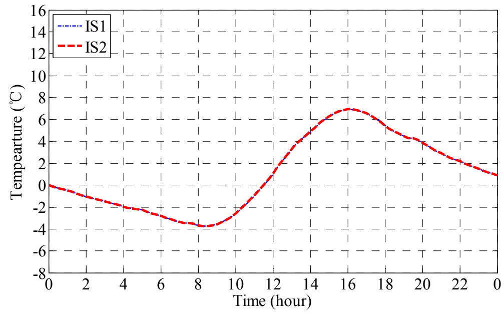

(a) Inner side

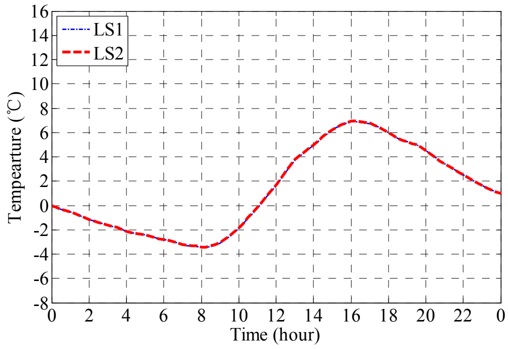

(b) Left side

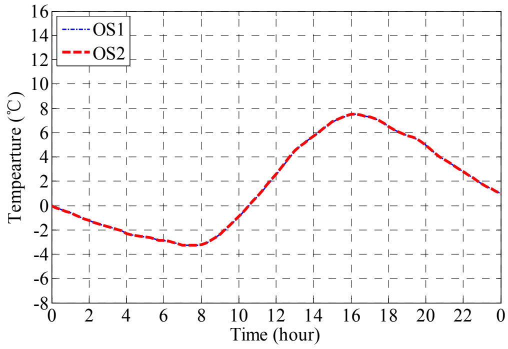

(c) Outer side

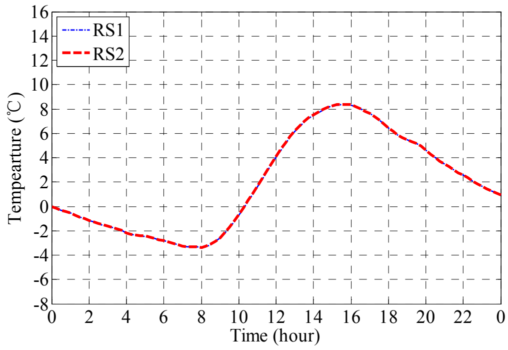

(d) Right side

Figure 4-36. Simulated temperature of the ring of the outer tube (Point D) on section 303.2m on 31st December 2013

The equivalent temperature of the ring member is calculated from Eq. 4-5 and shown in Figure 4-37. The temperature at Point B (in the southeast) increased rapidly in the morning. The temperatures of the four points almost reached the maximum value at the same time in the afternoon. The maximum variation of the daily equivalent temperature is approximately 13°C. The maximum temperature difference between Points B and A at the ring members is approximately 4°C, occurring at 12:00 on 31st December 2013. The maximum temperature difference between Point C and A at the brace members is approximately 4°C, occurring at 16:00 on 31st December 2013

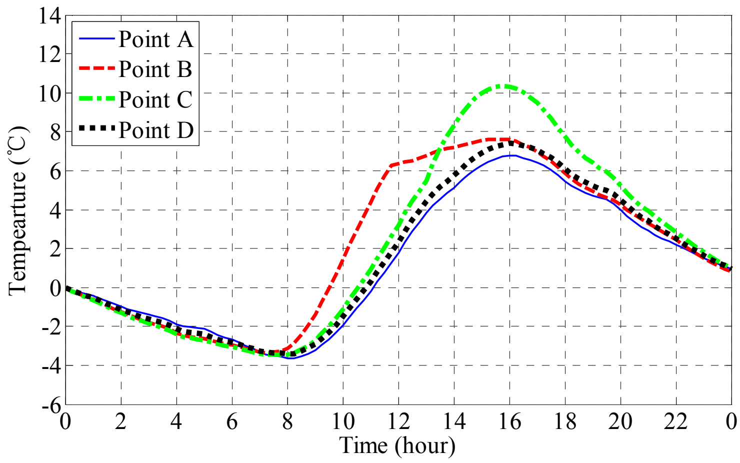

Figure 4-37. Simulated equivalent temperature of the ring member of the outer tube on section 303.2m on 31st December 2013

4.3 Temperature Variation Distribution

The daily temperature-induced movement of the Tower top is normally due to the temperature difference between different sides of the structure, especially the outer tube. It can be noticed that from the results in the last section, the maximum temperature difference between different sides on 31st December 2013 occurred at 12:00 or 16:00. The relative temperature difference between different members of the outer tube at 12:00 and 16:00 are shown in Figures 4-38 and 4-39, respectively.

The temperature of Points A to D is determined from the simulated results. The temperature of the other members of the outer tube is determined by a linear interpolation of the temperature values at the simulated points. The simulated daily relative temperature distribution of the inner tube at 12:00 and 16:00 is obtained in the similar way, as shown in Figures 4-40(a) and (b), respectively. These values are then input into the global structural FE model to calculate the temperature-induced structural responses.

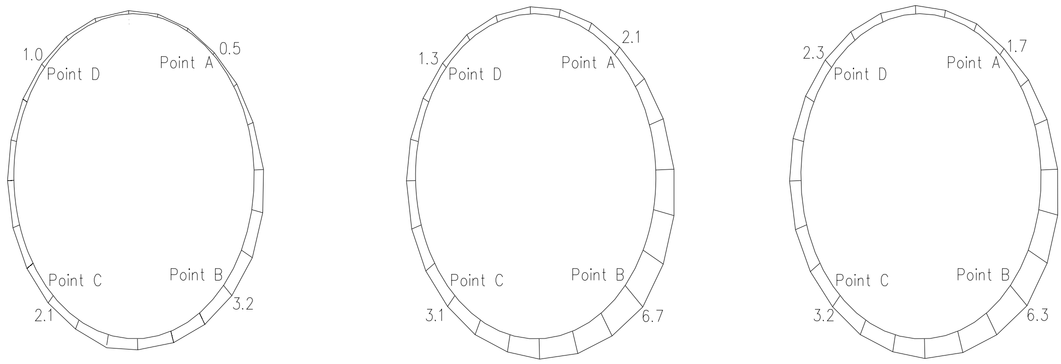

(a) column (b) brace (c) ring

Figure 4-38. Simulated equivalent relative temperature distribution of the structure members of the outer tube at 12:00 on 31st December 2013

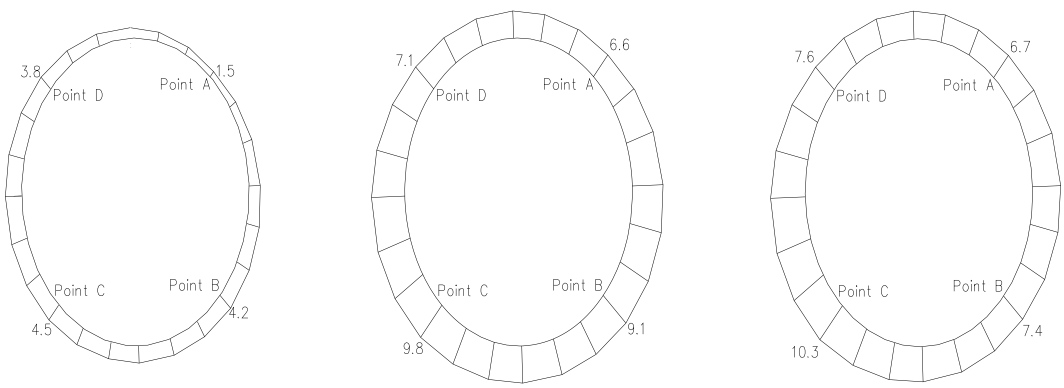

(a) column (b) brace (c) ring

Figure 4-39. Simulated equivalent relative temperature distribution of the structure members of the outer tube at 16:00 on 31st December 2013

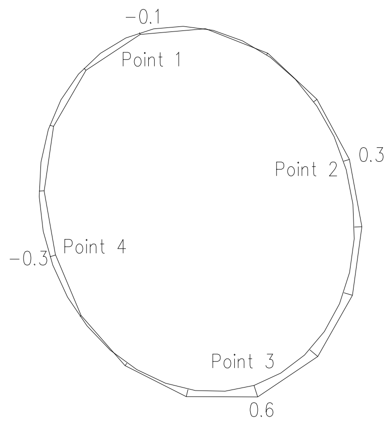

(a) 12:00

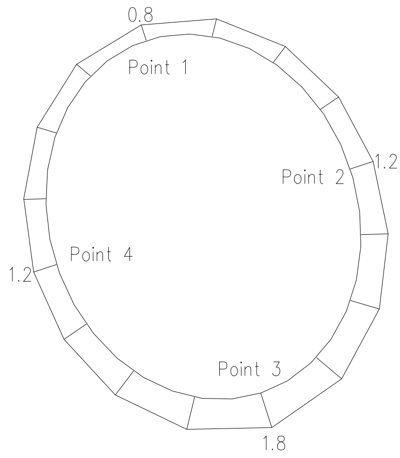

(b) 16:00

Figure 4-40. Simulated equivalent relative temperature distribution of the inner tube on 31st December 2013

Similarly, the relative temperature distributions in other seasons are obtained. Figures 4-41 and 4-42 show the results of the outer tube at 11:30 and 16:30 on 14th April 2013, respectively. At these two instances, the temperature distribution is the most unfavorable. The relative temperature distribution of the inner tube at 11:30 and 16:30 is shown in Figures 4-43(a) and (b), respectively. These values are then input the global structural FE model to calculate the temperature-induced structural responses.

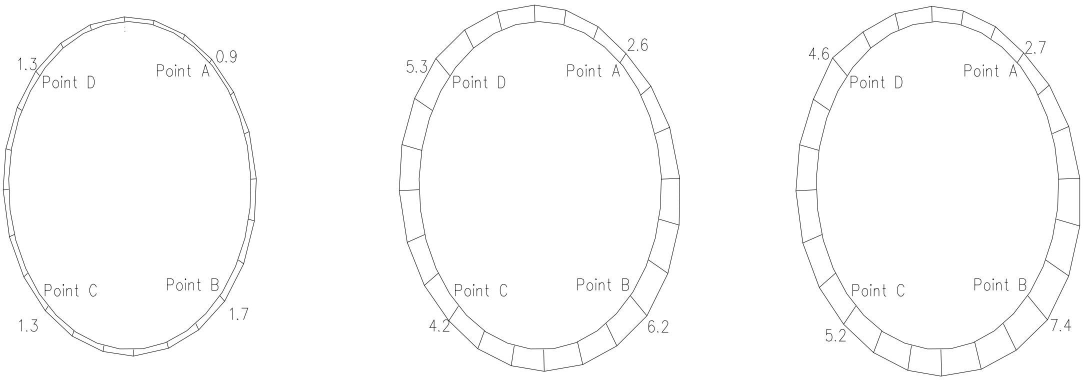

(a) column (b) brace (c) ring

Figure 4-41. Simulated equivalent relative temperature distribution of the structure members of the outer tube at 11:30 on 14th April 2013

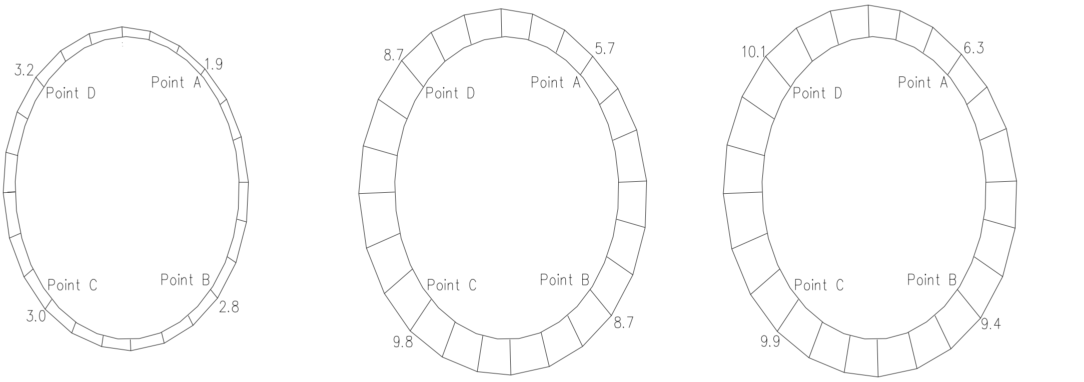

(a) column (b) brace (c) ring

Figure 4-42. Simulated equivalent relative temperature distribution of the structure members of the outer tube at 16:30 on 14th April 2013

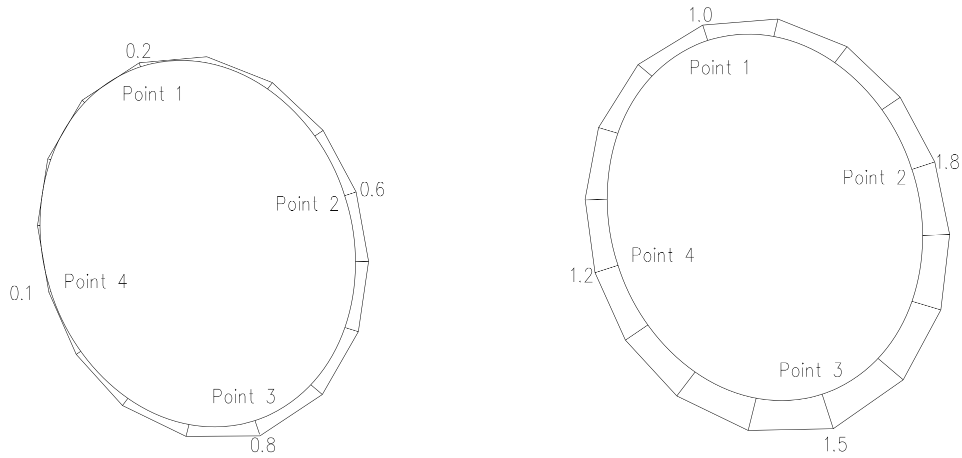

Figure 4-43. Simulated equivalent relative temperature distribution of the inner tube on 14th April 2013

4.4 Calculated Temperature-induced Deformation

4.4.1 FE Model of Canton Tower

Using the commercial software SAP2000, a 3D global FE model of the Canton Tower has been established. It has been validated by comparing the modal properties with the measured ones (Ni et al. 2009). Figure 4-44 illustrates the FE model in SAP2000, which will be used to calculate the temperature-induced deformation of the tower top in typical sunny day. In this model, two-node beam elements with six degrees of freedom at each node are used to model the outer tubes and the connecting beams between the inner and outer structures; four-node and three-node shell elements with six degrees of freedom at each node are used to model the shear-walls of the inner structure and the floor slabs. This model is composed of 21,902 beam elements and 22,768 shell elements, and 27,534 nodes.

By inputting the temperature distributions shown in Figure 4-38 to 4-43 into the established finite element model, the temperature-induced deformations (displacements) of the tower are calculated, which will be further compared with the displacement measurement results obtained by a GPS system. For simplicity, the temperature of each structural member is assumed as uniform and taken one identical value. With the obtained temperature increments for all members at each time instance, the corresponding deformations of the tower are attributed to temperature effect.

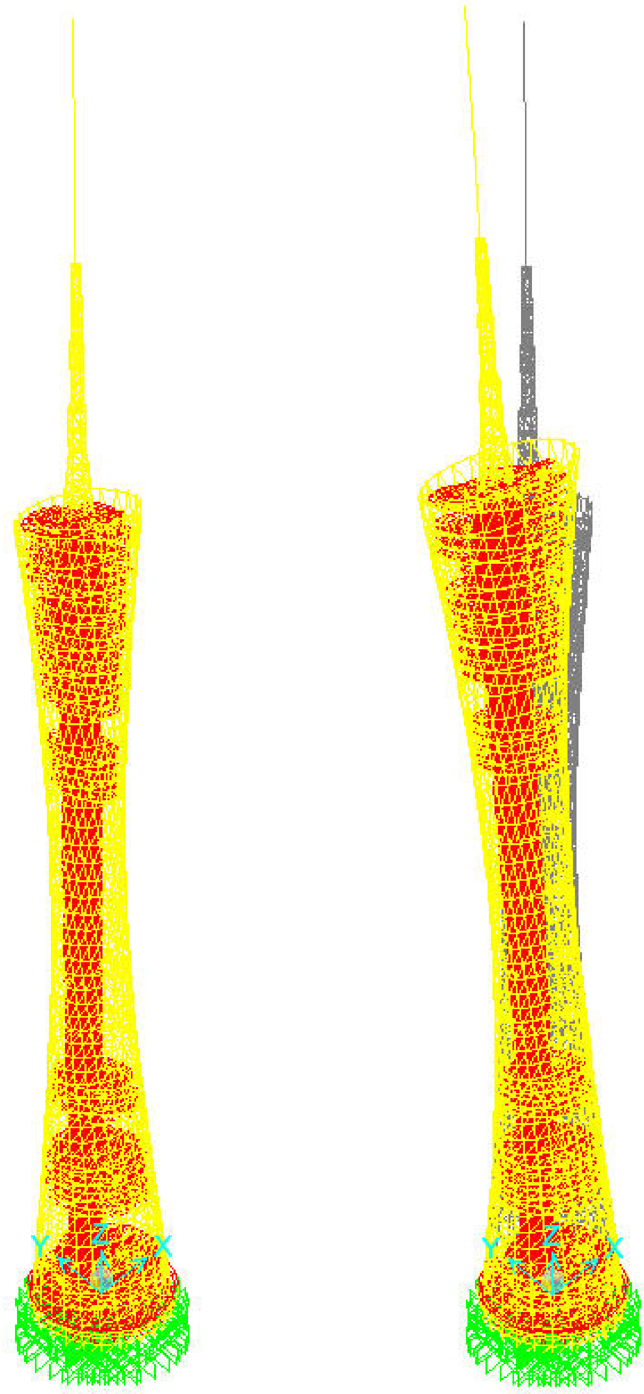

(a) initial configuration (b) deformed configuration

Figure 4-44. Finite element model of Canton Tower

4.4.2 Temperature-induced Horizontal Displacements

A GPS system has been installed and operated during the construction period. The sampling rate of the system is 1 Hz (one data per second). One GPS rover is located at the top of the inner structure, and the reference station is located at the sightseeing platform.

Figure 4-45 shows the daily movement track at an interval of 0.5 hour on 31st December 2013. The positions are averaged over the data every half-hour period. The track starts at 00:00 from the origin, which is taken as the reference point.

The members of the tower that are exposed to the sun received direct solar radiation. Thus, these members had higher temperature than those on the shaded facade, causing the structure to bend away from the sun. During early morning (before 7:00), the movement of the tower top was small and slow. After sunrise, the tower started to move toward west and arrived to its westernmost position at approximately 12:00. When the sun moved to the west in the afternoon, the temperature of the members in the southwest increased, causing the tower to move northeast. At 16:00, the tower reached its northernmost position. Afterward, the temperature difference among the tower members decreased, causing the tower to move back gradually from the north to south. The tower movement is about 14 cm in both east-west and north-south directions. The moments when the tower reached the westernmost and northernmost position are consistent with the moments when the adverse temperature distribution occurred.

With the FE model, the calculated tower top displacements at 12:00 and 16:00 are also shown in Figure 4-45. Comparison between the calculation and measurement is listed in Table 4-2 and shown in Figure 4-45. The two results agree very well, indicating the temperature distribution obtained from the thermal analysis is accurate and effective in calculating the temperature-induced displacements of the Canton Tower.

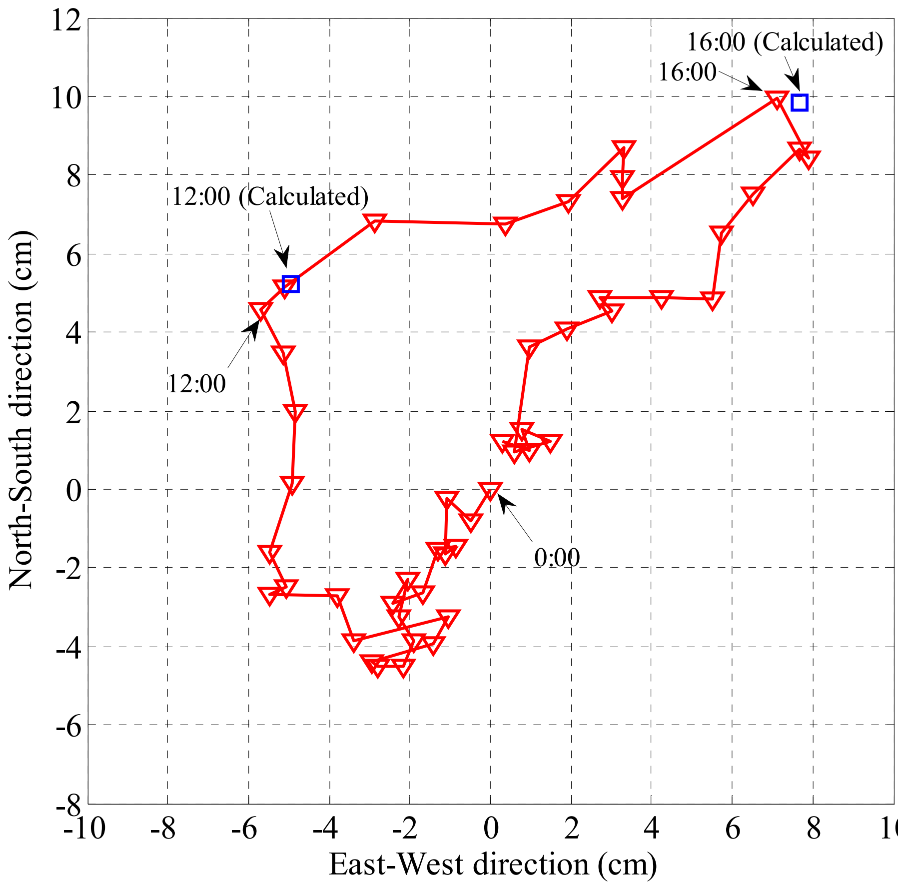

Figure 4-45. Displacement track of the tower top on 31st December 2013

Table 4-2. Comparison of GPS-measured and calculated displacements at tower top on 31st December 2013

Time	Direction	Displacement (cm)	
		GPS-measured	Calculated
12:00	North	4.56	5.23
	East	-5.69	-4.97
16:00	North	9.96	9.83
	East	7.11	7.69

Form the FE model, the deformation mode, or deformation profile of the entire structure along the height can be obtained. Figure 4-46 plot the displacement profile of the Tower at 12:00 on 31st December 2013, when the Tower had the maximum horizontal east-west displacement (see Figure 4-45). Figure 4-47 plot the displacement profile of the Tower at 16:00 on 31st December 2013, when the Tower had the maximum horizontal north-south displacement (see Figure 4-45). Point 1 to Point 4 in the above two figures represent the corresponding positions shown in Figure 4-7 at different heights. The deformation in the two figures showed the bending mode of the entire structure, different from the bending-shear mode of a typical frame−wall structure. This is because the floors of the Canton Tower are not attached to the outer tube and the floor girders are connected to the outer frame columns through bolts. Such a joint design causes the CFT columns can rotate freely to release the bending moment of the joints. Consequently the outer frame tube has less restraint on the deformation of the inner tube.

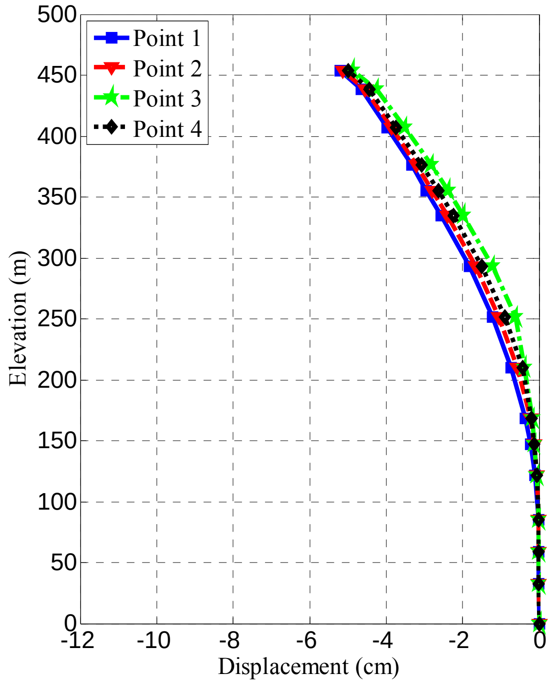

Figure 4-46. Displacement profile of the tower along the height in east-west direction at 12:00 on 31st December 2013

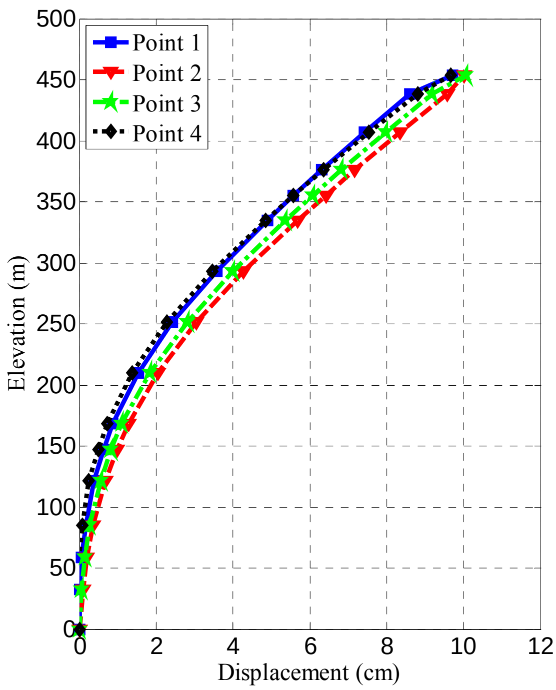

Figure 4-47. Displacement profile of the tower along the height in south-north direction at 16:00 on 31st December 2013

Figure 4-48 shows the daily movement track at the tower top on 14th April 2013. Again, the position of the tower at 00:00 is taken as the reference point and later position is the displacement relative to the reference. Similar to the tower movement in winter, the movement of the tower was small and slow during early morning (before 7:00). After sunrise, the tower started to move toward west and arrived to its westernmost position at approximately 11:30. In the afternoon, the tower moved to towards northeast. At 16:30, the tower reached its northernmost position. Afterward, the temperature difference among the tower members decreased, causing the tower to move back gradually from the north to the south. The tower displacement in one day is about 16cm in the east-west direction and 8 cm in the south-north.

The east-west displacement on 14th April 2013 is similar to that on 31st December 2013, whereas the south-north displacement on 14th April 2013 is much smaller than that on 31st December 2013. This is because the sun moves to the south in winter, causing the daily temperature difference between the south and north counterparts of the Canton Tower is more significant than other seasons. Consequently the daily movement in the south-north direction is relatively large.

Again the calculated tower top displacements at 11:30 and 16:30 are also shown in Figure 4-48. The comparison between the calculation and measurement results is present in Table 4-3 and Figure 4-48. The two sets of data agree very well.

Figure 4-49 plot the displacement profile of the Tower at 16:30 on 14th April 2013, when the Tower had the maximum horizontal east-west displacement (see Figure 4-48). Figure 4-50 plot the displacement profile of the Tower at 16:30 on 14th April 2013, when the Tower had the maximum horizontal north-south displacement (see Figure 4-48). The deformation in the two figures also showed the bending mode of the entire structure, same as the results on 31st December 2013.

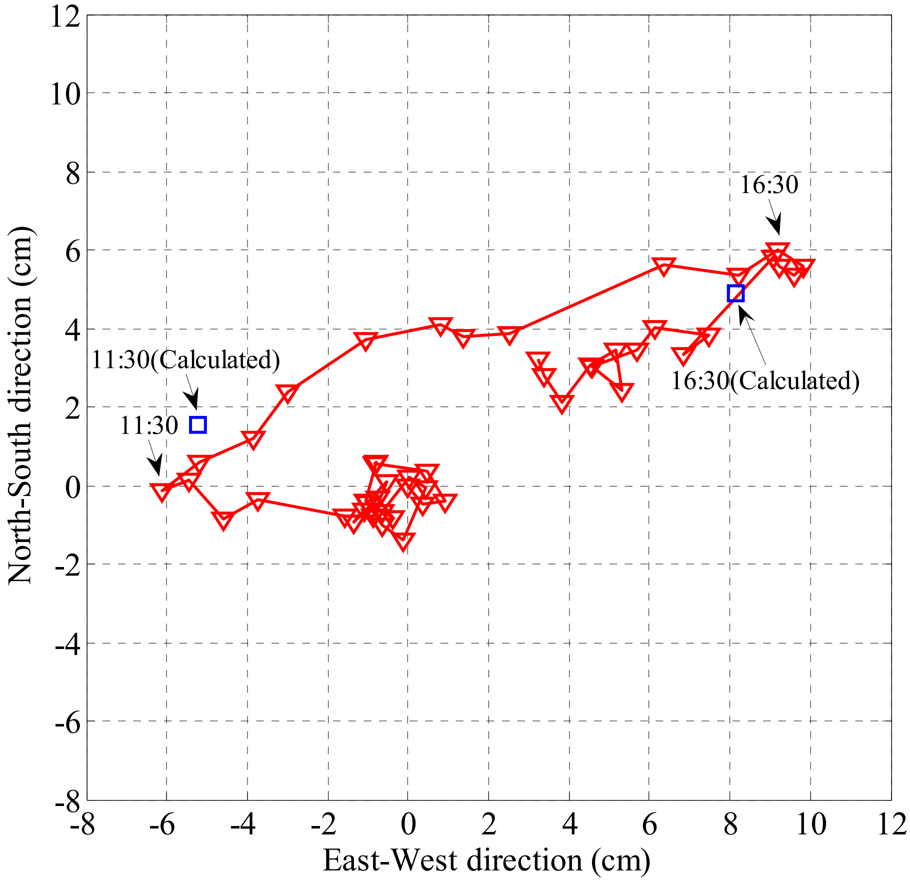

Figure 4-48. GPS-measured displacement track of the tower top on 14th April 2013

Table 4-3. Comparison of GPS-measured and calculated displacements at tower top on 14th April 2013

Time	Direction	Displacement (cm)	
		GPS-measured	Calculated
11:30	North	0.14	1.56
	East	-6.13	-5.23
16:30	North	6.00	4.89
	East	9.20	8.13

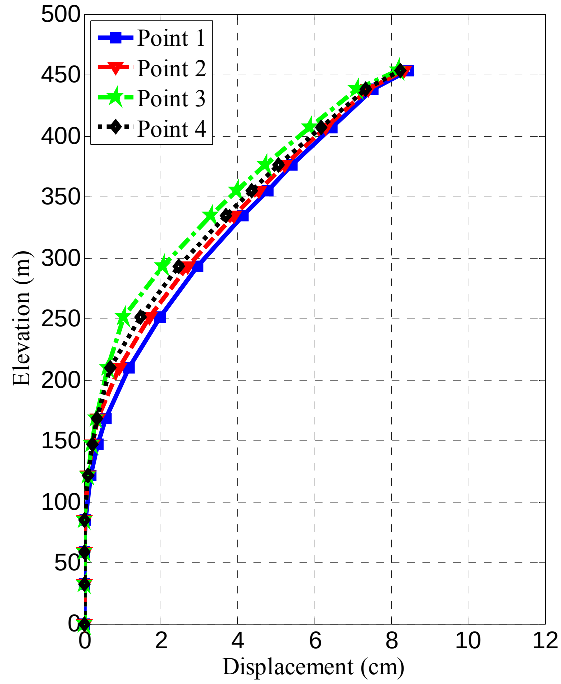

Figure 4-49. Displacement profile of the tower along the height in east-west direction at 16:30 on 14th April 2013

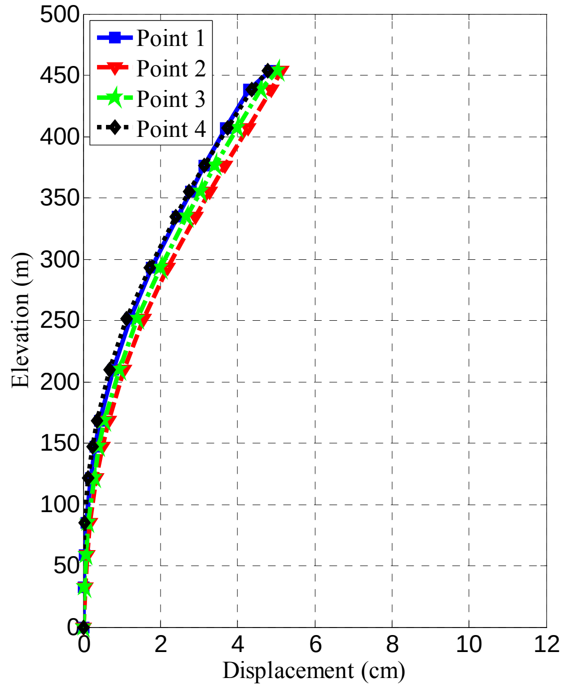

Figure 4-50. Displacement profile of the tower along the height in south-north direction at 16:30 on 14th April 2013

CHAPTER FIVE

DEFORMATION MONITORING OF CANTON TOWER USING REAL-TIME STRAIN DATA

5.1 Introduction

Lateral displacement is a critical parameter for assessing the safety and serviceability of supertall buildings. In contrast to acceleration measurement, accurately measuring displacement in practice can be challenging. Although displacement can be calculated from the double integral of acceleration, the displacement may drift over time because of the static and low-frequency components of the measured acceleration data (Chan et al. 2006).

Recently developed advanced techniques have allowed the displacement measurement of large-scale structures. These techniques include the utilization GPS, total station, radar, laser, and video camera. Except for GPS, these land-surveying techniques are often used for short-term monitoring rather than continuous long-term monitoring because such tools rely on good weather conditions and manpower. By contrast, GPS can automatically measure both static and dynamic deformations for a long period regardless of visibility or weather. Therefore, GPS is widely applied in measuring the deformations of civil structures, such as long-span bridges (Roberts et al. 2002, Breuer et al. 2008, Kijewski-Correa et al. 2007, Xia et al. 2013), high-rise buildings (Tamura et al. 2004, Meng et al. 2007, Xu et al. 2010, Park et al. 2008), and dams (He et al. 2005). A number of studies integrated the GPS with other conventional instruments, such as accelerometers (Cazzaniga et al. 2005, Li et al. 2006, Smyth et al. 2007), robotic total stations (Psimoulis et al. 2008), and inclination sensors (Yigit et al. 2008) to enhance the accuracy of measurement. Nevertheless, GPS accuracy in practice is still not very high. The quality of GPS measurement can be affected by various factors, such as satellite visibility, availability and geometry, quality of signal sent, delays caused by GPS waves crossing the ionosphere and troposphere, and multipath (Yi et al. 2013).

This chapter presents a new method for calculating the deformation of super-tall structures based on the assumption that the entire structure can be regarded as a cantilever beam. Thus, the deformation of the beam can be associated with the strain along the beam. Consequently, the displacement and tilt can be calculated from the strain using the virtual work theory. The effectiveness of the technique is verified through its application to the Canton Tower. The calculated displacements and tilts under different environmental conditions are compared with those measured using GPS and inclinometer. In addition, the displacement profile of the structure along the height can be obtained as well, which is not available using other measuring approaches.

5.2 Derivation of deformation using the distributed strain data

For slender and flexible super-tall structures that stand hundreds of meters, the tube can be regarded as a cantilever beam. The deformation of the cantilever beam can be represented by the longitudinal strain at different sections. As illustrated in Figure 5-1(a), a deformed cantilever beam is divided into *n* segments according to the available strain measurement points. The length of the *i*-th segment is h_i. At point *i*, the strain difference across the section is $\Delta\varepsilon_i$. If the strain difference between the measurement points is assumed to vary linearly, then the strain difference distribution along the entire beam can be shown as Figure 5-1(b). Figure 5-1(c) shows the deformation of an infinitesimal element of length *dh*. The angular rotation of the infinitesimal element can be expressed as follows:

$$d\theta = \frac{(\varepsilon_l - \varepsilon_r)dh}{b} = \frac{\Delta\varepsilon dh}{b} \tag{5-1}$$

where ε_l and ε_r are the vertical strain at the left and right surfaces of the element, respectively, $\Delta\varepsilon$ is their difference, and *b* is the height of the section.

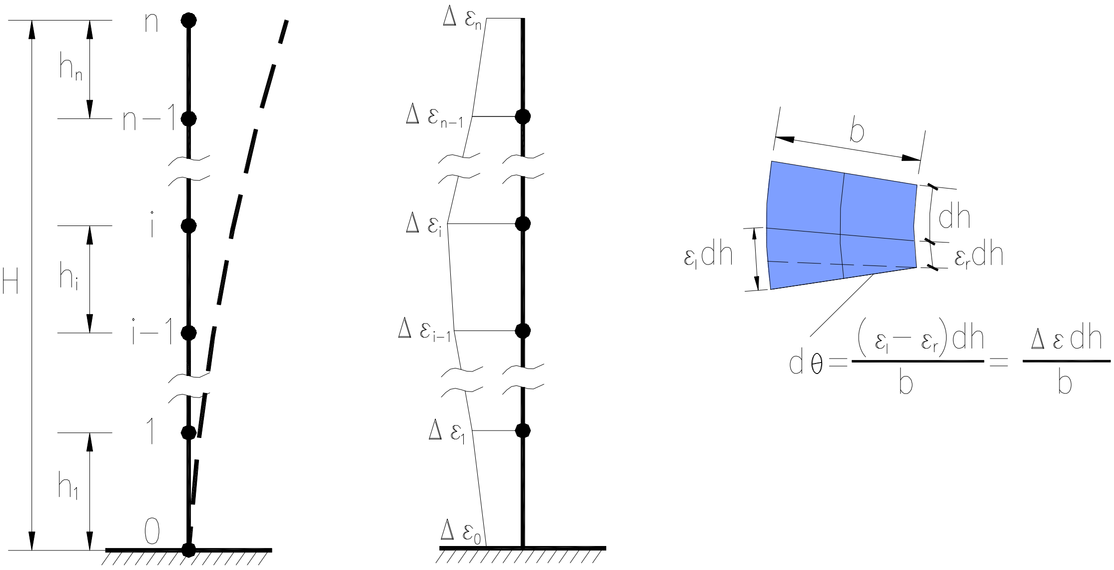

(a) Cantilever beam (b) Strain distribution (c) Deformation of an infinitesimal element

Figure 5-1. Deformed cantilever beam

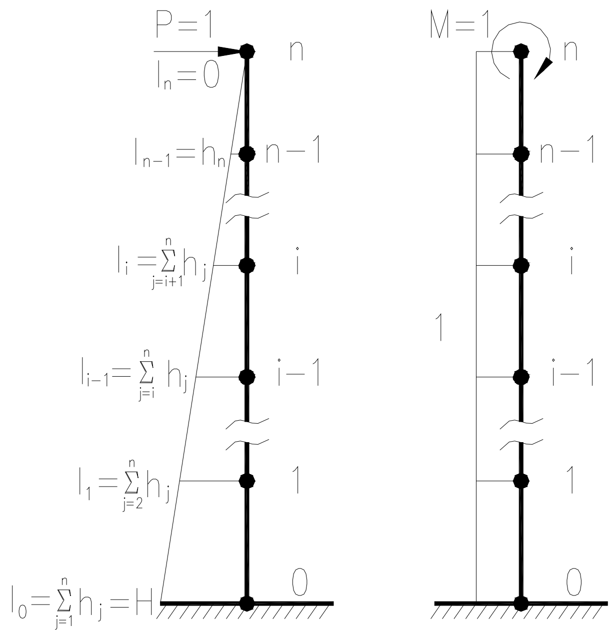

(a) Unit force (b) Unit moment

Figure 5-2. Bending moment diagram (M_u) of the beam subject to a unit virtual force

A unit virtual force is horizontally applied at point n to calculate the horizontal displacement at the top of the beam. The resulting bending moment (M_u) is plotted in Figure 5-2(a). The bending moment at point i is

$$l_i = \sum_{j=i+1}^{n} h_j \qquad (i = 0 \sim n-1) \tag{5-2}$$

$$l_n = 0 \tag{5-3}$$

According to the virtual work theory, the displacement at the top of the beam in Figure 5-2(a) can be calculated as follows:

$$v_n = \int M_u d\theta = \frac{1}{b}\int_0^H M_u \Delta\varepsilon dh \tag{5-4}$$

By using the multiplication diagram, Eq. (5-4) can be calculated as follows:

$$v_n = \frac{1}{6b}\sum_{i=1}^{n}[h_i(2l_{i-1}\Delta\varepsilon_{i-1} + l_{i-1}\Delta\varepsilon_i + l_i\Delta\varepsilon_{i-1} + 2l_i\Delta\varepsilon_i)] \qquad (6\text{-}5)$$

Therefore, the beam top horizontal displacement can be calculated from the strain at different heights.

Similarly, a unit virtual moment is applied at point n to calculate the tilt (or inclination) at the top of the beam. The resulting bending moment is shown in Figure 5-2(b). Therefore, the tilt angle can be calculated as follows:

$$\theta_n = \int M_u d\theta = \frac{1}{b}\int_0^H M_u \Delta\varepsilon dh = \frac{1}{2b}\sum_{i=1}^{n}(\Delta\varepsilon_{i-1} + \Delta\varepsilon_i)h_i \qquad (6\text{-}6)$$

With regarding to the Canton Tower, the vertical strains of the four measuring points of the inner tube on each section in the inner tube are available. Among the 12 critical sections of the inner tube, the strain data measured by the surface-type sensors installed at sections 32.8 and 100.4 m are rather noisy and are therefore disregarded in calculating the deformation of the tower; only the strain data from the ten sections above 100.4 m will be used. The inner tube is then divided to 11 segments (n = 11). According to Eqs. (5-5) and (5-6), the horizontal displacement and tilts along the short and long axis directions of the tower top can be calculated using the measured strain data at each time instance. In particular, the measurements of Points 2 and 4 at these sections are used to calculate the deformation along the short axis direction, and those of Points 1 and 3 are used to calculate the deformation along the long axis direction. Given that point 0 in Figure 5-1 has not been measured, the strain data at point 1 will be used instead, i.e., $\Delta\varepsilon_0 = \Delta\varepsilon_1$. Similarly, $\Delta\varepsilon_{11} = \Delta\varepsilon_{10}$ as the strain at the top of the structure is not available.

5.3 Horizontal Displacement of the Tower Top

To verify the effectiveness of the proposed method, the horizontal displacement and tilt of the tower top derived from the strain data are respectively compared with the measurements using GPS and inclinometer. Considering that the GPS output results are in the east and north directions, the derived displacements are transformed according to the following equation:

$$\begin{bmatrix} X'_d \\ Y'_d \end{bmatrix} = \begin{bmatrix} \cos\alpha & -\sin\alpha \\ \sin\alpha & \cos\alpha \end{bmatrix} \begin{bmatrix} X_d \\ Y_d \end{bmatrix} \tag{5-7}$$

As shown in Figure 5-3, X_d and Y_d are displacements along the short and long axes, respectively; X'_d and Y'_d are displacements to the east and north, respectively; and α is the angle between the long axis and the north.

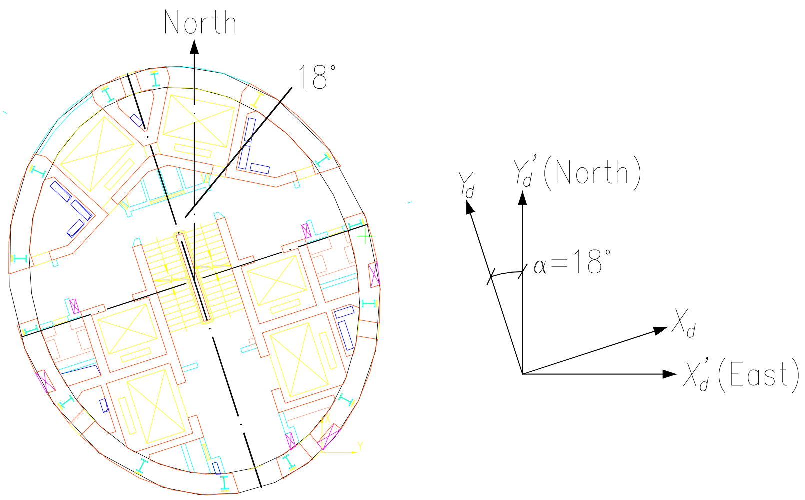

Figure 5-3. Plan view of coordinate transformation

5.3.1 Temperature-induced Displacement

5.3.1.1 One typical sunny day

During sunny days with low wind speed, the deformation of the structure is mainly induced by the temperature variation because there is no other significant loading on the structure. Figure 5-4 shows the air temperature on 3rd December 2008, which was a day when the wind speed was low. Figure 5-5 shows the relative vertical strain variation of the four measurement points at section 121.2 m during the day. Here the strain at midnight (00:00) is set as the initial reference value, with the results calculated at later times indicating relative changes to the reference values. The strain at point 2 (east) increased first at approximately 7:00. Subsequently, the strain at points 3, 4, and 1 increased at approximately 8:00, 12:00, and 14:00, respectively. The maximum strain difference between points 2 and 4 was approximately 15 με, whereas that between points 1 and 3 was approximately 10 με.

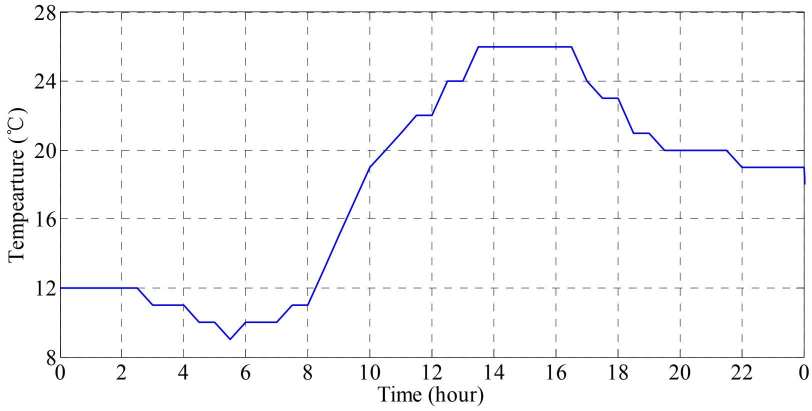

Figure 5-4. Air temperature in Guangzhou on 3rd December 2008

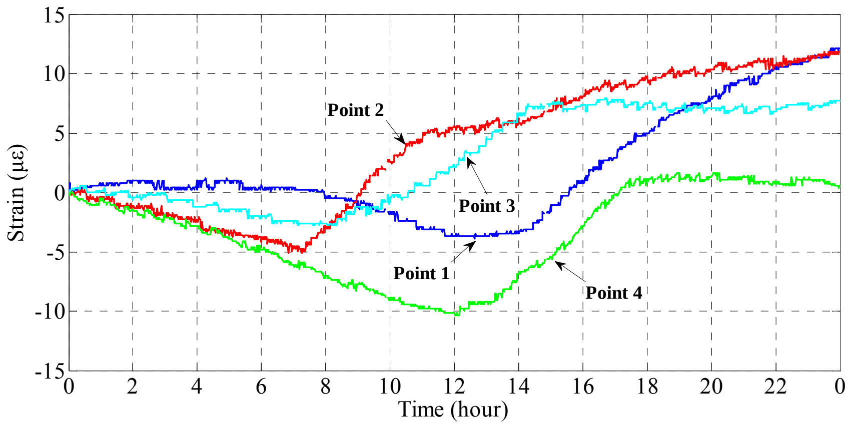

Figure 5-5. Relative strain at section 121.2 m on 3rd December 2008

By using the measured strain data at 10 different sections, the displacement of the tower top in the east and north directions on 3rd December 2008 is calculated and compared with the GPS measurements, as shown in Figure 5-6. The GPS data have a higher sampling frequency compared with that of the strain gauges. Thus, the former were resampled by averaging the data to the same frequency as the latter and then smoothed using the five-point moving average algorithm (Wolberg, 2006). The derived and measured displacement data exhibited the same variation trend. The maximum displacement toward the west and north directions occurred at almost the same time. In particular, the GPS-measured maximum motion was 9.1 cm in the east–west direction and 10.7 cm in the south–north; the corresponding derived values were 11.4 and 8.8 cm.

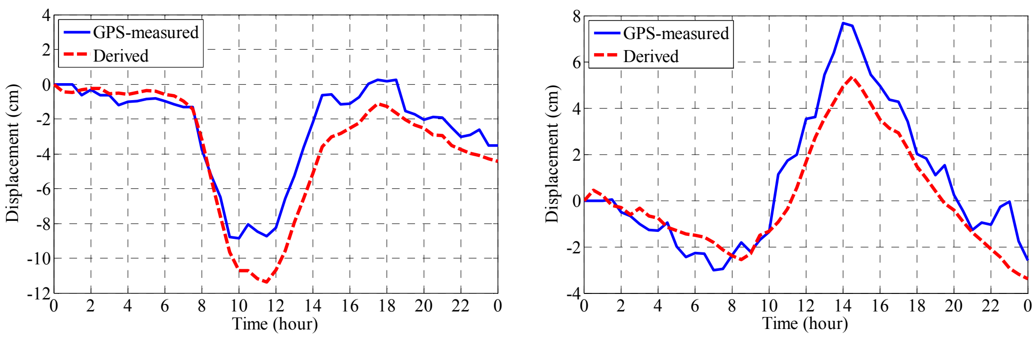

(a) East direction (b) North direction

Figure 5-6. GPS-measured and derived displacements at the top of the inner structure on 3rd December 2008

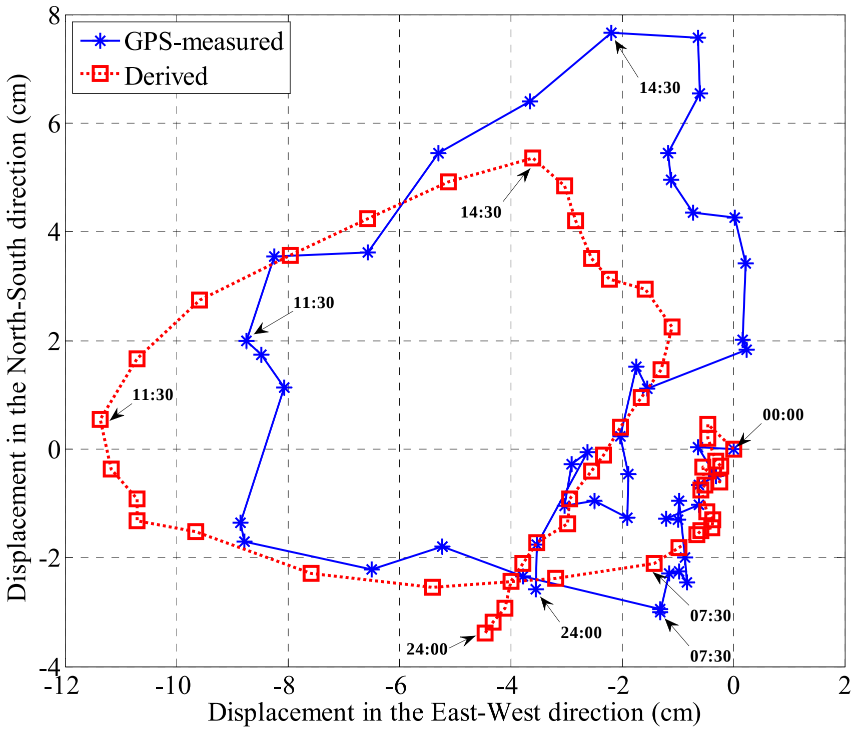

Figure 5-7. Derived and measured displacement track at the top of the inner structure on 3rd December 2008

Figure 5-7 shows the daily movement track at an interval of 0.5 hour. The positions were averaged from the data every half-hour period. Both curves start at 00:00 am from the origin to allow comparison. Both curves exhibit similar moving patterns. The members of the tower that are exposed to the sun received direct solar radiation. Thus, these members had higher temperature compared with those on the shaded facade, causing the structure to bend away from the sun. During early mornings (before 7:00), the movement of the tower was small and slow. After sunrise, the tower started to move toward west and arrived to its westernmost position at approximately 11:30. When the sun moved to the west in the afternoon, the temperature of the members in the southwest increased, causing the tower to move northeast. At 14:30, the tower reached its northernmost position. Afterward, the temperature difference among the tower members decreased, causing the tower to move back gradually from the north to the south.

5.3.1.2 One month displacement

During the in-service monitoring period, the GPS was installed and operated permanently to monitor the displacement of the tower top for a long-term period. The air temperature variation in April 2013 approximately ranged from 12 °C to 31 °C, as illustrated in Figure 5-8. No heavy wind or typhoon occurred during this month. Thus, the deformation of the tower can be primarily attributed to temperature. For this month, the maximum daily temperature difference, which ranged from 18 °C to 30 °C, occurred on 15th April 2013.

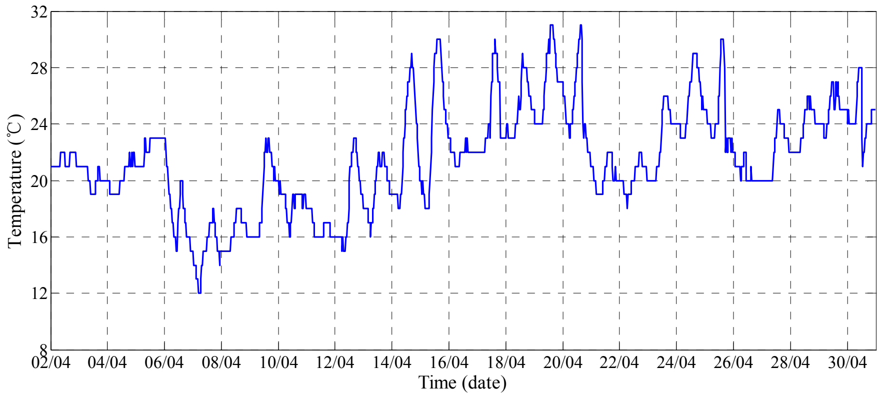

Figure 5-8. Air temperature in Guangzhou in April 2013

The derived and GPS-measured tower top displacement in the east and north directions during April 2013 are compared in Figures 5-9 and 5-10, respectively. The two sets of displacement data exhibit similar variation trend, although a number of discrepancies exist. Most days in April were rainy or cloudy except the 12th, 14th, and 15th. The displacement variations in these three sunny days were much larger than other days. The maximum GPS-measured daily motion during sunny days was 16.1 cm in the east–west direction and 7.4 cm in the south–north; the corresponding derived values were 12.1 and 7.4 cm. The GPS-measured and derived displacement variations during rainy and cloudy days were quite small, that is, less than 6 cm in the east direction and 4 cm in the north. The GPS-measured peak-to-peak motion for the entire month was 18.7 cm in the east–west direction and 12.1 cm in the south–north; the corresponding derived counterparts were 16.3 and 12.1 cm.

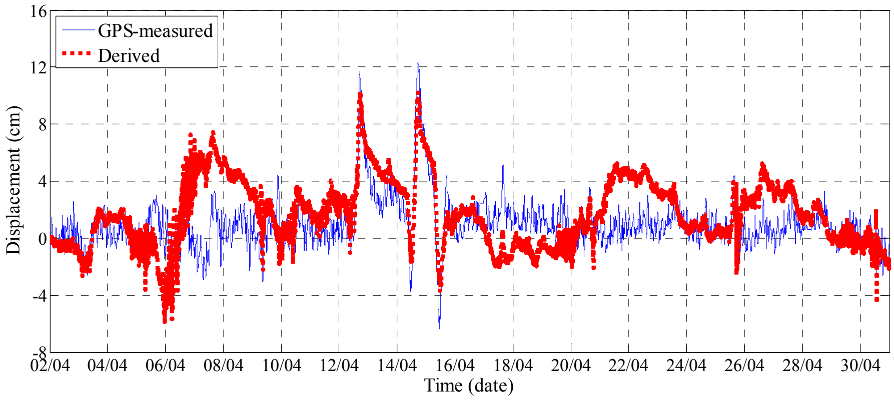

Figure 5-9. GPS-measured and derived displacements at the top of the inner structure in April 2013 (east direction)

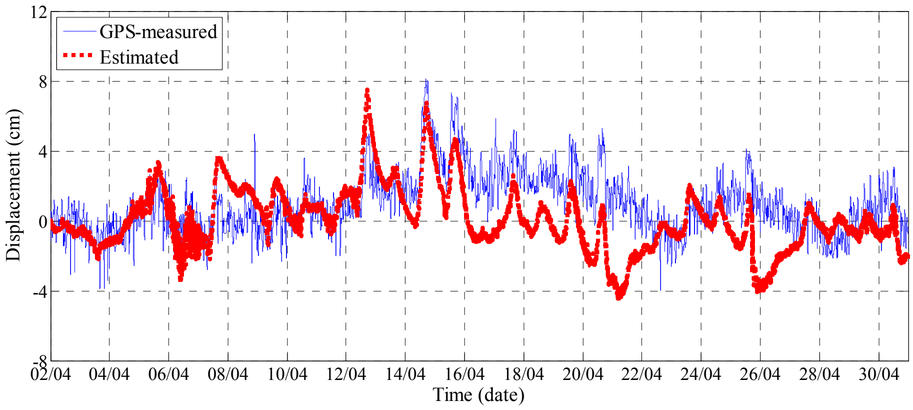

Figure 5-10. GPS-measured and derived displacements at the top of the inner structure in April 2013 (north direction)

5.3.2 Typhoon-induced Displacement

The Canton Tower is located in a typhoon-prone region and is thus subject to several typhoon incidents each year. Typhoon Koppu struck Guangdong Province from 14th September to 15th September in 2009. Figure 5-11 shows the 10-minute mean wind speed, which was measured by the anemometer installed on the top of the tower. The maximum mean wind speed was 20.9 m/s, which occurred approximately between 6:00 to 7:00. The wind speed direction was mainly toward the west.

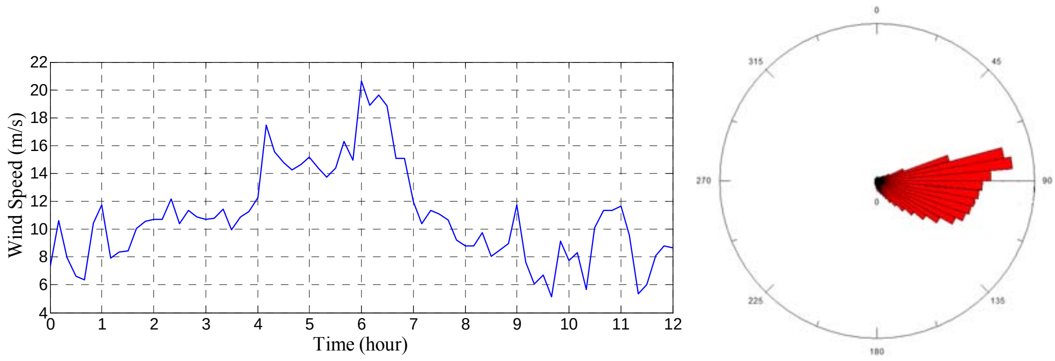

Figure 5-11. Ten-minute mean wind speed at the top of the tower (left) and wind rose diagram (right) on 15th September 2009 during Typhoon Koppu

Figures 5-12 and 5-13 present the comparisons of the derived and measured displacements during this typhoon incident from 19:00 on 14th September to 10:00 on 15th September. The derived displacement exhibited the same pattern as that of the GPS-measured displacement. The maximum displacement in the west direction occurred between 6:00 to 7:00 on 15 September when the wind speed was at its maximum. The GPS-measured peak-to-peak motion was 15.2 cm in the east–west direction and 8.1 cm in the south–north; the corresponding calculated counterparts were 15.3 and 8.4 cm. These measurements are similar to the daily temperature-induced displacements.

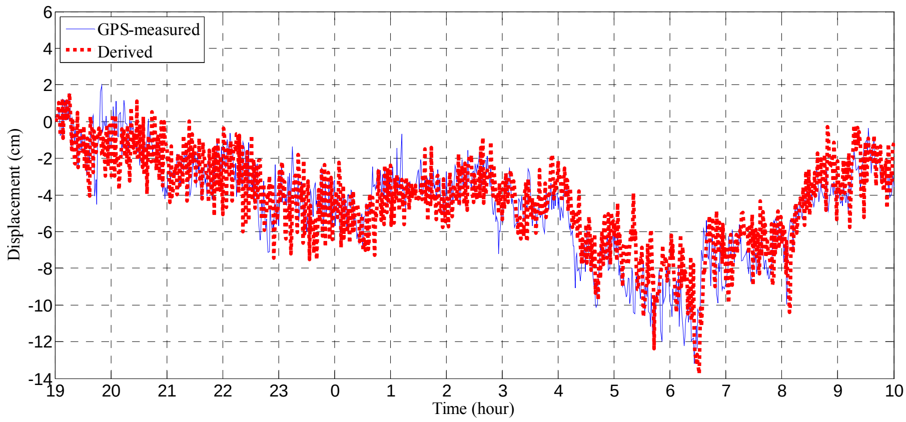

Figure 5-12. Derived and measured typhoon-induced displacement at top of the Tower (east direction)

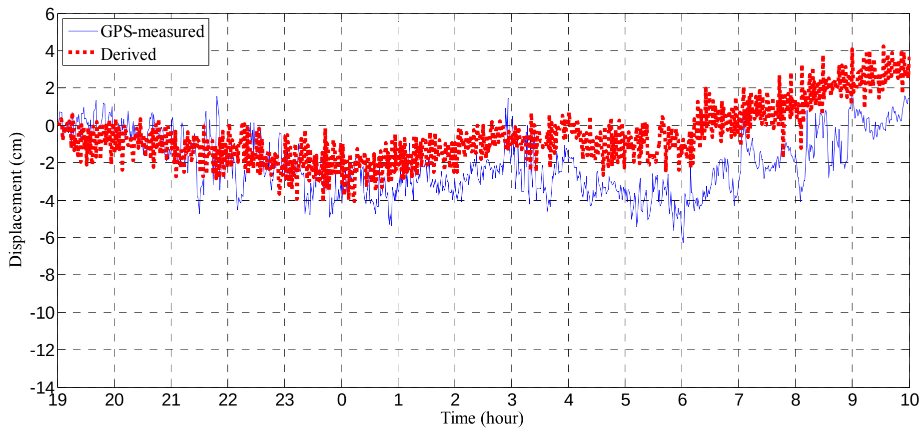

Figure 5-13. Derived and measured typhoon-induced displacement at top of the Tower (north direction)

5.3.3 Temperature-induced Tilt

Both the derived and inclinometer-measured tilts are along the long and short axes of the inner tube. Thus, coordinate transformation is no longer necessary, and the two results can be compared directly. The sampling rate of the inclinometer was 1 Hz. Thus, the measured tilt data are resampled by averaging the data in one minute.

Figure 5-14 compares the measured and derived tilt at the height of 443.4 m on 15th August 2011, which was a typical sunny day. The tilt angle is positive when the tower moves to the southwest along the short axis or to the southeast along the long axis. The air temperature on this day ranged from 27 °C to 36 °C, as shown in Figure 5-15.

As shown in Figure 5-14, the two tilt curves exhibit good agreement, although a number of discrepancies can be found along the long axis. During early morning (before 6:00), the tilt angle had little change. After the sun rose from the southeast, the structural temperatures in the southeast became higher compared with that on the opposite side. The tower bent to the northwest, resulting in an increase in the tilt angle along the short axis and a decrease along the long axis. During the afternoon, the sun moved to the southwest. The structural temperatures in the southwest facade began to rise, causing the tower to move back. The tilt angle along the short axis decreased, whereas that along the long axis increased. The temperature differences between the members on different facades were similar during midnight, and the tower almost moved back to its original location. These observations are similar to the temperature-induced horizontal displacement. The measured peak-to-peak tilt angle was 0.82 mrad along the short axis and 0.18 mrad along the long axis; the corresponding derived counterparts were 0.66 and 0.21 mrad.

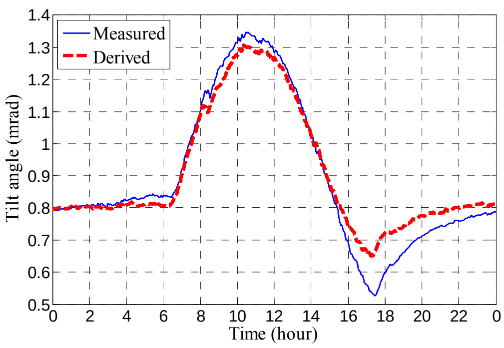

(a) short axis

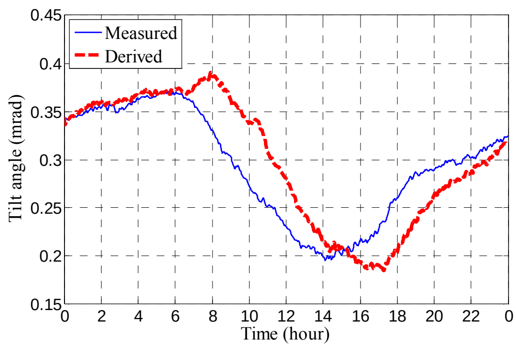

(b) long axis

Figure 5-14. Derived and measured tilts at the height of 443.4 m of the tower on 15th August 2011

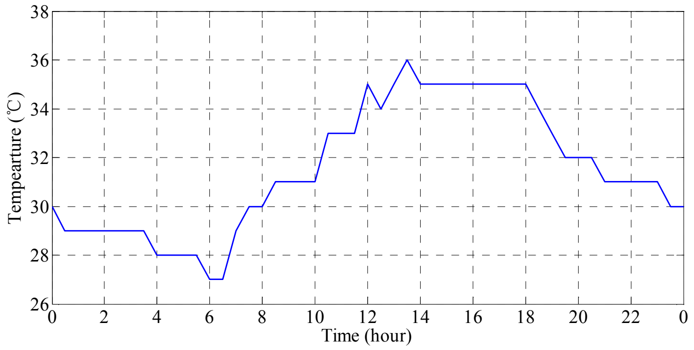

Figure 5-15. Air temperature in Guangzhou on 15th August 2011

5.4 Displacement Mode of the Canton Tower

The above procedure of calculating the deformation at the top of the structure can also be applied to calculating the deformation at other floors by applying the unit virtual force at the corresponding points. By this approach, the deformation mode, or deformation profile of the entire structure along the height can be derived. This is another advantage of the present technique. Figure 5-16 plots the displacement profile of the Tower at 11:30 on 3 December 2008, when the Tower had the maximum horizontal east-west displacement (see Figure 5-7). The south-north displacement was small and not shown here. The deformation showed the bending mode of the entire structure, same as the results obtained in Chapter 4.

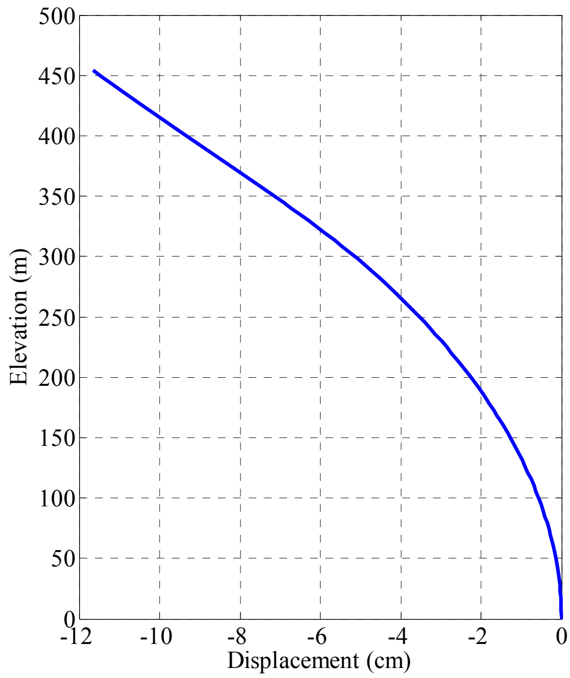

Figure 5-16. Displacement profile of the Tower along the height at 11:30 on 3 December 2008

5.5 Error Analysis

The derived deformation of the structure is subject to uncertainty because the strain measurements contain noise. The accuracy of the derivation depends on two factors. One factor is the beam bending model used in this paper. The assumption of the bending-type deformation can be accepted because the length-to-depth ratio of the main tower is approximately 26.7. The other source of uncertainty is measurement error. According to Eqs. 5-5 and 5-6, the uncertainties of the derived displacement and tilt depend on the measurement error of the strain because the length and section height of each segment could be known accurately. The standard deviation of a multivariate function $y=f(x_1, x_2,\ldots\ldots x_n)$ can be expressed as follows:

$$\sigma_y = \sqrt{(\frac{\partial y}{\partial x_1})^2 \sigma_{x_1}^2 + (\frac{\partial y}{\partial x_2})^2 \sigma_{x_2}^2 + \cdots\cdots + (\frac{\partial y}{\partial x_n})^2 \sigma_{x_n}^2} \tag{5-8}$$

where variables x_i *(i = 1, 2, ..., n)* are independent to each other, and σ is the standard deviation.

By applying Eq. (5-8) to Eq. (5-5), the standard deviation of the derived displacement at the top can be expressed as follows:

$$\sigma_{v_n} = \frac{1}{6b}\sqrt{h_1^2(2l_0 + l_1)^2 \sigma_{\Delta\varepsilon_0}^2 + \sum_{i=1}^{n-1}[h_i(l_{i-1} + 2l_i) + h_{i+1}(2l_i + l_{i+1})]^2 \sigma_{\Delta\varepsilon_i}^2 + h_n^2(l_{n-1} + 2l_n)^2 \sigma_{\Delta\varepsilon_n}^2} \tag{5-9}$$

Similarly, the standard deviation of the tilt at the top can be calculated as follows:

$$\sigma_{\theta_n} = \frac{1}{2b}\sqrt{h_1^2 \sigma_{\Delta\varepsilon_0}^2 + \sum_{i=1}^{n-1}(h_i + h_{i+1})^2 \sigma_{\Delta\varepsilon_i}^2 + h_n^2 \sigma_{\Delta\varepsilon_n}^2} \tag{5-10}$$

In the long axis,

$$\sigma_{\Delta\varepsilon_i}^2 = \sigma_{\varepsilon_{i1}}^2 + \sigma_{\varepsilon_{i3}}^2 \tag{5-11}$$

where $\sigma_{\varepsilon_{i1}}$ and $\sigma_{\varepsilon_{i3}}$ are the standard deviations of the measured strain at points 1 and 3 on the *i*-th section, respectively. Similarly in the short axis,

$$\sigma_{\Delta\varepsilon_i}^2 = \sigma_{\varepsilon_{i2}}^2 + \sigma_{\varepsilon_{i4}}^2 \tag{5-12}$$

where $\sigma_{\varepsilon_{i2}}$ and $\sigma_{\varepsilon_{i4}}$ are the standard deviations of the measured strain at points 2 and 4 on the *i*-th section, respectively.

The standard deviation of each strain sensor can be estimated from the measured strain data. During early morning, the temperatures of the structural members are almost stable and similar. During this period, if the wind speed is low and no special loading acts on the structure, the variation of the measured strain data can be mainly attributed to the measurement noise, and the standard deviation of each sensor can be calculated. The standard deviations of the strain measurements on 3rd

December 2008 are listed in Table 5-1. These measurements range from 0.3 με to 2.6 με, which coincide with the nominal precision of the vibrating wires that is, 1με approximately. If the different strain gauges are presumed to be independent, then the standard deviations of the derived displacements along the long and short axes can be respectively calculated as 0.29 and 0.31 cm according to Eq. (5-9). This uncertainty level is lower than that of the GPS measurements, which accuracy is generally regarded at the centimeter level under ideal conditions and from 5 cm to 10 cm under normal conditions because of numerous practical difficulties such as multipath. Therefore, the proposed strain-based displacement results can achieve higher accuracy compared with the GPS measurement results.

Similarly, the standard deviations of the derived tilt angles along the long and short axes can be respectively calculated as 0.0056 and 0.0084 mrad, according to Eq. (5-10). These calculated values are smaller than the precision of the inclinometer, which has a nominal accuracy of ±0.01 mrad.

Table 5-1. Standard deviations of measured strain on 3rd December 2008

Section No. (elevation)	Standard Deviation (με) Point 1	Point 2	Point 3	Point 4
S3 (121.2 m)	0.27	0.83	1.44	0.96
S4 (173.2 m)	0.30	1.22	0.69	0.83
S5 (204.4 m)	1.27	0.56	0.24	0.75
S6 (230.4 m)	0.36	0.78	0.76	0.68
S7 (272.0 m)	0.75	0.97	1.65	1.56
S8 (303.4 m)	0.41	1.43	0.79	0.60
S9 (334.4 m)	0.84	0.35	0.32	1.47
S10 (355.2 m)	0.32	0.64	2.09	1.00
S11 (386.4 m)	0.44	0.39	1.54	2.58
S12 (438.4 m)	0.42	0.59	1.74	1.10

5.6 Summary

In this chapter, distributed strain data obtained from an SHM system are employed to derive the displacement and tilt of supertall buildings. The derivation is based on the assumption that the inner tube is a bending type structure and that shear deformation can be ignored in the sections. The comparison shows that the indirectly-derived horizontal displacement and tilt of the Canton Tower are in good agreement with the direct measurements using GPS and the inclinometer, indicating that the proposed method can calculate the deformation of the supertall structure. The deformation mode of the Canton Tower is also calculated through the proposed method and the results shows the bending deformation type. Error analysis shows that the derived displacement has higher accuracy that the GPS-measured results. In addition, the derived tilt has similar accuracy with the inclinometer-measured results. Aside from buildings, the proposed technique in this chapter can be applied to bridges if the strains at different sections are available.

CHAPTER SIX

TEMPERATURE EFFECT ON VIBRATION PROPERTIES OF CANTON TOWER

It is widely recognized that the changing environmental conditions, especially the temperature, could cause the changes in structural vibration properties, such as frequencies, damping and mode shapes. Some studies have found that the changes could be more significant than those caused by a medium degree of structural damage (Salawu 1997) or under normal operational loads (Xu 2010). Fully understanding the temperature effects on structural vibration properties is particularly important in vibration-based structural condition assessment and damage detection. In this chapter, the correlation between modal properties and temperature of the Canton Tower are investigated using the long-term SHM data.

6.1 Field Vibration Measurement System for Canton Tower

Twenty uni-axial accelerometers (Tokyo Sokushin AS-2000C) were installed at eight different cross sections of the inner tube considering the availability of space and access to the data acquisition units, as shown in Figure 6.1. The frequency range of the sensors is DC-50 Hz (3 dB). The amplitude range is ±2 g and the sensitivity 1.25 V/g. The 4th and the 8th sections were equipped with four accelerometers, two for measuring horizontal vibrations along the long axis and the other two for the short axis of the inner tube. At six other sections, each is equipped with two accelerometers, one for the long axis and the other for the short axis of the inner tube. The sensors were fixed firmly on the shear wall of the inner tube and locked in a steel box for protection, as shown in Figure 6-2.

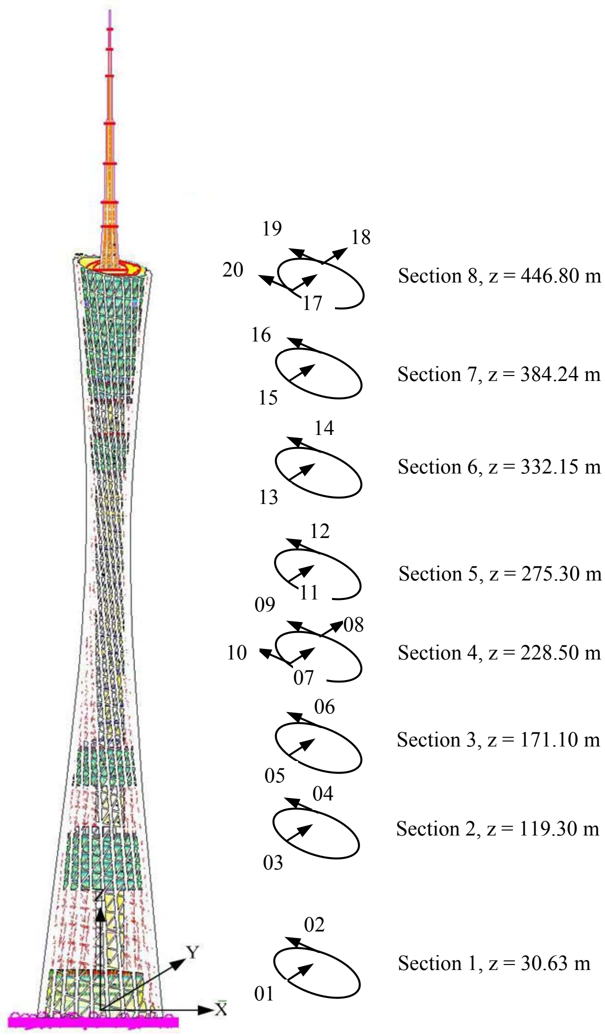

(a) Floors with the accelerometers

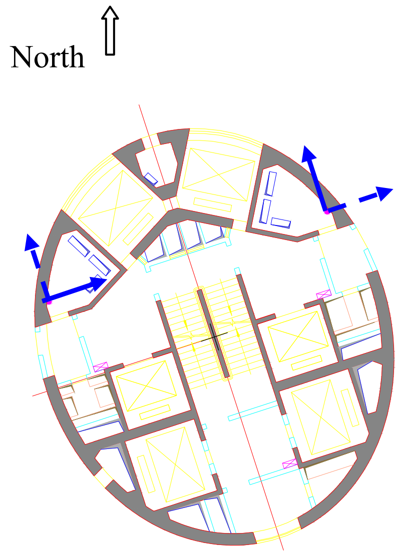

(b) Plan of the inner tube and the direction of the accelerometers

Figure 6-1. Layout of accelerometers installed on Canton Tower

Figure 6-2. Accelerometers installed on Canton Tower

At each cross section, an acquisition unit was placed around to collect the acceleration data. The total eight acquisition units were connected in series via two cables, one for synchronization and the other for acceleration data transmission. One PC in the tower is responsible for sending synchronization signal and collecting acceleration data. A bandwidth filter of 0.05 – 40 Hz was designed in each acquisition unit. The system has 24 bit A/D converters. An amplifier is used in each unit to amplify the acceleration signal by 1000 times. The sampling rate of the acceleration data is set to 50 Hz.

6.2 Quantitative Analysis

It is widely believed that variations in natural frequencies of structures with temperature are caused by change in material properties, in particular, the modulus of elasticity. To quantify the effect of temperature on natural frequencies, a single-span or multi-span prismatic beam made of an isotropic material is used as an example. Its undamped flexural vibration frequency of order *n* is (Blevins 1979):

$$f_n = \frac{\lambda_n^2}{2\pi l^2}\sqrt{\frac{EI}{\mu}} \tag{6-1}$$

where λ_n is a dimensionless parameter and is a function of the boundary conditions, l is the length of the beam, μ is the mass per unit length, E is the modulus of elasticity, and I is the moment of inertia of the cross-sectional area. It is assumed that variations in temperature will not affect mass and boundary conditions, but only the geometry of the structure and the mechanical properties of the material.

It can be shown that

$$\frac{\delta f_n}{f_n} = -2\frac{\delta l}{l} + \frac{1}{2}\frac{\delta E}{E} + \frac{1}{2}\frac{\delta I}{I} - \frac{1}{2}\frac{\delta \mu}{\mu} \tag{6-2}$$

where δ represents an increment in the corresponding parameters. Assuming that the thermal coefficient of linear expansion of the material is θ_T and the thermal coefficient of modulus is θ_E, one obtains

$$\begin{aligned} \frac{\delta l}{l} &= \theta_T \delta T \\ \frac{\delta E}{E} &= \theta_E \delta T \\ \frac{\delta I}{I} &= 4\theta_T \delta T \\ \frac{\delta \mu}{\mu} &= -\theta_T \delta T \end{aligned} \tag{6-3}$$

Here, we assume that variations in Young's modulus with temperature are linear for small changes in temperature, variations in moment of area are four times the variations in linear expansion, and the mass per unit length is inversely proportional to the length as the total mass is a constant. Consequently, Eq. (6-2) yields

$$\frac{\delta f_n}{f_n} = \frac{1}{2}(\theta_T + \theta_E)\delta T \tag{6-4}$$

Eq. (6-4) estimates the dimensionless rate of the frequency change with the temperature change. The linear thermal expansion coefficients (θ_T) of steel (Brockenbrough 1999) and concrete (CEB-FIP) are 1.1×10^{-5} and 1.0×10^{-5}/°C, respectively. The modulus thermal coefficients (θ_E) of the two materials are -3.6×10^{-4} and -3.0×10^{-3}/°C, respectively. θ_E is obviously much larger than θ_T for the two materials, which indicates that variations in natural frequency subjected to temperature change are controlled by θ_E. It also shows that the variation percentage of natural frequency is a function of the modulus thermal coefficients only, regardless of modes, spans, and boundary conditions (simply-supported or cantilever beam). Consequently, theoretical variation percentages of the natural frequency of steel beams and RC beams are 0.018% and 0.15% per degree Celsius, respectively. The big difference in the modulus thermal coefficient contributes to significantly different observations. For example, variations in natural frequencies of a steel beam and an RC beam are about 0.36% and 3.0%, respectively, under a temperature change of 20 °C. The former is difficult to observe in practice and may be masked by measurement noise or other factors, especially for lower modes with small absolute frequencies.

6.3 Variation in Vibration Properties with Respect to Temperature

6.3.1 Data Processing and Modal Parameter Identification

The measured acceleration data are firstly de-trended before conducting the modal parameter identification. It was performed by subtracting the mean values calculated over the full duration of each measurement and could remove the DC-components which can badly influence the identification results.

A sampling frequency of 50 Hz on the measurement in a frequency ranges from 0 to 25 Hz. For the supertall Canton Tower, the first few natural frequencies are within 2 Hz. Therefore, re-sampling of the raw measurement data was then carried out, which can make the following processing faster. A re-sampling and filtering from 50 to 5 Hz was conducted which led to a frequency range from 0 to 2.5 Hz.

After the pre-processing procedure, the modal properties were extracted by using the Enhanced Frequency Domain Decomposition (EFDD) method (Brincker 2000). The data processing and modal parameter identification were carried out by using ARTeMIS Extractor software.

Table 6-1 lists the identified modal properties of Canton Tower and natural frequencies calculated from the FE analysis. The identified results are obtained by using the measured acceleration data between 0:00 to 1:00 on 1 January 2014. It is noticed that the several identified natural frequencies of low modes agree well with the FE analytical ones, whereas in the higher modes, relative larger errors are observed. The first five bending mode shapes in both short and long axis are also obtained, as shown in Figure 6-3.

Table 6-1. Identified modal properties and FE results

Modal characteristic	FE results	Identified results	
	Frequency (Hz)	Frequency (Hz)	Damping ratio (%)
1st short axis bending	0.1088	0.09182	1.723
1st long axis bending	0.1570	0.1341	1.032
2nd short axis bending	0.3660	0.3723	0.4646
2nd long axis bending	0.4711	0.4628	0.4186
3rd short axis bending	0.7157	0.7979	0.326
3rd long axis bending	0.9005	0.9667	0.1929
4th short axis bending	1.1942	1.404	0.1545
4th long axis bending	1.4526	1.635	0.1833
5th short axis bending	1.6981	1.933	0.3800
5th long axis bending	2.0393	2.285	0.3826
1st torsion	0.4556	0.4992	0.2934
2nd torsion	1.0814	1.251	0.2076

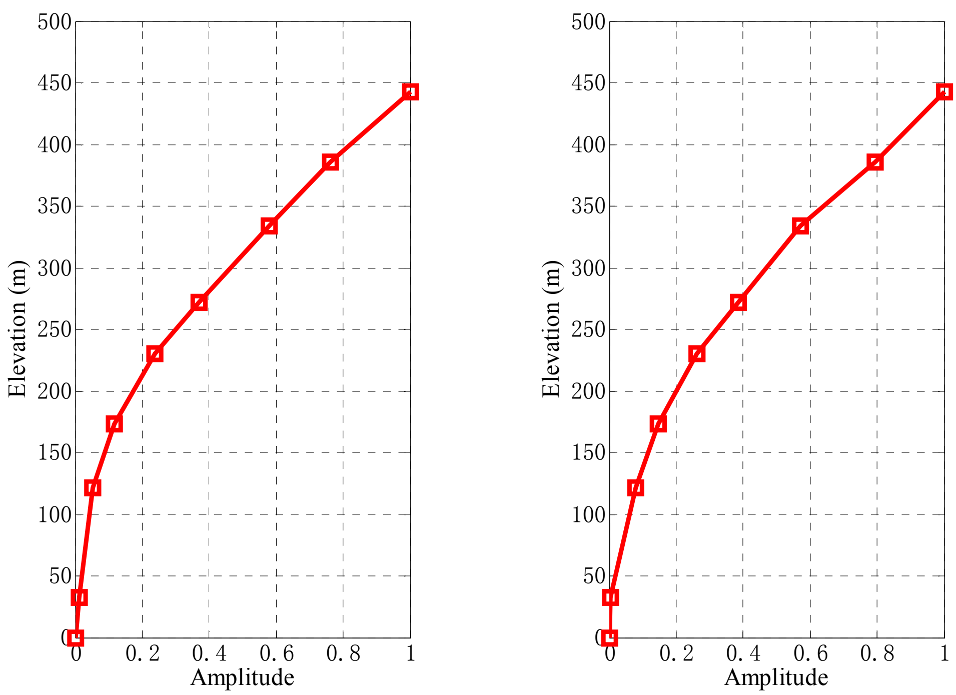

(a) 1st short axis (b) 1st long axis

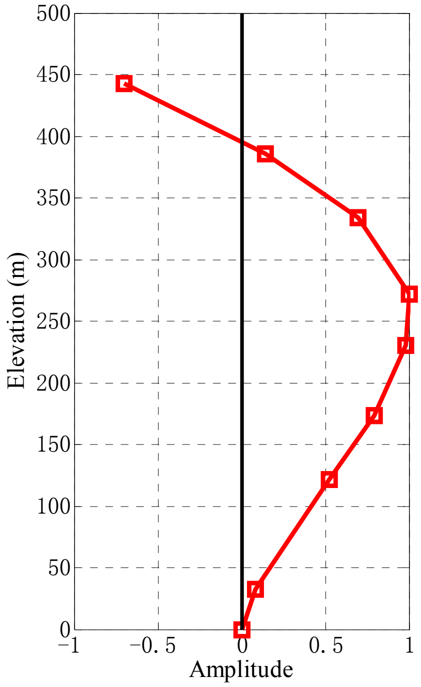

(c) 2nd short axis

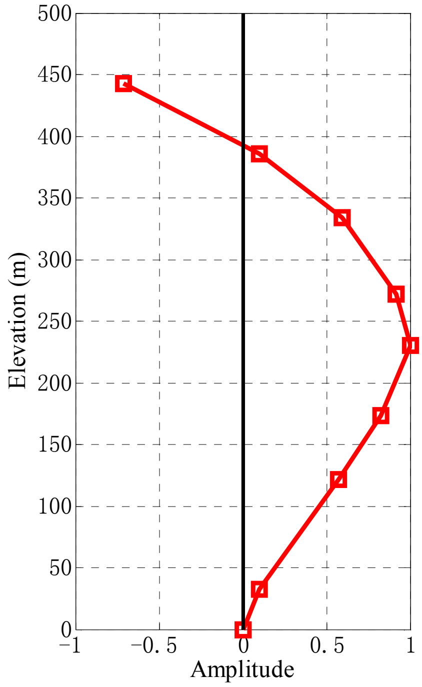

(d) 2nd long axis

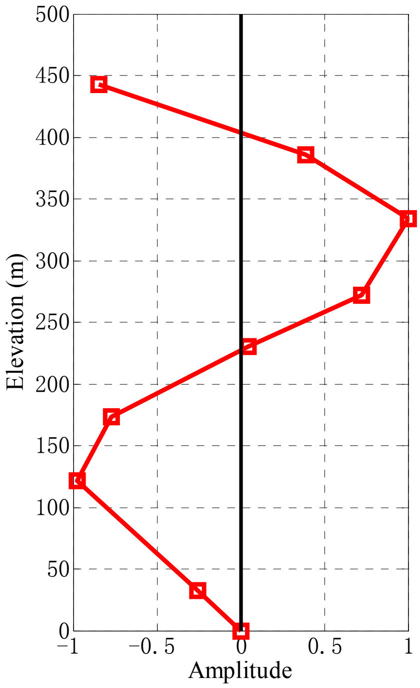

(e) 3rd short axis

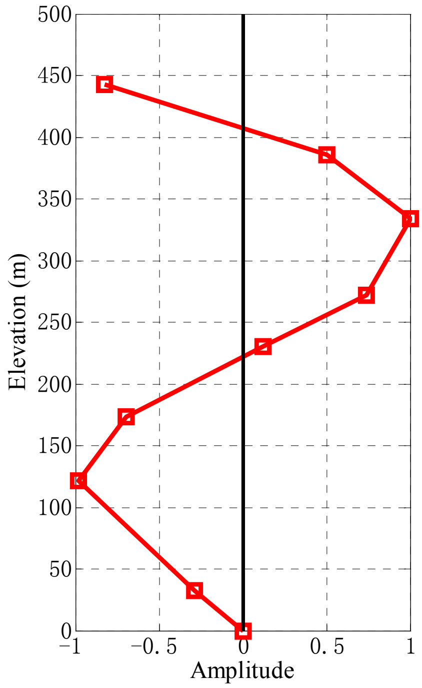

(f) 3rd long axis

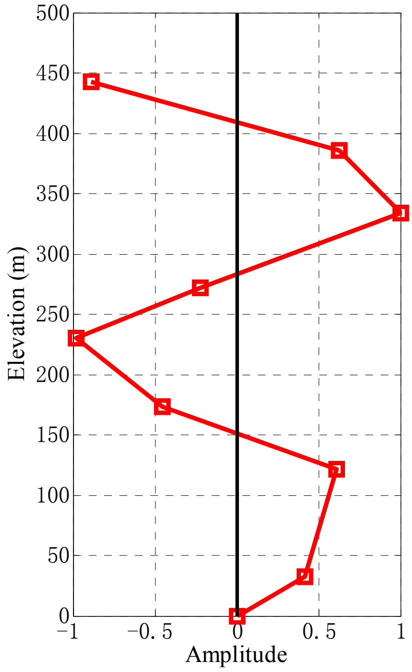

(g) 4th short axis

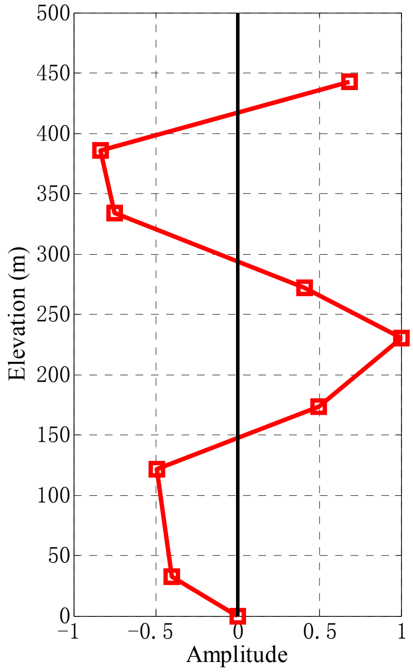

(h) 4th long axis

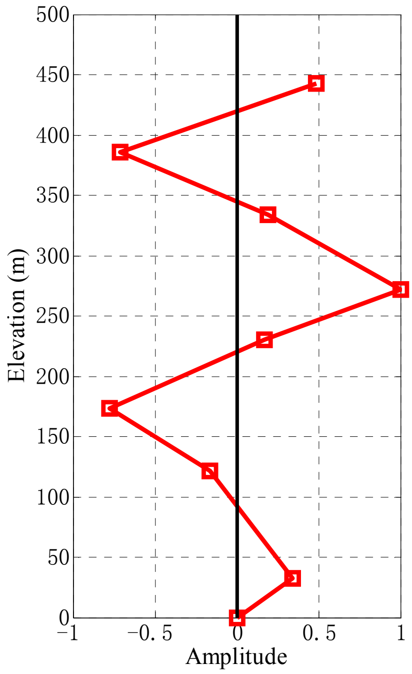

(i) 5th short axis

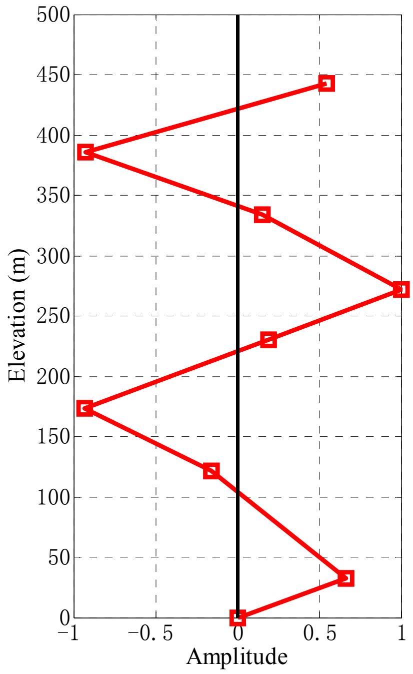

(j) 5th long axis

Figure 6-3. The first five bending mode shapes in short and long axes

6.3.2 Variations in Frequency with Respect to Temperature

Variations in the first four bending frequencies extracted from the acceleration data versus the ambient air temperature on 1 January 2014, 24 March 2014, 23 July 2014 and 12 October 2014 in four different seasons are studied here. All of the above four days are sunny days and the wind speed in these days was small. The frequencies include two bending modes along the short axis and two bending modes along the long axis of the inner tube.

Figures 6-4, 6-6, 6-8 and 6-10 show the variations in the first four vertical frequencies and temperature on 1 January 2014, 24 March 2014, 23 July 2014 and 12 October 2014, respectively. In these figures, the frequency data at each hour are obtained from the acceleration data recorded during that hour, and the temperature is the averaged ambient air temperature over the hour. Based on these figures, it is can be noticed that all of the frequencies generally decreased when the temperature went up before noon, whereas they increased as the temperature dropped in the afternoon although the variations are quite small. The minimum frequencies and the maximum temperatures do not occur at the same time, and the time difference is approximately three hours.

The variation percentage of the frequencies with respect to ambient air temperature in these four days are shown in Figures 6-5, 6-7, 6-9 and 6-11, in which the frequencies are divided by the maximum values of the mode. The variation trends of the first four modal frequencies are very similar and the maximum variations are approximately 0.6% to 1.8%.

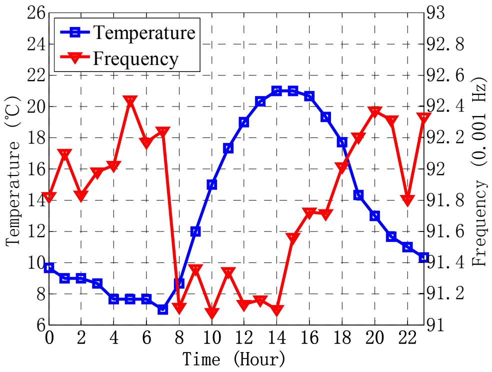

(a) 1st short axis

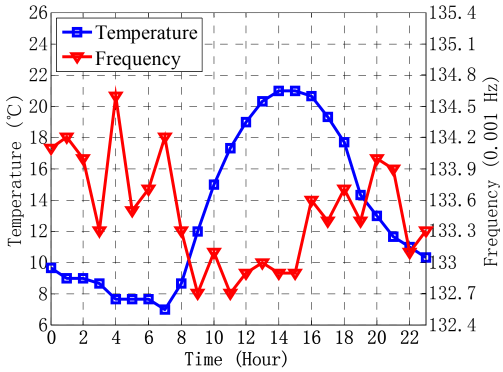

(b) 1st long axis

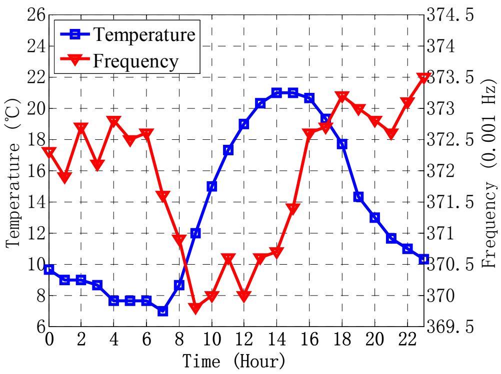

(c) 2nd short axis

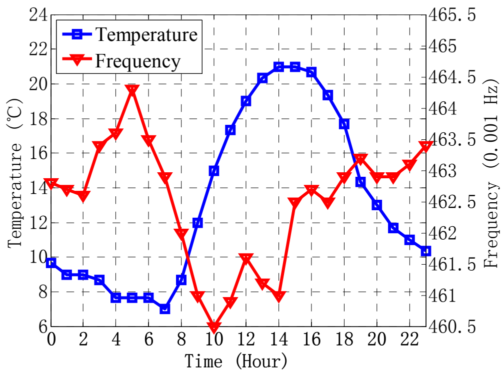

(d) 2nd long axis

Figure 6-4. Variations in frequencies versus air temperature of Canton Tower on 1 January 2014

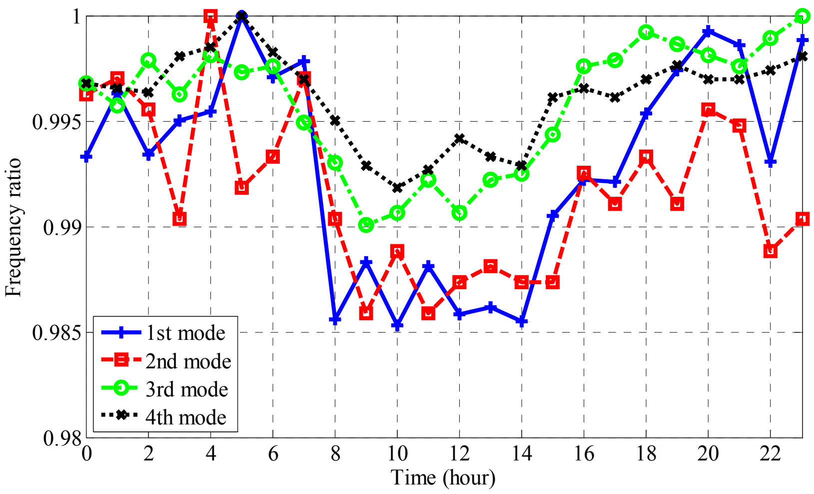

Figure 6-5. Variation percentage of frequencies on 1 January 2014

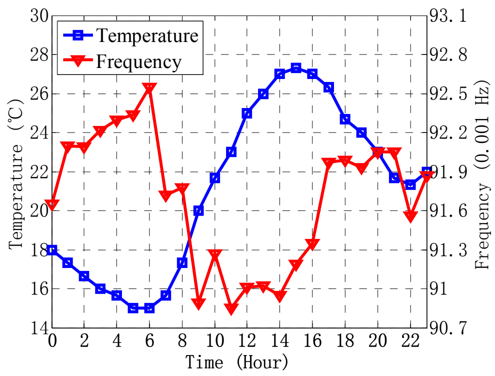

(a) 1st short axis

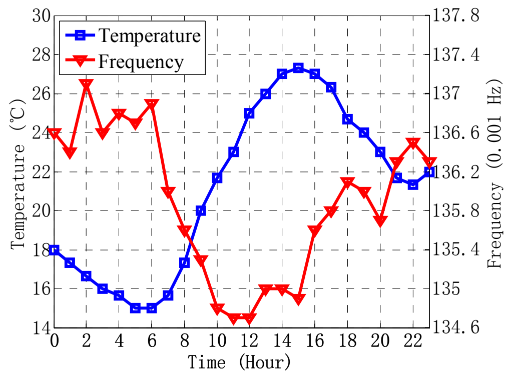

(b) 1st long axis

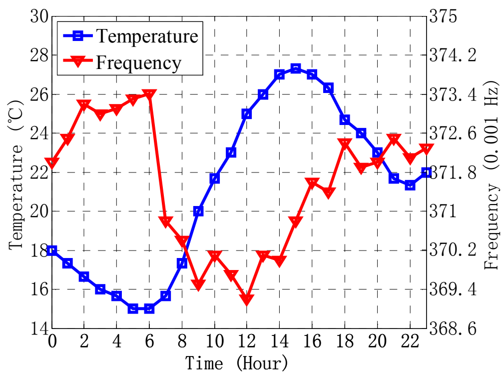

(c) 2nd short axis

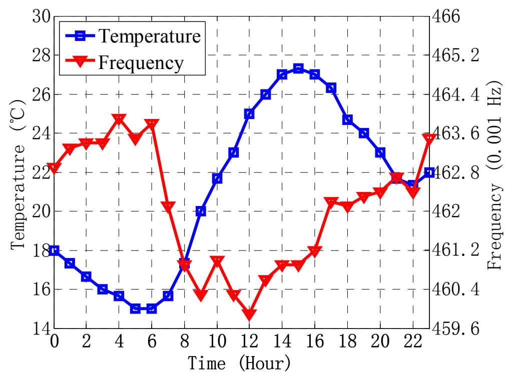

(d) 2nd long axis

Figure 6-6. Variations in frequencies versus air temperature of Canton Tower on 24 March 2014

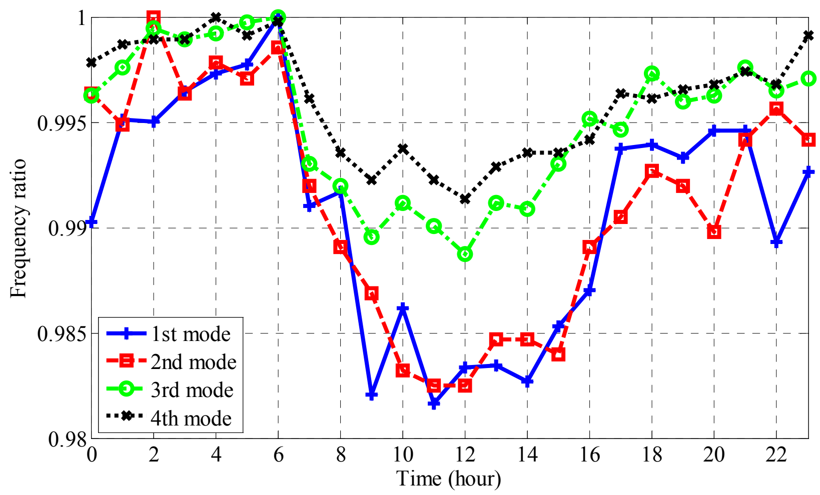

Figure 6-7. Variation percentage of frequencies on 24 March 2014

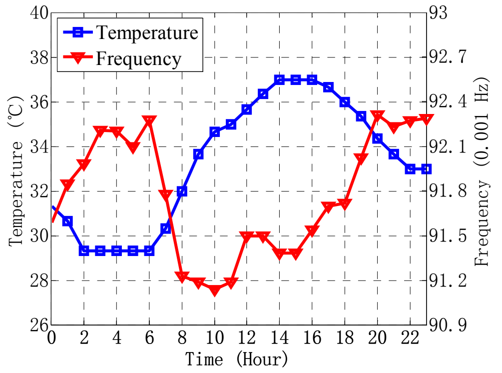

(a) 1st short axis

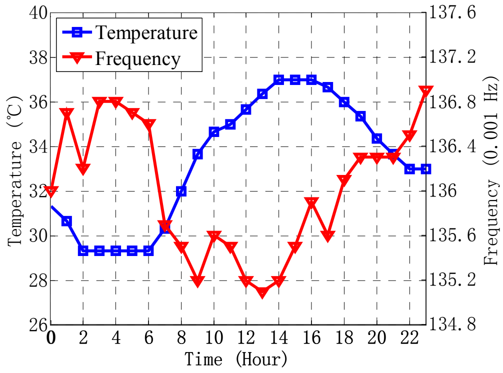

(b) 1st long axis

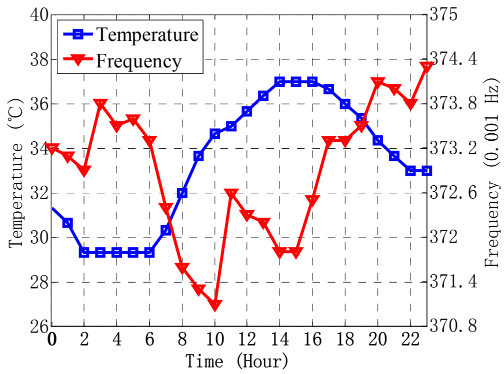

(c) 2nd short axis

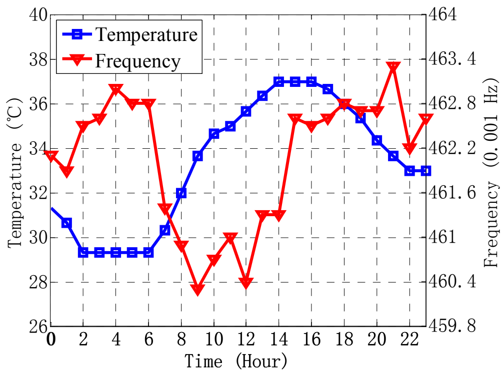

(d) 2nd long axis

Figure 6-8. Variations in frequencies versus air temperature of Canton Tower on 23 July 2014

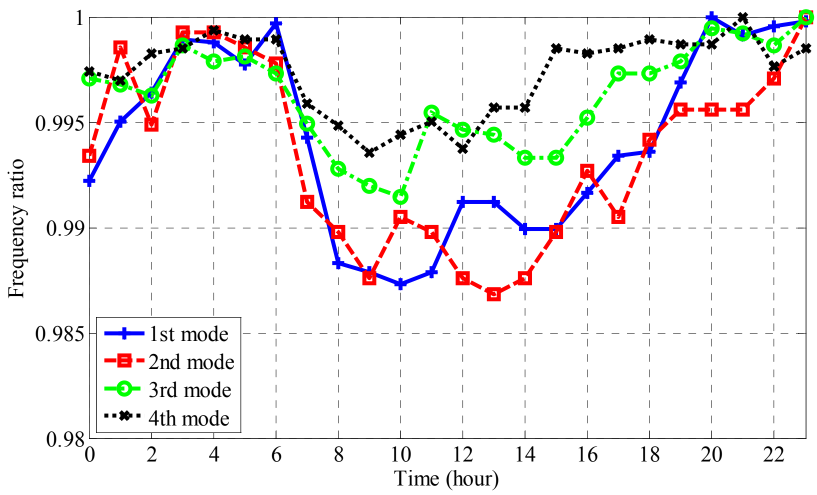

Figure 6-9. Variation percentage of frequencies on 23 July 2014

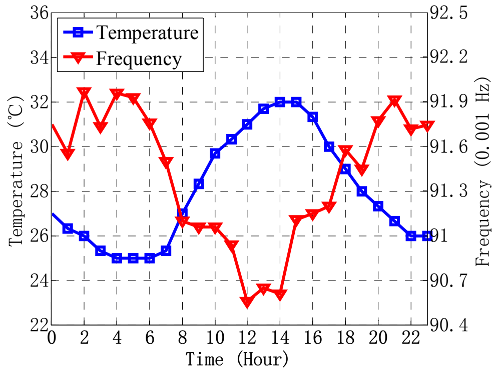

(a) 1st short axis

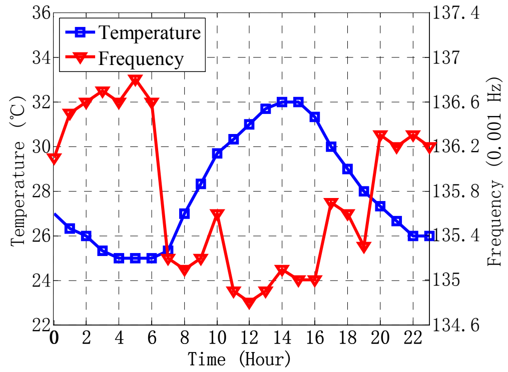

(b) 1st long axis

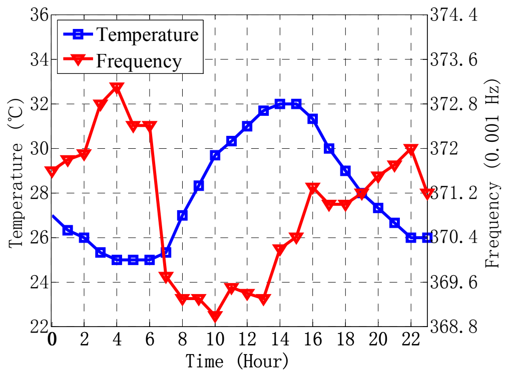

(c) 2nd short axis

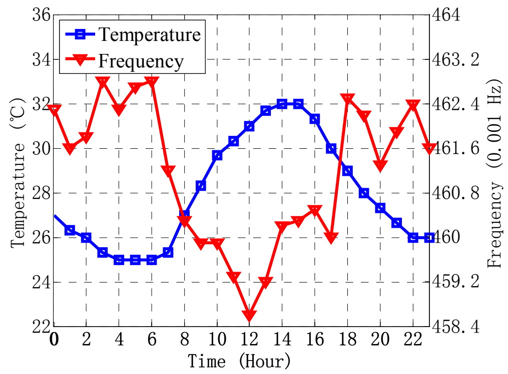

(d) 2nd long axis

Figure 6-10. Variations in frequencies versus air temperature of Canton Tower on 12 October 2014

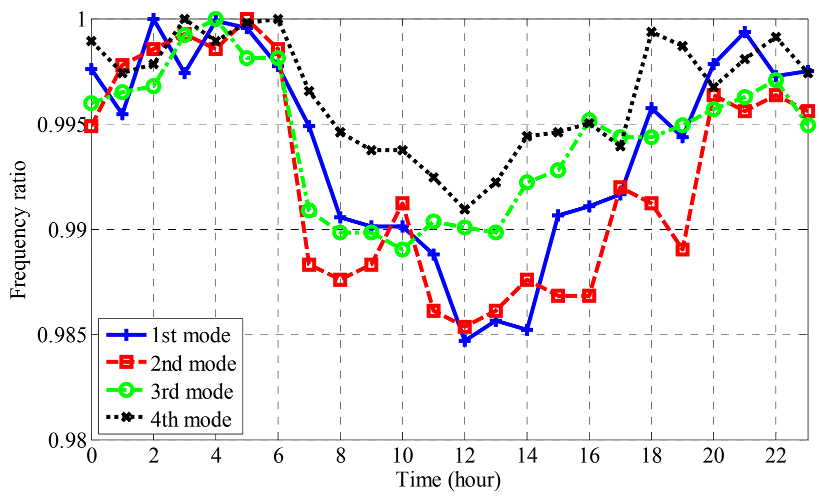

Figure 6-11. Variation percentage of frequencies on 12 October 2014

6.3.3 Quantitative Relation between Frequency and Temperature

The linear regression technique is utilized to examine the relation between the frequencies and the structural temperature of the models. A linear regression model has the form of

$$f = \beta_0 + \beta_T T + \varepsilon_f \tag{6-5}$$

where f is the frequency, T is the ambient air temperature variable, β_0 (intercept) and β_T (slope) are the regression coefficients, and ε_f is the regression error.

The fitted regression lines of the first four natural frequencies versus air temperature of the Canton Tower in four days in different seasons with 95% confidence bounds are plotted in Figures 6-12 to 6-15.

The regression coefficients of the Canton Tower are also obtained and listed in Table 6-2 to 6-5 for each mode. The slope β_T represents frequency change with respect to temperature and the intercept β_0 represents the frequency at 0 °C. For comparison of different modes, β_T is normalized to β_0 and listed in Table 6-2 to 6-5 as well. β_T/β_0 indicates the percentage of the frequency change when the structural temperature increases by unit degree Celsius.

The correlation coefficients of several cases in the four days are between 0 to -0.5, implying the linear correlation between the air temperature and the natural frequencies are not very good. This is because the temperature is non-uniformly distributed across the tower and the frequencies are global properties and are associated with the temperature distribution of the entire structure. Different components have different contributions to the global frequencies, and using one temperature may not represent the variations of the whole structure.

For those modes with the correlation coefficients between -0.6 to -1.0 (indicating a good correlation), the modal frequencies of the Canton Tower decrease by approximately 0.079% to 0.162%, when the structural temperature increases by unit degree Celsius. This value is close to half of the modulus thermal coefficients of the concrete (θ_E = 0.30% for concrete, respectively) according to Eq. (6-4). This verifies Eq. (6-4) and indicates that the variations in the bending frequencies of the structures are mainly caused by the change in the modulus of the materials.

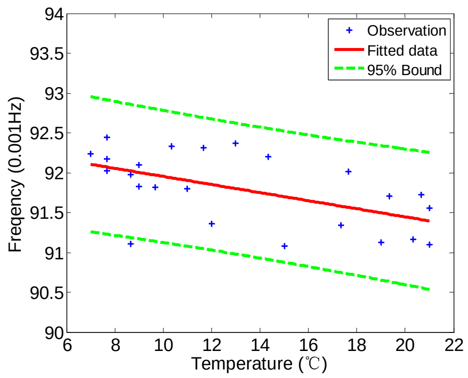

(a) 1st mode

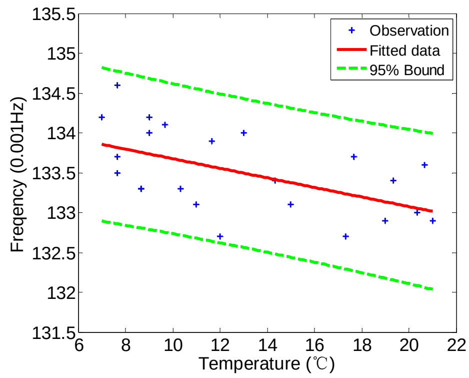

(b) 2nd mode

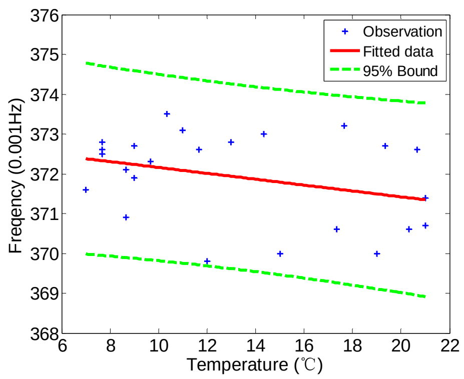

(c) 3rd mode

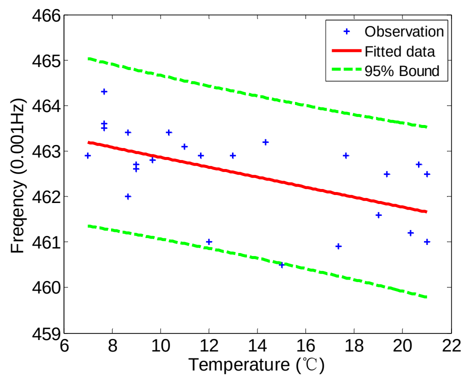

(d) 4th mode

Figure 6-12. Relation of natural frequencies to temperature of Canton Tower on 1 January 2014

Table 6-2. Regression coefficients of the models on 1 January 2014

Mode	Correlation Coefficient	$\beta_0\,(10^{-3})$	$\beta_t\,(10^{-3})$	$\beta_t/\beta_0\ (10^{-3})$
1	-0.56	92.5	-0.051	-0.549
2	-0.57	134.3	-0.06	-0.447
3	-0.33	372.9	-0.074	-0.198
4	-0.56	464.0	-0.11	-0.237

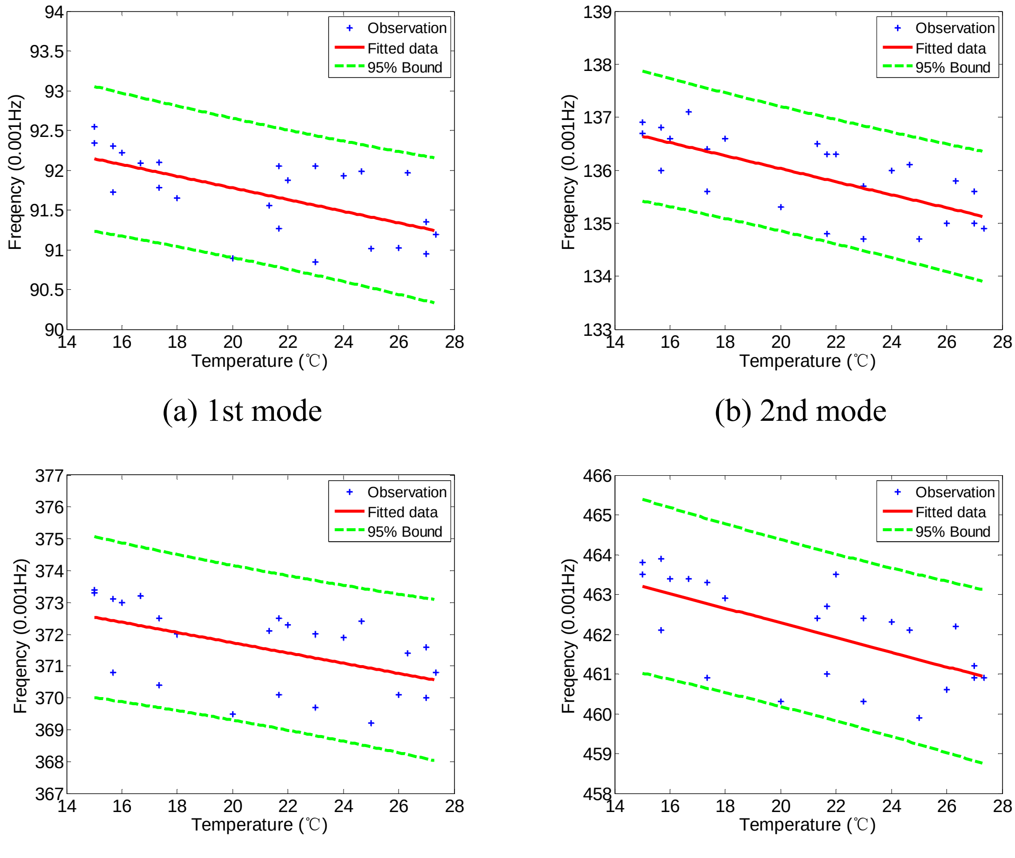

(a) 1st mode

(b) 2nd mode

(c) 3rd mode

(d) 4th mode

Figure 6-13. Relation of natural frequencies to temperature of Canton Tower on 24 March 2014

Table 6-3. Regression coefficients of the models on 24 March 2014

Mode	Correlation Coefficient	$\beta_0\,(10^{-3})$	$\beta_t\,(10^{-3})$	$\beta_t/\beta_0\ (10^{-3})$
1	-0.61	93.2	-0.07	-0.79
2	-0.70	138.5	-0.12	-0.89
3	-0.52	374.9	-0.16	-0.43
4	-0.63	466.0	-0.18	-0.40

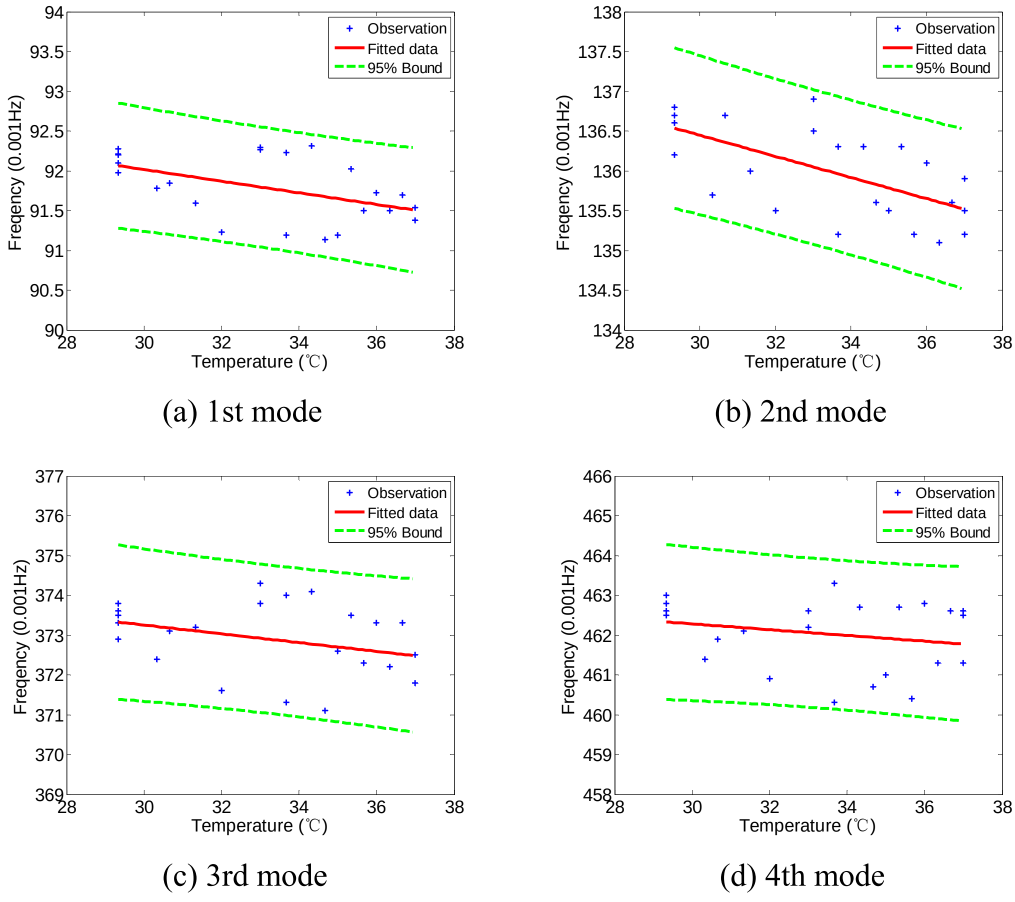

(a) 1st mode

(b) 2nd mode

(c) 3rd mode

(d) 4th mode

Figure 6-14. Relation of natural frequencies to temperature of Canton Tower on 23 July 2014

Table 6-4. Regression coefficients of the models on 23 July 2014

Mode	Correlation Coefficient	$\beta_0\,(10^{-3})$	$\beta_t\,(10^{-3})$	$\beta_t/\beta_0\ (10^{-3})$
1	-0.51	94.2	-0.07	-0.78
2	-0.64	140.4	-0.13	-0.95
3	-0.34	376.6	-0.11	-0.29
4	-0.23	464.5	-0.07	-0.16

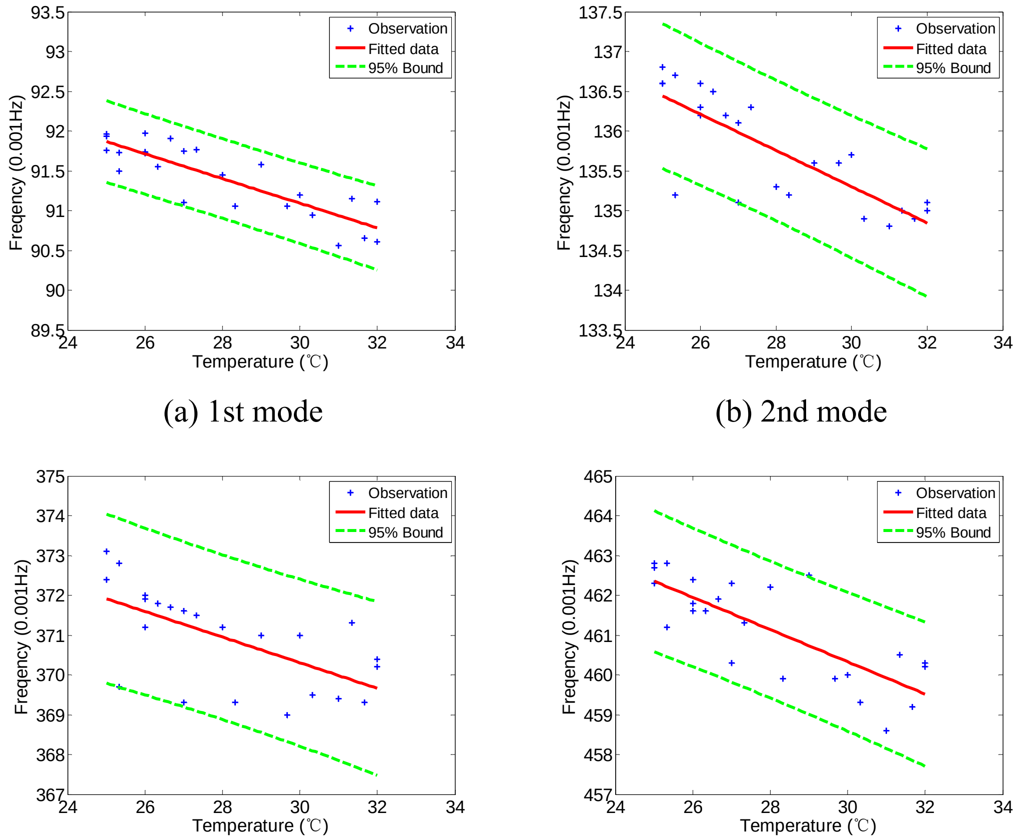

(a) 1st mode (b) 2nd mode

(c) 3rd mode (d) 4th mode

Figure 6-15. Relation of natural frequencies to temperature of Canton Tower on 12 October 2014

Table 6-5. Regression coefficients of the models on 12 October 2014

Mode	Correlation Coefficient	$\beta_0\,(10^{-3})$	$\beta_t\,(10^{-3})$	$\beta_t/\beta_0\ (10^{-3})$
1	-0.86	95.7	-0.16	-1.62
2	-0.81	142.1	-0.23	-1.60
3	-0.64	380.0	-0.32	-0.85
4	-0.78	472.49	-0.41	-0.86

Ration of all the first four natural frequencies in four days with the correlation coefficient less than -0.5 versus the temperature are illustrated in Figure 6-16, in which the frequencies are normalized with β_0 of the mode (intercept at temperature 0 °C). A good linear correlation can be observed for all modes, and the slope of the linearly fitted curve is -1.32×10^{-3}, very close to half of the modulus thermal coefficients of concrete ($\theta_E = -3.0\times10^{-3}/^{o}C$), as described in Eq. (6-4). This implies that even this large-scale structure is quite complicated, variations in the bending frequencies are mainly caused by modulus change of the material under different temperatures.

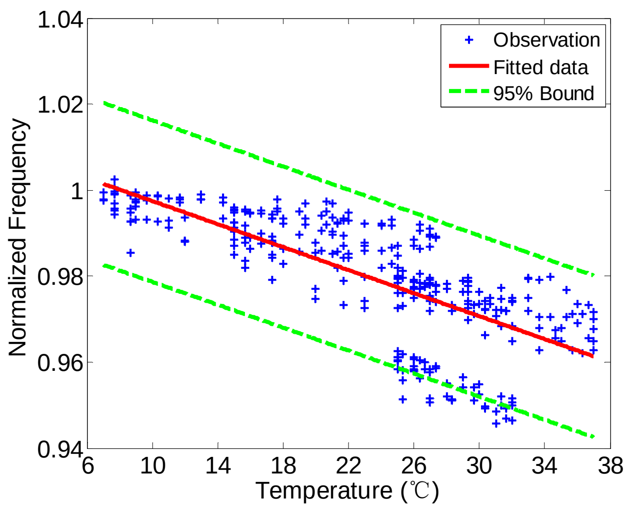

Figure 6-16. Relation of natural frequencies to temperature of Canton Tower

6.3.4 Variations in Damping with Respect to Temperature

Variations in the four damping ratios of the Canton Tower on 1 January 2014, 24 March 2014, 23 July 2014 and 12 October 2014 are shown in Figures 6-17 to 6-20. No clear correlation between damping ratios and temperature can be found, indicating that temperature has little effect on damping ratios. Nevertheless, variations in damping ratios are quite significant because damping ratios are difficult to measure accurately in practice.

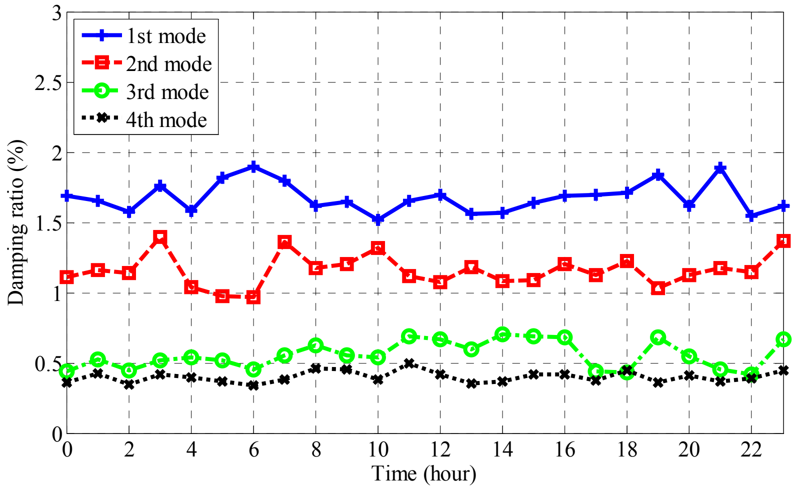

Figure 6-17. Variations in damping ratios of Canton Tower on 1 January 2014

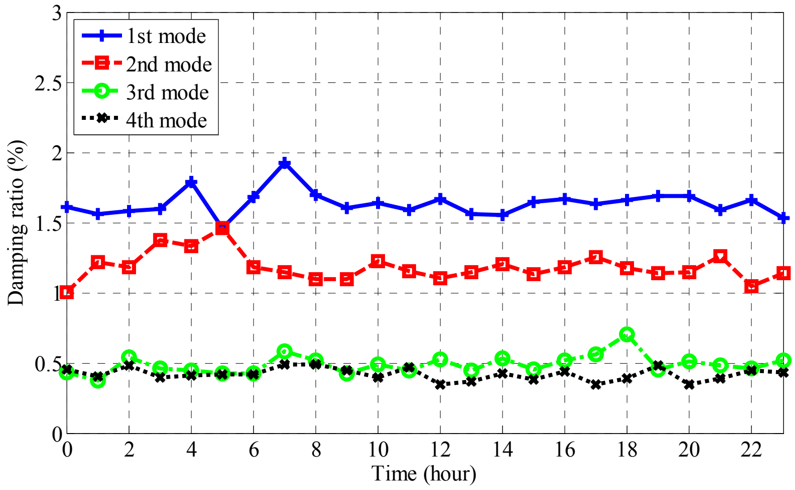

Figure 6-18. Variations in damping ratios of Canton Tower on 24 March 2014

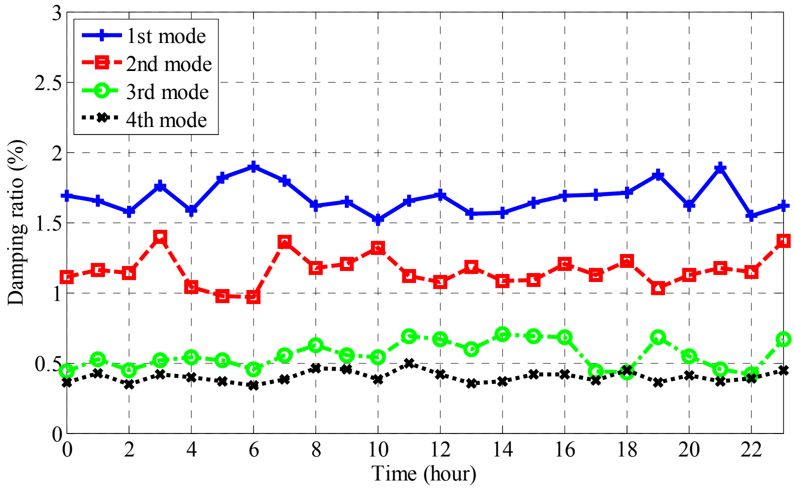

Figure 6-19. Variations in damping ratios of Canton Tower on 23 July 2014

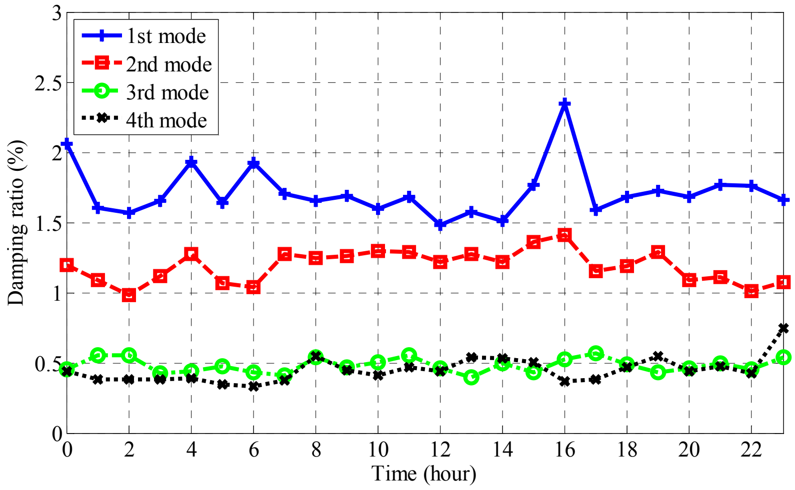

Figure 6-20. Variations in damping ratios of Canton Tower on 12 October 2014

6.4 Summary

This chapter studies the temperature effect on variations in modal properties of Canton Tower. The results show that an increase in temperature leads to a decrease in structural frequencies, whereas its effect on damping has not been well understood because of large uncertainty of damping.

Quantitative analysis results show that variations in frequencies are caused mainly by the change in the modulus of a material under different temperatures. That is, modal frequencies of the concrete structures decrease by about 0.15% when temperature increases by one degree Celsius. Frequencies of concrete structures are more sensitive to temperature change than steel structures.

CHAPTER SEVEN

CONCLUSIONS AND FUTURE WORK

7.1 Conclusions

In spite of extensive research about temperature effects on structures have been conducted over the past decades, it's still far from mature especially in super-tall structures. The long-term SHM system implemented on the 600 m tall Canton Tower provides sufficient data to investigate the temperature distribution and temperature-induced responses for the super-tall structure.

In this study, the FE models for inner tube and members of the outer tube are established to investigate the temperature distribution through the heat transfer analysis. The results demonstrate that:

1. To obtain the reasonable and accurate temperature variation results, the proper boundary condition is of great importance. The solar radiation model should be calibrated through the field test first.
2. Limited measurement points can't provide enough information of the whole structure. More information about the temperature distribution can be obtained from proper numerical analysis. Without field monitoring data, the numerical results could not be verified and are unreliable.
3. The maximum equivalent temperature variation of the hollow ring steel tube can reach 14°C in a typical sunny day, while that maximum variation of the CFT column is approximately 4.5 °C. Using CFT column can decrease the temperature difference and thus reduce the temperature-induced deformation significantly

The temperature distribution is then used as an input into the global FE model of the

Canton Tower to calculate the temperature-induced deformation. The calculated results are compared with the GPS-measured counterpart. The two results are very close, indicating that the proposed method is effective. It could be also noticed that a small temperature difference (approximated 3 to 4°C) between different facades of the outer tube can induce the relative large deformation (larger than 10 cm) for this slender super-tall structure.

A new method for calculating structural deformation using distributed strain data obtained from an SHM system is proposed. The derivation is based on the assumption that the inner tube is a bending type structure and that shear deformation can be ignored in the sections. The derived displacement and tilt are then compared with the field monitoring data. Error analysis is conducted to investigate the accuracy of the proposed approach. The following conclusions are drawn from the study:

1. Comparison shows that the indirectly-derived horizontal displacement and tilt of the Canton Tower are in good agreement with the direct measurements using GPS and the inclinometer, indicating that the proposed method can calculate the deformation of the supertall structure.
2. On a sunny day, the movement of the tower top follows a west–north–east–south clockwise pattern. The temperature-induced maximum daily movement is approximately 16 cm, which is similar to the typhoon-induced motion (the maximum mean wind speed in the typhoon period is 20.9 m/s).
3. The deformation mode of the Canton Tower is also calculated and shows the bending deformation type. This is because the girder-frame joints are pin connected and thus, the frame effect of the entire structure is not strong as a typical frame-wall system.
4. The Error analysis shows that the derived displacement has a higher accuracy then the GPS-measured results. The derived tilt has the similar accuracy as the inclinometer-measured one.
5. Aside from buildings, the proposed technique can be applied to bridges if the strains at different sections are available.

The modal properties of Canton Tower were extracted by using the EFFD algorithm. The results demonstrate that an increase in temperature leads to a decrease in structural frequencies. Quantitative analysis results show that variations in frequencies are caused mainly by the change in the modulus of a material under different temperatures. That is, modal frequencies of the concrete structures decrease by about 0.15% when temperature increases by one degree Celsius, which are more sensitive to temperature change than steel structures. This level of change in natural frequencies can't be neglected in vibration-based structural condition assessment and health monitoring. No clear correlation between temperature and damping ratios of Canton Tower can be found due to the large uncertainty of damping ratio.

7.2 Recommendations for Future Work

Although progress has been made in this thesis for the temperature effect on static and dynamic properties of the super-tall Canton Tower, several following important issues deserve further studies.

1. For large-scale structures long-span bridges and super-tall structures, it is not feasible to install large number of sensors due to the cost limitation. Sensor location optimization is a further consideration in designing the SHM system. How to efficiently and economically deploy the sensor system to obtain more useful information to investigate the temperature effect on the structures can be further investigated.
2. The temperature distribution pattern obtained in this thesis only represents some typical sunny days. The adverse temperature distribution in long-time period needs further investigation. Meanwhile, the temperature characteristics obtained in this thesis may not represent other type of structures like steel structures which have larger temperature

variations. More reliable temperature models for super-tall structures needs more monitoring exercises implemented on these type structures.

3. The variations of modal properties of super-tall structures in different environmental excitations like typhoon and earthquake need be investigated, especially the typhoon period. The air temperature normally has a rapid drop in typhoon-period. How to appropriately separate the temperature and typhoon effect on the structural modal properties is meaningful for vibration-based structural condition assessment.

REFERENCES

AASHTO, (1989), *AASHTO guide specifications, thermal effects in concrete bridge superstructures*, Washington, D.C.

Adams, R. D., Cawley, P., Pye, C. J., and Stone, B. J., (1978), "A vibration technique for non-destructively assessing the integrity of structures", *Journal of Mechanical Engineering Science*, **20**(2), 93–100.

Adjalia, M. H., Daviesb. M., Reesc. S. W., and Littler, J., (2000), "Temperatures in and under a slab-on-ground floor: two- and three-dimensional numerical simulations and comparison with experimental data", *Building and Environment*, **35**(8), 655-662.

ANSYS 14.0, (2011), [Computer software]. ANSYS Inc., Southpointe, PA, USA.

Askegaard, V., and Mossing, P., (1988), "Long term observations of RC-Bridge using changes in natural frequency", *Nordic Concrete Research*, 7, 20-27.

Au, F. T.K., Tham, L. G., Tong, M., and Lee, P. K.K., (2001), "Temperature monitoring of steel bridges", *Proceedings of SPIE*, 4337, 282-291.

Balmes, E., Basseville, M., Bourquin, F., Mevel, L., Nasser, H., and Fabien Treyssede, F., (2008), "Merging sensor data from multiple temperature scenarios for vibration monitoring of civil structures", *Structural Health Monitoring*, **7**(2), 129-142.

Blevins, R. D., (1979), *Formulas for natural frequency and mode shape*. New York: Van Nostrand Reinhold.

Branco, F. A., (1986), "Thermal effects on composite box girder bridges during construction", *Proc., 2nd Int. Conf. on Short and Medium Span Bridges*.

Canadian Society for Civil Engineering, Montreal, Canada, 215-226.

Branco, F. A., and Mendes, P. A., (1993), "Thermal actions for concrete bridges design", *Journal of Structural Engineering*, *ASCE*, **119**(8), 2313-2331.

Breccolotti, M., Franceschini, G., and Materazzi, A. L., (2004), "Sensitivity of dynamic methods for damage detection in structural concrete bridges", *Shock and Vibration*, **11**(3-4), 383–394.

Breuer, P., Chmielewski, T., Gorski, P., Konopka, E., and Tarczynski, L., (2008), "The Stuttgart TV Tower - displacement of the top caused by the effects of sun and wind", *Engineering Structure*, **30**(10), 2771-2781.

Brincker, R., Zhang, L., and Andersen, P., (2000), "Modal identification from ambient responses using frequency domain decomposition", *In: Proceedings of the 18th international modal analysis conference*, 625 – 630.

Bortoluzzi, D., Casciati, S., and Faravelli, L., (2013), "Modeling the dependency of displacement variability on thermal effects", *Journal of Vibration and Control*, **19**(15), 2301–2313.

Brockenbrough, R. L., and Merritt, F. S., (1999), *Structural steel designer's handbook*, 3rd ed., New York, McGraw-Hill.

Capps, M. W. R., (1968), "The thermal behavior of the Beachley Viaduct/Wye Bridge", *TRRL Report LR 234*, Ministry of Transport, Road Research Laboratory.

Cazzaniga, N. E., Pinto, L., Forlani, G., and Abruzzi P., (2005), "Monitoring oscillations of slender structures with GPS and accelerometers", *In: Proc of the FIG Working Week 2005 and GSDI-8*, Cairo, Egypt, 16–21.

CEB-FIP, (1993), *Model code 1990*, London, Thomas Telford.

Chan, W.S., Xu, Y.L., Ding, X.L, and Dai, W.J., (2006), "An integrated GPS–accelerometer data processing technique for structural deformation monitoring", *Journal of Geodesy*, **80**, 705–719.

Cornwell, .P.J, Farrar, C. R., Doeblig, S.W., and Sohn, H., (1999), "Environmental variability of modal properties", *Experimental Techniques*, **23**(6), 45-48.

DeWolf, J. T., Conn, P. E., and O'Leary, P. N., (1995), "Continuous monitoring of bridge structures", *Proceedings of the International Association for Bridge and Structural Engineering Symposium on Extending the Lifespan of Structures*. San Francisco, USA, 934-940.

Desjardins, S. L., Londono, N. A., Lau, D. T., and Khoo, H., (2006), "Real-time data processing, analysis and visualization for structural monitoring of the confederation bridge", *Advances in Structural Engineering*, **9**(1), 141-157.

Dilger, W. H., and Ghali, A., (1982), "Temperature stresses in composite box girder bridges", *Journal of Structural Engineering*, *ASCE*, **109**(6), 1460-1478.

Dilger, W. H., (2000), "Temperature effects in concrete and composite bridges", *Proceedings of the Workshop on Research and Monitoring of Long Span Bridges*, Hong Kong, April 2000, 1-13.

De Sortis, A., and Paoliani, P., (2007), "Statistical analysis and structural identification in concrete dam monitoring", *Engineering Structures*, **29**(1), 110-120.

Elbadry, M. M., and Ghali, A., (1983), "Temperature variations in concrete bridges", *Journal of Structural Engineering*, *ASCE*, **109**(10), 2355-2374.

Froli, M., Hariga, N., Nati, G., and Orlandini, M., (1996), "Longitudinal thermal behavior of a concrete box girder bridge", *Structural Engineering International*, **6**(4), 237-242.

Fu, H.C., Ng, S.F., Cheung, M.S., (1990), "Thermal behavior of composite bridges", *Journal of Structural Engineering*, ASCE, **116**(12), 3302–3323.

Fu, Y., and DeWolf, J. T., (2001), "Monitoring and analysis of a bridge with partially restrained bearings", *Journal of Bridge Engineering*, ASCE, **6**(1), 23–29.

Fu, Y., and DeWolf. J. T., (2004), "Effect of differential temperature on a curved post-tensioned concrete bridge", *Advances in Structural Engineering*, **7**(5), 385–397.

Giraldo, D. F., Dyke, S. J., and Caicedo, J. M., (2006), "Damage detection accommodating varying environmental conditions", *Structure health monitoring*, **5**(2), 155-172

He, X.F., Sang, W., Chen, Y.Q., and Ding, X.L., (2005), "Steep slope monitoring: GPS multiple antenna system at Xiaowan Dam", *GPS World,* **16**(11), 20–25.

Imbsen, R. A., and Vandershaf, D. E., (1984), "Thermal effects in concrete bridge superstructures", *Transportation Research Record*, **2**, 101-113.

Kehlbeck, F., (1975), *Einfluss der Sonnenstrahlung bei Brilckenbauwerken*, Werner-Verlag, Diisseldorf, Germany.

Kennedy, J.B., and Soliman, M.H., (1987), "Temperature distribution in composite bridges", *Journal of Structural Engineering*, ASCE, **113**(2), 475–482.

Kess, H.R., and Adams, D.E., (2007), "Investigation of operational and environmental variability effects on damage detection algorithms in a woven composite plate", *Mechanical Systems and Signal Processing*, **21**(6), 2394-2405.

Kijewski-Correa, T., and Kochly, M., (2007), "Monitoring the wind-induced response of tall buildings: GPS performance and the issue of multipath effects", *Journal of* Wind *Engineering and Industrial Aerodynamics*, **95**(9–11), 1176–1198.

Kullaa, J., (2011), "Distinguishing between sensor fault, structural damage, and environmental or operational effects in structural health monitoring", *Mechanical Systems and Signal Processing*, **25**(8), 2976–2989.

Li, X.J., Ge, L.L., Ambikairajah, E., Rizos, C., Tamura, Y. and Yoshida, A., (2006) "Full-scale structural monitoring using an integrated GPS and accelerometer system", *GPS Solutions*, **10**(4), 233–247.

Liu, C.Y., and DeWolf, J. T., (2007), "Effect of temperature on modal variability of a curved concrete bridge under ambient loads", *Journal of Structural Engineering*, *ASCE*, **133**(12), 1742-1751.

Malcolm, J. S., (1984), "Thermal loading of concrete roofs", *Journal of Structural Engineering*, *ASCE*, **110**(8), 1847-1860.

Mirambell, E., Aguago, A., Mendes, P. A., and Branco, F. A., (1991), "Design temperature differences for concrete bridges", *Structural Engineering International*, **1**(3), 36-40.

Nayeri, R. D., Masri, S. F., Ghanem, R. G., and Nigbor, R. L., (2008), "A novel approach for the structural identification and monitoring of a full-scale 17-story building based on ambient vibration measurements", *Smart Materials and Structures*, **17**(2), 1-19.

Ni, Y.Q., Hua, X.G., Fan, K.Q., and Ko, J.M., (2005), "Correlating modal properties with temperature using long-term monitoring data and support vector machine technique", *Engineering Structure*, **27**(12), 1762-1773.

Park, H.S., Sohn, H.G., Kim, I.S., and Park, J.H., (2008), "Application of GPS to monitoring of wind-induced responses of high-rise buildings", *Structural Design of Tall and Special Buildings,* **17**(1), 117–132.

Peeters, B., and Roeck, G. D., (2001), "One year monitoring of the Z24-Bridge: environmental effects versus damage events", *Earthquake Engineering and Structural Dynamics*, **30**(2), 149–171.

Pirner, M., and Fischer, O., (1999), "Long-time observation of wind and temperature effects on TV towers", *Journal of Wind Engineering and Industrial Aerodynamics*, **79**(1-2), 1-9.

Potgieter, I. C., and Gamble, W. L., (1983), "Response of highway bridges to nonlinear temperature distributions", *Report. No. FHWA/IL/ UI-201*, University of Illinois at Urbana-Champaign, Urbana-Champaign, USA.

Psimoulis, P. A., and Stiros, S. C., (2008), "Experimental assessment of the accuracy of GPS and RTS for the determination of the parameters of oscillation of major structures", *Computer-Aided Civil and Infrastructure Engineering,* **23**(5), 389–403.

Rao, S. S., (2005), *The Finite Element Method in Engineering*, Woburn, Mass, Butterworth Heinemann.

Roberts-Wollman, C. L., Breen, J. E., and Cawrse, L., (2002), "Measurements of thermal gradients and their effects on segmental concrete bridge", *Journal of bridge engineering*, *ASCE*, **7**(3), 166-174.

Roberts, G.W., Meng, X.L., and Dodson, A. H., (2004), "Integrating a global positioning system and accelerometers to monitor the deflection of bridges", *Journal of Surveying Engineering*, *ASCE*, **130**(2), 65–72.

Salawu, O. S., (1997), "Detection of structural damage through changes in frequency: A review", *Engineering Structures*, **19**(9), 718-723.

Saleh, B., and Blum, P. A., (1990), "Study of temperature effect on behavior of structures", *Journal of Surveying Engineering*, **116**(1), 1-12.

Scetta, A., Scotta, R., and Vitaliani, R., (1995), "Stress analysis of concrete structures subjected to variable thermal loads", *Journal of Structural Engineering, ASCE*, **121**(3), 446-457.

Shahawy, M. A., and Arockiasamy, M., (1996), "Analytical and measured strains in Sunshine Skyway Bridge. II", *Journal of Bridge Engineering, ASCE*, **1**(2), 87-97.

Smyth, A., and Wu, M.L., (2007), "Multi-rate Kalman filtering for the data fusion of displacement and acceleration response measurements in dynamic system monitoring", *Mechanical Systems and Signal Processing,* **21**(2), 706–723.

Sohn, H., Worden, K., and Farrar, C. R., (2002), "Statistical damage classification under changing environmental and operational conditions", *Journal of intelligent material systems and structures*, **13**(9), 561-574.

Sohn, H., Dzwonczyk, M., Straser, E. G. Kiremidjian, A. S., Law, K.H., and Meng, T., (1999), "An experimental study of temperature effect on modal parameters of the Alamosa Canyon Bridge", *Earthquake Engineering Structural Dynamics*, **28**(8), 879-897.

Song, W., and Dyke, S. J., (2006), "Ambient vibration based modal identification of the Emerson bridge considering temperature effects", *4th World Conference on Structural Control and Monitoring*, July 11-13, San Diego, USA.

Tamura, Y., Matsui, M., Pagnini, L. C., Ishibashi, R., and Yoshida, A., (2002), "Measurement of wind-induced response of buildings using RTK-GPS", *Journal of Wind Engineering and Industrial Aerodynamics,* **90**(12–15), 1783–1793.

Tong, M., Tham, L. G., Au, F. T. K., and Lee, P. K. K., (2001), "Numerical modelling for temperature distribution in steel bridges", *Computers and Structures*, **79**(6), 583-593.

Wang, M. L., (2008), "Load and environmental effects of a damaged PC box girder bridge", *The 4th International Workshop on Advanced Smart Materials and Smart Structures Technologies*, Tokyo.

Wong, K.Y., Man, D.K.L., and Chan, K.W.Y., (2002), "Thermal load and response monitoring of Ting Kau (cable-stayed) Bridge", *International Conference on Innovation and Sustainable Development of Civil Engineering in the 21st Century*, Beijing, China, 249-252.

Xia, Y., Hao, H., Zanardo, G., and Deeks, A. J., (2006a), "Long term vibration monitoring of a RC slab: temperature and humidity effect", *Engineering Structures*, **28**(3), 441-452.

Xia, Y., Hao, H., and Deeks, A.J., (2006b), "Variation of vibration properties induced by changing environment", *The Ninth International Symposium on Structural Engineering for Young Experts*, Fuzhou, China, 2229-2235.

Xia, Y., Chen, B., Zhou, X.Q. and Xu, Y.L., (2013), "Field monitoring and numerical analysis of Tsing Ma Suspension Bridge temperature behavior", *Structural Control and Health Monitoring*, **20**(4), 560-575.

Xu, Y.L., Chen, B., Ng, C.L., Wong, K.Y. and Chan, W.Y., (2010), "Monitoring temperature effect on a long suspension bridge", *Structural Control and Health Monitoring*, **17**(6), 632-653.

Xu, Z.D., and Wu, Z.S., (2007) "Simulation of the effect of temperature variation on damage detection in a long-span cable-stayed bridge", *Structure health monitoring*, **6**(3), 177-189.

Yan, A.-M., Kerschen, G., De Boe, P., and Golinval, J.-C., (2003), "Structural damage diagnosis under varying environmental conditions—Part I: a linear analysis", *Mechanical Systems and Signal Processing*, **19**(4), 847-864

Yigit, C.O., Li, X.J., Inal, C., Ge, L., and Yetkin M., (2010), "Preliminary evaluation of precise inclination sensor and GPS for monitoring full-scale dynamic response of a tall reinforced concrete building", *Journal of Applied Geodesy,* **4**(2), 103–113.

Yi, T.H., Li, H.N., and Gu, M., (2013), "Recent research and applications of GPS-based monitoring technology for high-rise structures", *Structural Control and Health Monitoring*, **20**(5), 649-670.

Zuk, W., (1965), "Thermal behavior of composite bridges - insulated and uninsulated", *Highway Research Record*, 76, 231-253.